

Optoelectronic Devices for Optical Memory Systems

Thesis by

Xu Wang

In Partial Fulfillment of the Requirements
for the Degree of
Doctor of Philosophy

California Institute of Technology
Pasadena, California

1999

(Submitted November 25, 1999)

© 1999

Xu Wang

All Rights Reserved

Acknowledgements

I am very grateful to my advisor, Professor Demetri Psaltis, for all the support and advice over the years. His encouragement, kindness and sense of humor made my stay at his group to be a wonderful experience. Clearly, I have never had such a great mentor who deserves more respect.

I am greatly indebted to Dr. Tim Strand, Jeff Mason, and Milt Latta in IBM Almaden Research Center for many valuable discussions and their measuring of optical diffraction from sub-wavelength features to make this collaboration quite enjoyable and fruitful. I am also greatly indebted to Dr. Daniel Wilson, Dr. Paul Maker and Dr. Richard Muller in the Microdevices Section at the Jet Propulsion Laboratory for preparing several PMMA blazed grating samples with direct-electron beam lithography in the Liquid Crystal blazed grating beam deflector project.

During my years in Professor Psaltis's research group, I was very lucky to get extensive orientations from senior group members, especially Dr. Jean-Jacques Drolet and Dr. David Marx. The former introduced me into the wonderful world of liquid crystal display. The latter helped me a great deal in modeling the sub-wavelength structure's diffraction. I also have enjoyed all kinds of help and advice from all other members. They are: Dr. Jiafu Luo, Robert Denkwalter, Dr. Geoffrey Burr, Dr. Chuan Xie, Dr. Allen Pu, Dr. Ernest Chuang, Dr. Michael Levene, Dr. Xin An, Dr. George Barbasthathis, Dr. Ali Adibi, Greg Billock, Greg Steckman, George Ouyang, Wenhai Liu, Chris Moser, Zhiwen Liu, Yungping Yan, George Panotopoulos, Jose Mumbru, and Irena Maravic. Of course, no research can be conducted smoothly without the help and assistance from Yayun Liu, Lucinda Acosta, Joseph Chiu, Dimitris Sakellariou, and Helen Carrier.

Finally, thank you to my lovely wife, Ping Nan, for taking care of me and bringing me all the smiles, encouragement, and more importantly, the love. I can not make it without her.

Support of the research presented in this thesis was provided in part by the National Science Foundation's Center for Neuromorphic Systems Engineering at California Institute of Technology.

Abstract

This thesis describes several optoelectronic devices developed for the optical memory system. It consists of three parts, which are liquid crystal beam steering devices, modeling and measurement of optical diffraction from subwavelength structure at focused spot, and CMOS detector design.

In liquid crystal beam steering devices, two types of liquid crystal beam deflectors have been successfully demonstrated. The essential working idea of those two deflectors is the same, which is utilizing a blazed grating (either permanently fabricated or virtually built up) to deflect the incident beam and the liquid crystal is used as an electrically controllable birefringent medium. The reflective type deflector exploits the liquid crystal on silicon (LCOS) technology to build up a virtual blazed grating (dynamic grating) and vary this virtual grating's period to achieve multiple steering angels. Seven addressable angles with as high as 93% steering efficiency have been demonstrated. A numerical modeling tool is also developed to analyze liquid crystal molecule director's distribution under nonuniform electrical field (fringe-field-effect). The transmission type deflector is based on a custom-fabricated PMMA blazed grating (fixed grating) and dynamically address multiple angles by stacking several layers of PMMA/LC composite gratings. 16 steering angles are obtained with the contrast ratio of 18. A fabrication-compensation trick is proposed to greatly improve the device's performance.

In modeling and measurement of optical diffraction from subwavelength structure at focused spot, we describe a technique for studying scattering from subwavelength features that used a focused ion beam system to generate subwavelength, submicron features and a simple scatterometer to measure the scattering from single subwavelength scatterers. A two-dimensional model that handles arbitrary profiles is described. The model is shown to agree quite well with the experimental measurements. The model is then used to demonstrate ways in which the aspect ratios of

subwavelength ridges and trenches can be obtained from scattering data and how ridges can be distinguished from trenches over a wide range of aspect ratios. We show that some earlier results on distinguishing pits from particles do not extend to low aspect ratio features.

Finally, in CMOS detector, we have designed a CMOS detector to be used in the compact memory module. The chip features 64x64 array of $17\mu\text{m} \times 17\mu\text{m}$ pixel with 23% filling factor within a $2\text{mm} \times 2\text{mm}$ die, correlated double sampling (CDS) signal-conditioning circuit in each column, as well as the software-controlled window-of-interest readout. Even more, two pixel designs (active photodiode and direct readout photodiode) are incorporated with the same chip for performance comparison.

Contents

Acknowledgements	iii
Abstract	v
1 Introduction	9
1.1 Motivation of the thesis work	9
1.2 Summary of the thesis work	12
2 Liquid crystal electro-optics analysis	14
2.1 Liquid crystal introduction	14
2.2 Electro-optic effect of liquid crystal	15
2.2.1 Numerical modeling	15
2.2.2 Liquid crystal configurations	18
2.3 Liquid crystal cell packaging process	23
2.3.1 Liquid crystal alignment process	23
2.3.2 Package process monitoring technique	27
3 Liquid crystal on silicon (LCOS) beam steering device	31
3.1 Introduction	32
3.2 Design considerations	35
3.2.1 Liquid crystal analysis	35
3.2.2 Diffraction analysis	36
3.3 Fabrication	40
3.4 Characterization	41
3.4.1 Experiment setup	41
3.4.2 Optimal voltage vs linear voltage	44
3.4.3 Multiple steering angles	45

3.5	Discussions	46
3.5.1	Fringe field effect	46
3.5.2	Hologram recording with the LCOS deflector	56
3.5.3	Programmable deflector design	58
4	Liquid crystal blazed grating beam steering device	62
4.1	Introduction	62
4.2	Design considerations	65
4.2.1	Diffraction analysis	65
4.2.2	Driving voltage loss and non-uniformity	69
4.3	Fabrication process	73
4.4	Experiment and discussion	77
4.4.1	Define sample profile parameters	77
4.4.2	Single layer deflector characterization	78
4.4.3	Multiple layer deflector characterization	81
5	Modeling and measuring of optical diffraction from sub-wavelength structures	85
5.1	Introduction	86
5.2	Diffraction modeling	88
5.2.1	Incident beam	88
5.2.2	Sample profile input	91
5.2.3	Convergence issue	92
5.2.4	Incident angle	92
5.3	Experimental measuring	93
5.3.1	Sample fabrication and characterization	93
5.3.2	Scatterometer system	95
5.3.3	Scattering measurements	99
5.4	Comparing measurement and modeling results	100
5.4.1	AFM curve remeasurement story	100
5.4.2	Intensity comparison	104

5.5	Further discussion	110
5.5.1	Aspect ratio extraction	110
5.5.2	Distinguishing trenches and ridges	114
5.6	Application in optical memory system	121
5.6.1	Single pit memory	123
5.6.2	Multi-pits memory	123
6	Design of a CMOS detector	130
6.1	Motivation	130
6.2	Design details	134
6.2.1	Basics	134
6.2.2	Sensing elements	135
6.2.3	Readout circuits	139
6.3	Noise analysis	141
6.3.1	Reset noise	143
6.3.2	Integration noise	145
6.3.3	Readout noise	145
7	Conclusion	147
7.1	Beam deflectors	147
7.2	Diffraction of subwavelength structure	148
7.3	CMOS detector	149
	Bibliography	150

List of Figures

1.1	Compact memory module concept.	10
1.2	3-D holographic recording system concept.	11
2.1	Liquid crystal cell modeling coordinate system.	16
2.2	Commonly used liquid crystal alignment configurations.	18
2.3	Homogeneous alignment configurations.	19
2.4	Homogeneous alignment orientation angle distribution modeling result.	20
2.5	Homogeneous alignment refractive index modeling result.	21
2.6	Hybrid Alignment Nematic (HAN) configuration.	22
2.7	Numerical results of HAN orientation angle distribution at different driving voltages.	22
2.8	HAN refractive index modeling result.	24
2.9	Liquid crystal cell package process flow chart.	26
2.10	Liquid crystal cell package testing experimental setup.	28
2.11	Output intensity is a function of phase delay difference between ordinary and extra-ordinary light with crossed polarizer setup.	29
2.12	Liquid crystal cell thickness check.	29
3.1	Liquid crystal on Silicon (LCOS) beam deflector.	33
3.2	LCOS multiple angle addressing approach.	34
3.3	LCOS deflector diffraction modeling.	37
3.4	Diffraction efficiency simulation comparison between optimal voltage assignment and linear voltage assignment along the electrodes.	39
3.5	Custom developed LCOS deflector packaging process.	40
3.6	Characterization setup of LCOS deflector.	42
3.7	Picture of LCOS deflector and liquid crystal driver board.	43

3.8	Experimental data comparison between optimal voltage assignment and linear voltage assignment along the electrodes.	44
3.9	Measurement data of those 7 steering angles.	45
3.10	Picture of 7 steering angle beam spots.	47
3.11	LCOS deflector response time measurement.	48
3.12	Flyback issue.	49
3.13	Fringe field introduction.	50
3.14	Simulation of fringe field effect.	51
3.15	Relationship of electric displacement D and electric field E for liquid crystal medium.	52
3.16	Fringe field effect modeling result of refractive index at different voltage with depth/width ratio of 1.	54
3.17	Fringe field effect modeling result of refractive index at different voltage with depth/width ratio of 10.	55
3.18	Fringe field effect modeling result of refractive index at different depth/width ratios with 1.2V driving voltage.	56
3.19	Experimental setup for multiple holograms recording with LCOS deflector.	57
3.20	Multiple holograms recording and readout with LCOS deflector.	58
3.21	Programmable LCOS beam deflector addressing circuitry.	60
3.22	Programmable LCOS beam deflector chip layout.	61
4.1	Liquid crystal blazed grating beam deflector.	63
4.2	Multiple layer stacking concept to achieve multiple deflection angles.	64
4.3	Liquid crystal blazed grating diffraction model.	65
4.4	Optimization of the blazed grating depth.	67
4.5	Influence of blazed grating duty cycle on diffraction efficiency.	68
4.6	Simulation result from DIFFRACT program.	69
4.7	Illustration of liquid crystal blazed grating deflector's driving voltage loss and non-uniformity.	70

4.8	Liquid crystal blazed grating deflector's index matching.	72
4.9	PMMA blazed grating fabrication process flow chart.	74
4.10	Surface profile of 10 μ m period grating measured by AFM.	75
4.11	Liquid crystal blazed grating deflector packaging process.	76
4.12	Device's characterization experimental setup.	77
4.13	Determination of grating surface profile parameters.	79
4.14	Liquid crystal blazed grating diffraction intensity vs driving voltage. .	80
4.15	Performance of the 4 LC/PMMA blazed gratings.	81
4.16	Comparison between real-OFF state and virtual-OFF state.	82
4.17	Measurement data of the 4 stacked-grating 16-angle deflector.	83
4.18	Photographs of the 16-angle deflector diffracted spots.	84
5.1	Diffraction modeling of focused spot from sub-wavelength structure. .	86
5.2	Incident field notation.	88
5.3	Far field diffraction comparison with rectangular incident beam and Gaussian incident beam.	90
5.4	Comparison between AFM curve and sampling curve. Illustrated with profile2 contour.	91
5.5	Sample surface contours measured by AFM.	94
5.6	Experimental setup of measuring the scattering from sub-wavelength structures.	96
5.7	Experimental setup's coordinate system.	97
5.8	Experimental verification of the numerical aperture of focusing lens. .	101
5.9	Optimal profile searching data plots.	103
5.10	Scattering region data comparison between experiment and numerical modeling for all narrow profiles (1 & 3).	106
5.11	Scattering region data comparison between experiment and numerical modeling for all wide profiles (2 & 4).	107
5.12	Specular region data comparison between experiment and numerical modeling for narrow profiles (1 & 3).	108

5.13 Specular region data comparison between experiment and numerical modeling for wide profiles (2 & 4).	109
5.14 Constant-volume profiles contours.	111
5.15 Constant-volume trenches aspect ratio extraction calculation results.	112
5.16 Zoom in plot of the specular region data at TM mode for all four trenches under normal incident.	113
5.17 Constant-volume ridges aspect ratio extraction calculation results.	115
5.18 Zoom in plot of the specular region data at TM mode for all four ridges under normal incident.	116
5.19 TE/TM intensity ratio vs aspect ratio at different scattering angles.	118
5.20 Far field scattering calculation of trenches illuminated with 60° to the surface normal.	119
5.21 Far field scattering calculation of ridges illuminated with 60° to the surface normal.	120
5.22 Some parameters comparison between current CD and DVD format.	122
5.23 Numerical modeling of single pit. (a) single bump. (b) single trench. The parameters are adopted from DVD disc format.	124
5.24 Numerical modeling of single pit. (a) contour profiles with different heights. (b) far field intensity at center point corresponding to different heights.	125
5.25 Numerical modeling of single trench. (a) contour profiles with different depths. (b) far field intensity at center point corresponding to different depths.	126
5.26 Diffraction intensity at center location from 2 pits (bumps) with different depth combinations.	128
6.1 Compact system with separate detector and SLM.	131
6.2 Performance comparison between CMOS and CCD detector/imager.	132

6.3	CMOS imager major developers and their products. PD stands for PhotoDiode, ADC is Analog to Digital Conversion, DR-PD is Direct Readout PhotoDiode, and APS is active pixel sensor.	133
6.4	Passive photodiode pixel circuits.	135
6.5	Direct readout photodiode pixel circuits.	136
6.6	Active photodiode pixel circuits.	137
6.7	Active photogate pixel circuits.	138
6.8	Active pixel Sensor (APS) pixel circuits.	140
6.9	CMOS imager chip layout.	141
6.10	Reset circuit small signal model.	144

Chapter 1 Introduction

With the fast evolution of 20th century science and technology, the classical 19th century science, Optics, also experiences several revolutionary breakthroughs to make it still outperform its closest competitor, Electronics, in many fields. With the invention of the laser in the early 1960s, classical optics stepped into the modern optics arena. Currently, people's everyday life is benefiting greatly from two technologies that stem from optics, which are CD/DVD technology and fiber communication technology. Even more, there are no signs that optical technology will slow down its evolution in the near future. No wonder that Gerald J. Butters, Optical Networking Group President from Lucent Technology, Inc., said: "Optical technology will be as important to the 21st century as electronics was to the 20th century." (<http://www.lucent-optical.com>)

1.1 Motivation of the thesis work

Compact, highly integrated system for holographic memories is quite desirable in many applications. Figure 1.1 shows such a compact architecture, employing angular multiplexing. The module is comprised of a photorefractive crystal, such as lithium niobate, in which holograms are stored, a pair of liquid crystal beam steerers that are responsible for angularly multiplexing holograms in the crystal, and an optoelectronic integrated circuit (OEIC) that merged the functions of a reflective SLM (for recording holograms) and a detector array (for readout). For this module, holograms are written by letting the signal beam, modulated by the OEIC, interfere with the reference beam coming from the back of the crystal. Holograms are readout by illuminating the crystal from the front with a counter-propagating reference beam, causing the conjugate reconstruction to self-focus back on the OEIC, where it is sensed and processed.

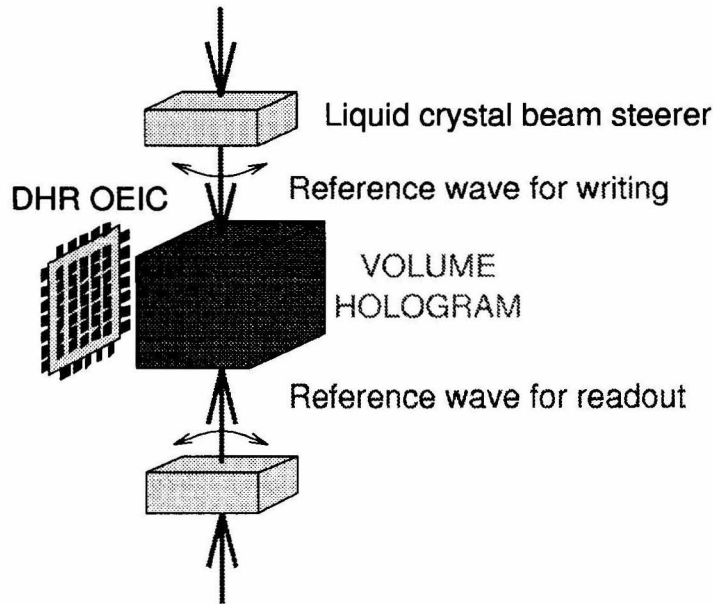


Figure 1.1: Compact memory module concept.

To appreciate the advantage of this compact module, we might want to see the conventional angularly multiplexed system which is illustrated in Figure 1.2. For conventional system, holograms are stored in the recording medium by the interference of a signal beam coming from the upper left corner with a reference beam from the upper right corner. A transmissive SLM imprints data on the signal beam, while a motorized rotating mirror addresses individual data pages within the memory. During the readout, the reconstructed signal beam propagates away from the SLM, towards a detector array located in the lower right corner of the figure. As we can see, first, this system needs lens to image the reconstructed data page on the detector array so that lenses aberrations are a big problem when large pages of data are stored. Also, the required distance between the lenses, the SLM, and the detector array imposes a minimum size on the system. Second, the motorized mirror is usually big and heavy, and suffers from a low speed and backlash (repeatability) problems. Finally, the detector array must be aligned to within a fraction of the pixel size with the SLM, which is pretty challenging from the experiment point of view. Compared to that,

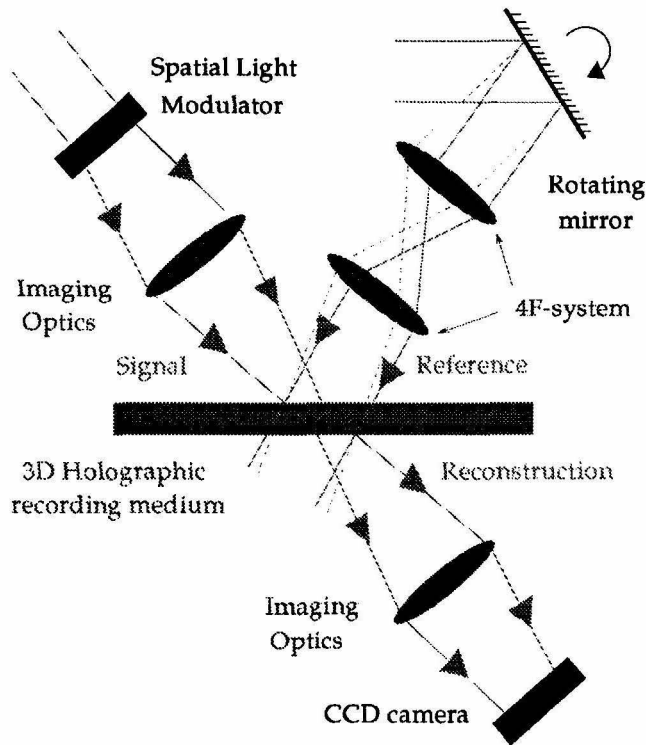


Figure 1.2: 3-D holographic recording system concept.

the compact module consists of no lenses. Conjugate readout eliminates the need for imaging optics, since the reconstruction retraces the path and phase profile of the signal beam during the recording. This allows all the components to be assembled in a single compact structure. Also, phase conjugation undoes aberrations in the signal path so that the reconstruction possesses high fidelity. Secondly, the compact module's page addressing devices, two liquid crystal beam steerers, are free of the problems associated with conventional mechanical addressing system, such as vibration, backlash, low speed, high power consumption, and with acousto-optics deflectors, such as wavelength shift and high voltage operation. Finally, if a single OEIC containing modulators and detectors at each pixel location is employed, alignment is guaranteed by design.

The motivation of this thesis work is to develop two key components, the liquid crystal beam steerer and the OEIC, for this compact memory module. (With the

evolution of this compact module, a CMOS imager rather than an OEIC is finally needed.)

1.2 Summary of the thesis work

This thesis presents several optoelectronic devices developed for an optical memory system. It is organized into 7 chapters. Chapter 2 describes the numerical modeling of liquid crystal electro-optics effect. This analysis could be generally used as a good reference for developing liquid crystal devices. Furthermore, its application in monitoring the liquid crystal device's packaging process is also successfully demonstrated.

Chapter 3 describes a low cost, low operation voltage, but high performance, reflective type beam steering device based on liquid crystal on silicon technology (LCOS) [1]. Seven dynamically addressable angles with as high as 93% steering efficiency have been successfully demonstrated. A fringe field effect analysis is done for improving the device's performance.

Chapter 4 describes a transmission type liquid crystal blazed grating beam steering device based on a stacking technique. Sixteen steering angles with contrast ratio of 18 have been obtained. A manufacturing compensation trick is proposed to improve the device's performance.

Chapter 5 presents the work on the modeling and measurement of optical diffraction from sub-wavelength structures at a focused spot. The excellent agreement between numerical modeling and experimental measurement has been demonstrated. Also, an aspect ratio extraction and trench/ridge distinguishing technique for sub-wavelength structure is proposed and justified. Finally, the modeling's application in pit-encoded optical memory is demonstrated. An interesting difference of diffraction between S and P polarizations from subwavelength structures is found. A multi-pits encoding method is proposed to boost the storage density of this pit-encoded optical memory system.

Chapter 6 described the details of a custom-designed CMOS detector. A complete noise analysis of the imager is carried out to help design the future ultra small pixel

CMOS imager.

Chapter 7 contains the conclusion remarks and presents several ideas for future work.

Chapter 2 Liquid crystal electro-optics analysis

This chapter introduces liquid crystal's electro-optics as well as its packaging process developed for usage in this thesis work. A detailed numerical modeling of the nematic liquid crystal's electro-optics effect is presented, which build up a solid ground for further liquid crystal device development. Also, this numerical modeling has been successfully used as a powerful tool for monitoring the liquid crystal packaging process.

2.1 Liquid crystal introduction

The study of liquid crystals began in 1888 when Friedrich Reinitzer observed a material known as cholesterylbenzoate has two distinct melting points. In his experiment, Reinitzer increased the temperature of a solid sample and watched the crystal change into a hazy liquid. As he increased the temperature further, the material changed again into a clear, transparent liquid [2]. Because of that, Reinitzer is often credited with discovering a new phase of matter: the liquid crystal phase.

Liquid crystal materials generally have several common characteristics, such as a rod-like molecular structure, rigidity of the long axis, and a strong dipole and/or easily polarizable substituent. The distinguishing characteristic of the liquid crystalline state is the tendency of the molecule to point along a common axis, called the director. This tendency leads to a condition known as anisotropy which makes liquid crystal materials interesting.

The liquid crystal state is a distinct phase of matter observed between the crystalline(solid) and isotropic(liquid) states. There are many mesophases of liquid crystal materials, such as nematic phases, smectic phases, cholesteric phases, etc. The most

simple/popular one is the nematic phase which is characterized by molecules that tend to point in the same direction (along the director). It is found that external perturbation (either electric or magnetic fields) can cause significant changes in the macroscopic properties of the liquid crystal system. This could be explained by the molecule dipole model. For a permanent electric dipole, one end of a molecule has a net positive charge while the other end has a net negative charge. With an electric field on, the dipole molecules tend to orient themselves along the direction of the field. If a molecule does not form a permanent dipole, the electric field produces slight re-arrangement of electrons and protons in molecules such that an induced electric dipole results. More details about the electro-optics of the liquid crystal will be discussed in the next section.

Liquid crystal technology has had a major effect not only on many areas of science and engineering, but everyday life as well. The most common application is the liquid crystal display (LCDs). This field has grown into a multi-billion dollar industry, and many significant scientific and engineering discoveries have been made. Other applications include optical information processing (used as SLM), liquid crystal thermometers, as well as non-destructive mechanical testing of materials under stress, etc.

2.2 Electro-optic effect of liquid crystal

2.2.1 Numerical modeling

For this electro-optic effect analysis, we numerically modeled the nematic liquid crystal molecule director orientation distribution at different electrical fields. The basic idea is to minimize the net free energy of the liquid crystal molecules, at which its director distribution reaches a stable state. By Frank elastic continuum theory [3],

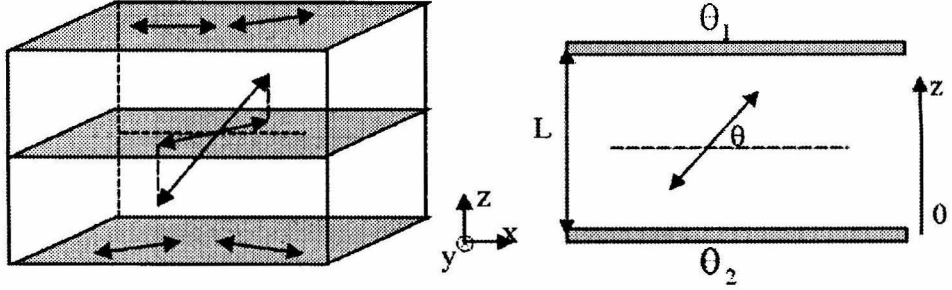


Figure 2.1: Liquid crystal cell modeling coordinate system.

the net free energy of the molecule can be represented as:

$$F_{net} = \frac{1}{2} \int_0^\infty [K_{11}(\nabla \cdot \vec{n})^2 + K_{22}(\vec{n} \cdot (\nabla \times \vec{n}))^2 + K_{33}(\vec{n} \times (\nabla \times \vec{n}))^2 - \vec{D} \cdot \vec{E}] dV \quad (2.1)$$

Where K_{11} is the splay constant, K_{22} is the twist constant, and K_{33} is the bend constant. Those constants correspond to S-deformation, T-deformation and B-deformation. \vec{D} is the electric displacement and \vec{E} is the electric field. The molecule director is $\vec{n} = (\cos \theta \cos \phi, \cos \theta \sin \phi, \sin \theta)$, as shown in Figure 2.1.

During the numerical modeling of the liquid crystal electro-optics effect, we made three assumptions: (1) Strong anchoring at both surfaces. This means the boundary condition is defined exclusively by surface orientation angle. (2) No twist orientation involved, which makes the K_{22} term in Equation 2.1 disappear. (3) 1-D modeling only. This implies $E_x = E_y = 0$. Based on those three assumptions, the simplified formula from Equation 2.1 can then be represented as:

$$F_{net} = \frac{1}{2} \int_0^L (K_{11} \cos^2 \theta + K_{33} \sin^2 \theta) \left(\frac{d\theta}{dz} \right)^2 dz - \frac{\frac{1}{2} \epsilon_0 V_{apply}^2}{\int_0^L \frac{1}{\epsilon_\perp \cos^2 \theta + \epsilon_\parallel \sin^2 \theta} dz} \quad (2.2)$$

Where ϵ_0 is the dielectric constant in free space, V_{apply} is the liquid crystal driving voltage. ϵ_\perp and ϵ_\parallel are the dielectric constants of perpendicular and parallel direction

to the electrical field respectively. By using variational calculus method [4], this integral equation can be changed into a differential equation. After a long derivation, the final differential equation is obtained as follows:

$$\left(\frac{dz}{d\theta}\right)^2 = \frac{K_{11}(1 + K \sin^2 \theta)}{C + \frac{D_z^2}{\epsilon_o \epsilon_{\perp}(1+r \sin^2 \theta)}} \quad (2.3)$$

Where $K = \frac{K_{33}-K_{11}}{K_{11}}$, D_z is the electric displacement along the Z direction, $r = \frac{\epsilon_{\parallel}-\epsilon_{\perp}}{\epsilon_{\perp}}$, and C is the constant defined by the boundary condition. Numerically solving this equation with boundary conditions θ_1 and θ_2 as shown in Figure 2.1, we can easily obtain the molecule director distribution inside the whole cell at a certain driving voltage.

We need to perform one more step to get the liquid crystal's refractive index information since that is the important information for the optical application. We know from the previous section that liquid crystal is an anisotropic birefringent material. From the well-known formula for an anisotropic medium's index ellipse, we have the distribution of refractive index for extra-ordinary light inside the liquid crystal cell

$$n_e(\theta_z) = \frac{n_o n_e}{\sqrt{n_o^2 \cos^2 \theta_z + n_e^2 \sin^2 \theta_z}} \quad (2.4)$$

Where θ_z is the orientation angle, n_e and n_o are the liquid crystal's extraordinary and ordinary refractive index, respectively. It is more convenient, from a practical point of view, to use the effective refractive index of the whole cell for further discussion. It is given by

$$n_{eff} = \frac{1}{L} \int_0^L n_e(z) dz \quad (2.5)$$

Basically the liquid crystal material can be considered as an electrically controlled birefringent medium. It is important to determine the phase delay between ordinary and extra-ordinary light after passing through the medium. We can represent it as

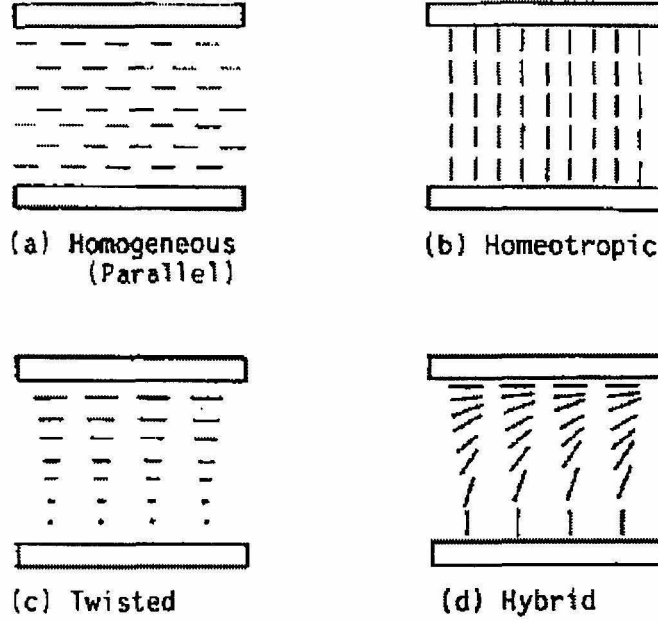


Figure 2.2: Commonly used liquid crystal alignment configurations.

follows:

$$\delta = \frac{2\pi}{\lambda} \int_0^L (n_e(z) - n_o) dz \quad (2.6)$$

2.2.2 Liquid crystal configurations

There are four common aligned nematic configurations that are shown in Figure 2.2. The boundary condition for each case is illustrated in the figure. Twist aligned nematic configuration is widely used in liquid crystal display, where the contrast ratio and viewing angle are the big concerns. Here we are discussing two configurations for our applications: homogeneous alignment nematic configuration and hybrid aligned nematic (HAN) configuration.

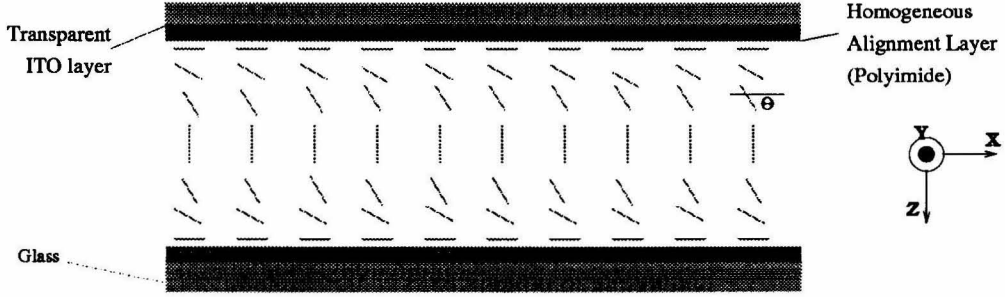


Figure 2.3: Homogeneous alignment configurations.

Homogeneous alignment nematic configuration

In this configuration, both layers induced strong parallel alignment along the surface by spin-coating an anchoring chemical agent and then rubbing the surface. The elasticity of liquid crystal, the applied electrical field, and the surface anchoring chemicals result in a symmetrical smooth rotation of the molecule director inside the nematic film. Figure 2.3 illustrates the homogeneous alignment configuration's molecule director distribution along the cell depth direction. The chosen liquid crystal material is Merck E7, whose refractive indexes for extra-ordinary and ordinary light are 1.737 and 1.5185 respectively [5]. E7 is a eutectic mixture of a number of cyanobiphenyls and cyanoterphenyls with a positive dielectric anisotropy, $\epsilon_{||} \approx 18$, $\epsilon_{\perp} \approx 6$, at 1KHz frequency and room temperature [6]. Figure 2.4 shows the calculation results for orientation angle distribution with different driving voltages. As we can see, the director orientation angle is increased with the magnitude of the driving voltage. The middle layer of the cell has the largest orientation angle for each driving voltage reaching 90° when the voltage is large. After determining the orientation angle distribution inside the cell at different voltages, the effective refractive index (for extraordinary light) with driving voltage was easily calculated. Figure 2.5 shows that, actually, the refractive index decreases continuously as the driving voltage increases. Ideally it can be swept from n_e to n_o when the driving voltage is varied from 0 to a very large value (assuming a nonlinear effect does not occur). This electrically controlled

LC cell orientation angle vs Z location

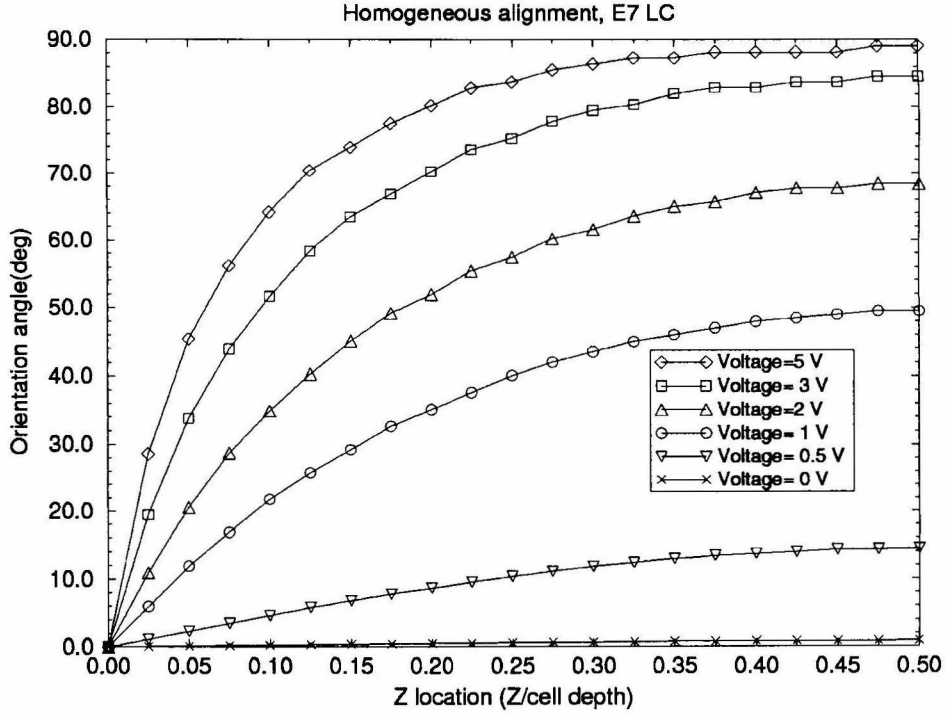


Figure 2.4: Homogeneous alignment orientation angle distribution modeling result.

birefringence (ECB) is about 0.2 for E7 within 5V, which is a big advantage, from both the refractive index modulation magnitude and the power consumption point of view, over commonly used electro-optical crystals. The property of index varying with driving voltage has been used in our liquid crystal blazed grating beam deflector (see Chapter 4). Furthermore, there is one more interesting thing in Figure 2.5. The variation of the refractive index only happens after a certain value, i.e., about 0.9V for our E7 material. This is the so-called threshold voltage for the liquid crystal material with the homogeneous alignment configuration. Further research has shown that the value of this threshold voltage is only a function of material physical parameters, such as viscosity constant, elastic constant, etc. The threshold voltage is not changed with the cell's thickness.

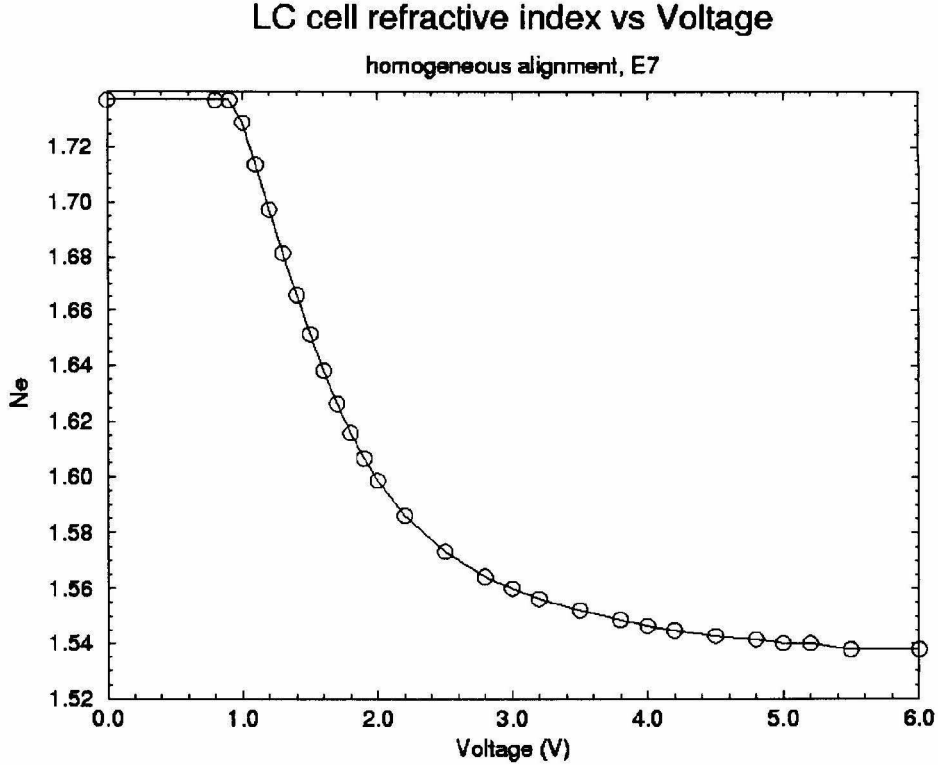


Figure 2.5: Homogeneous alignment refractive index modeling result.

Hybrid Alignment Nematic (HAN) configuration

In this configuration, one layer induced strong homogeneous alignment, where the other induced strong homeotropic alignment. The elasticity of liquid crystal as well as the anchoring chemical agent result in a smooth rotation of the molecule director's orientation to form a splay-bend conformation inside the nematic film, as illustrated in Figure 2.6. Using the same parameters described previously for homogeneous alignment, we calculated the director distribution as well as the refractive index with different driving voltage for this HAN configuration. The results are shown in Figure 2.7 and Figure 2.8. Actually, the HAN configuration could be considered as half of the homogeneous alignment, where its 90° alignment boundary condition corresponds to the middle layer of a homogeneous alignment driven with a large voltage. Like homogeneous alignment, the director also orients along the electrical field direction

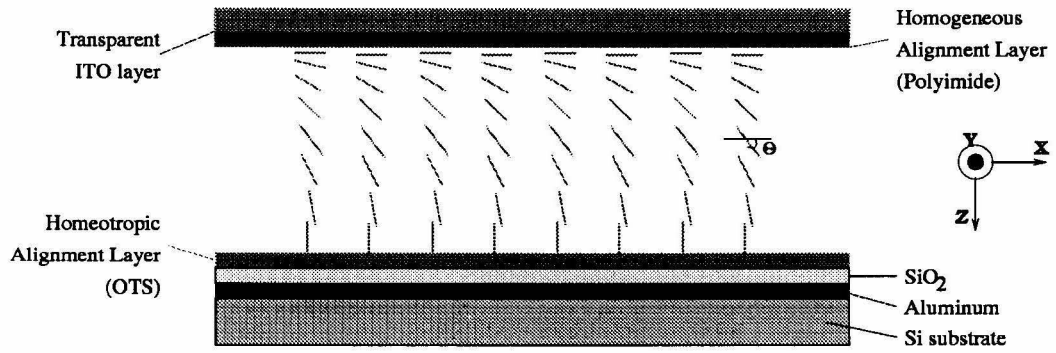


Figure 2.6: Hybrid Alignment Nematic (HAN) configuration.

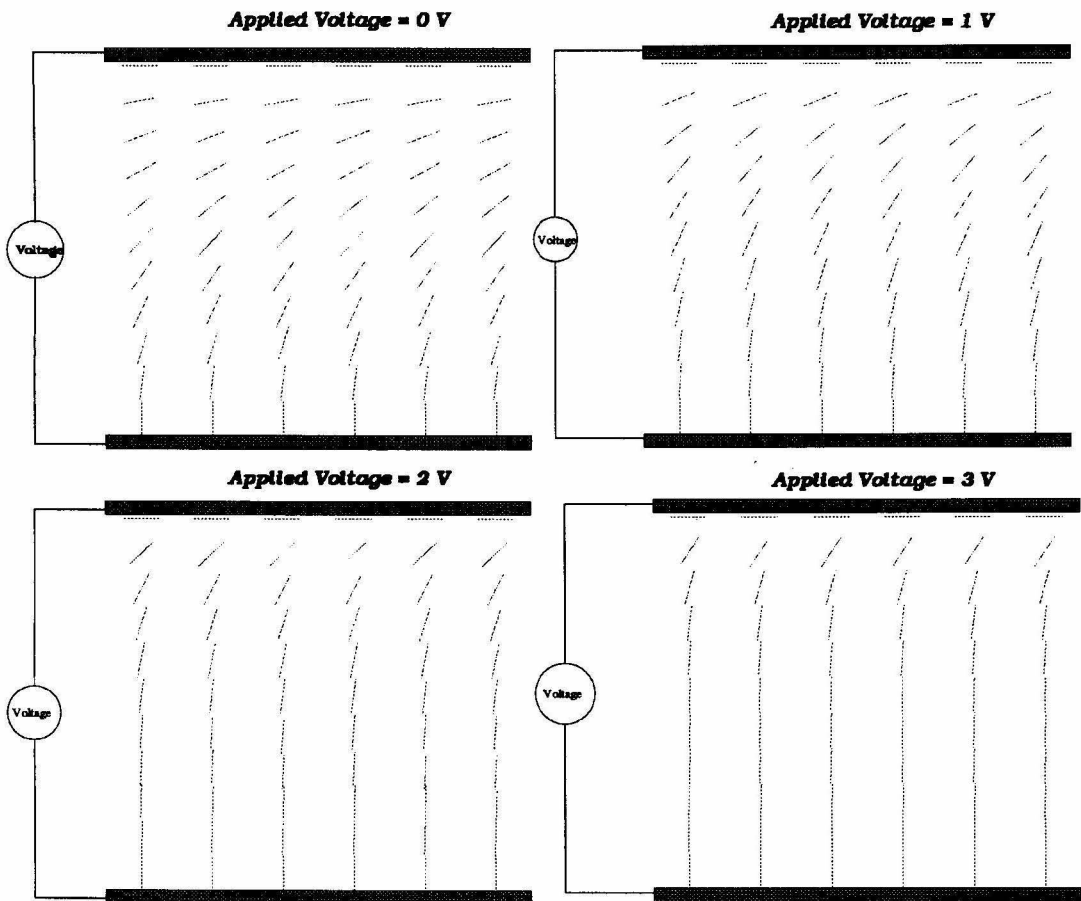


Figure 2.7: Numerical results of HAN orientation angle distribution at different driving voltages.

and the orientation magnitude (orientation angle) corresponds to the magnitude of the driving voltage. However, for the HAN configuration, there are several prominent differences from the homogeneous alignment. First, there is no symmetry of the orientation angle corresponding to the middle of the cell where the biggest orientation angle is located, as with homogeneous alignment. All directors are gradually oriented along the electrical field direction from the perpendicular direction to the parallel direction. Second, there is NO threshold voltage present at all! The refractive index modulation begins right after the driving voltage is on no matter how small it is. This offers the pure analog modulation to the refractive index and relatively faster switching speed than with homogeneous alignment. Although the corresponding index modulation magnitude is less than that with homogeneous alignment, its advantage of lower power consumption is highly desired in some application, such as micro-display product.

2.3 Liquid crystal cell packaging process

2.3.1 Liquid crystal alignment process

Uniform molecular alignment on the glass substrate is desired for fabricating good quality (corresponding to good functionality) liquid crystal devices. Various techniques to obtain uniform alignment have been proposed by many researchers although the real mechanisms of molecular alignment are not yet well understood. The molecular alignment of nematic liquid crystals is believed [7] to depend on (1) physicochemical interactions, such as hydrogen bonding, van der Waal's interactions, or dipole-dipole interactions between liquid crystal molecules and the glass surface (2) mechanical interactions relating to the surface topology and anisotropic elasticity of liquid crystal molecules. The former interaction seems to play a dominant role in orienting molecules parallel or perpendicular to the glass surfaces, and the latter interactions seem to play an auxiliary role, that is, they determine the orientation of molecules in the case of parallel alignment.

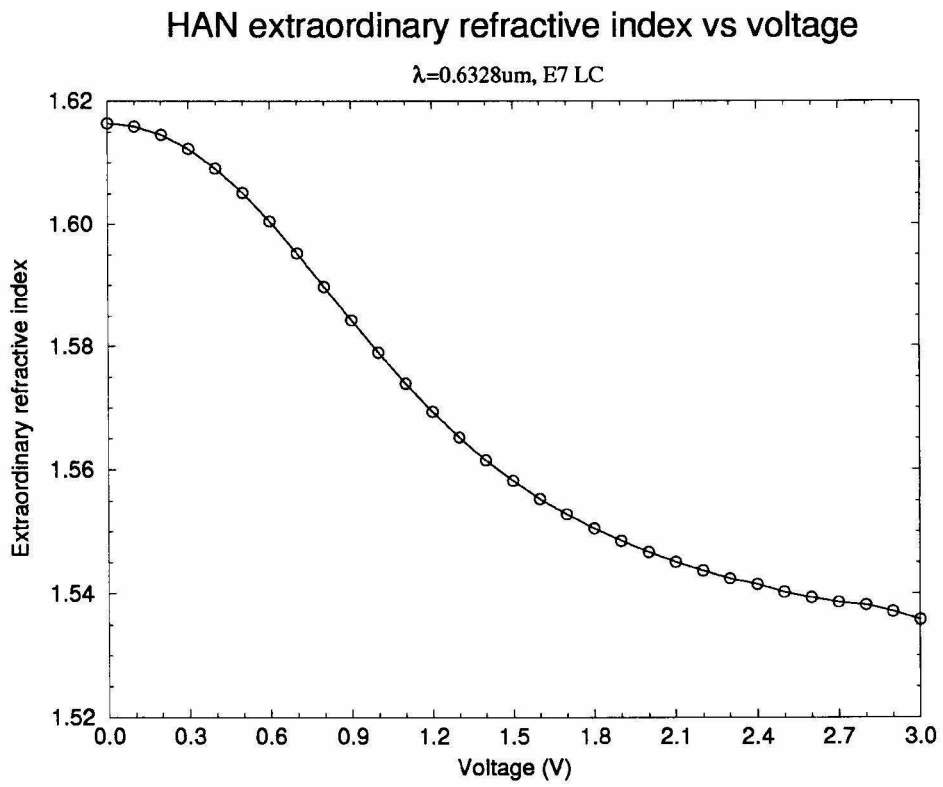


Figure 2.8: HAN refractive index modeling result.

Homogeneous alignment process

A commonly used technique to achieve homogeneous alignment is to spin-coat polyimide and rub the surface with cloth. There are many types of commercially available polyimide, such as Nolimid 32, Dupont 2555, and Merck ZLI 2650 [8].

Our fabrication process (shown in Figure 2.9) is as follows: First, a glass plate is coated with a $20\ \Omega$ per square indium-tin-oxide (ITO) transparent electrode to form the ITO glass. A polyimide solution (1% mass in N-Methyl-2-Pyrrolidone (NMP), here NMP is used for the polyimide thinner) is spun onto the ITO glass at 3000 rpm for 40 seconds and then baked at 200°C for 30 minutes. This polyimide-coated ITO glass is then rubbed unidirectionally on a cloth to form a uniaxially buffered alignment layer. The two pre-treated ITO glasses are affixed together, at a microscopic distance set by small drops of a mixture of chopped glass fibers and Norland91 UV-cured optical adhesive, which are deposited on the periphery of the active area of the cell. The resulting cavity is filled with Merck E7 in isotropic phase, i.e., filling at 75° . The mesogenic substance finally enters the nematic phase as the device slowly cools down.

The orientation mechanism along the rubbing direction has been satisfactorily explained by a simple model [9] which assumes the rubbing produces a series of microscopic grooves where it is energetically more favorable for the optic axis to lie along the grooves rather than across them. This explanation has also been verified by our work in liquid crystal blazed grating beam steering device, where we exploited those E-beam lithography-generated tiny grooves as the natural homogeneous alignment layer (see Chapter 4).

There are also some other alignment techniques to achieve homogeneous alignment. One is using oblique evaporation of silicon monoxide to control the tilt angle by varying the evaporation angle [10]. However, the evaporated film has to be compatible with the high temperature process, and the packaging cost is increased by using vacuum apparatus. Even more, it is unsuitable for large area devices because of the difficulty of obtaining a uniform evaporation angle over a wide area. Another

LC Cell Fabrication Process Diagram

1, Cleaning ITO glass



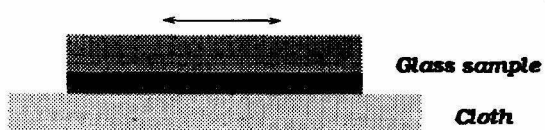
2, Spin coating PI (1%wt) or OTS (2%wt)
3K RPM, 40 second



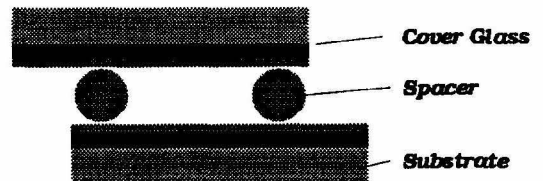
3, Baked at 200 degrees for 30 min



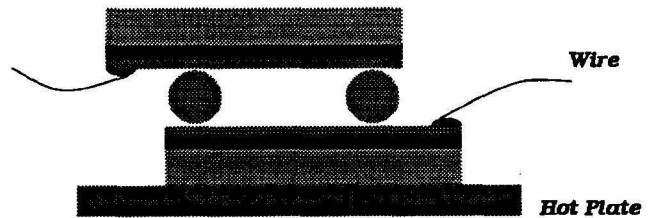
4, Rubbing gently with cloth (PI case only)



5, Packaging with UV cured Spacer



6, Wiring; 70 degrees hot plate for 5 min



7, Drop LC into cavity; Cool down

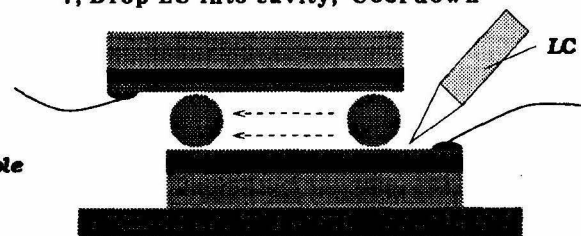


Figure 2.9: Liquid crystal cell package process flow chart.

technique is to use a PVA (Polyvinyl alcohol) coating [11]. This technique can avoid rubbing the surface so that it is quite suitable for a surface sensitive application, such as LCD manufacturing. However, PVA alignment is found to deteriorate with high temperature and humidity. Hence it is not used as the alignment layer in the LCD industry these days.

Homeotropic alignment process

Almost all surfaces receiving homeotropic alignment are treated by some kind of surface coupling agents that have perpendicularly aligned alkyl chains or fluorocarbon chains, and this kind of surface clearly has low energy [7]. We are using Octadecyltriethoxysilane (OTS) as the surface anchoring agent. The whole process is pretty much the same as that for homogeneous alignment except that 2% mass OTS solution is in place of 1% mass Polyimide solution and no rubbing procedure is needed. Homeotropic alignment is used in our liquid crystal on silicon (LCOS) beam steering device application. More details for the LCOS device package are illustrated later in Chapter 3.

2.3.2 Package process monitoring technique

For the previously described packaging process, the cell thickness depends on the spacer size, glue density, as well as the pressure of putting the coverglass on top of the substrate layer. A simple qualitative method for monitoring the cell thickness is to observe the color interference fringes under ambient light. This technique could be also used for monitoring the parallelization of two layers, which is quite important to achieve the uniformity of electrical field inside the whole cell. In order to quantitatively monitor the packaging process, however, the above discussed electro-optics analysis turns out to be a powerful tool.

Figure 2.10 is the experimental setup to check the packaging process, mainly the cell thickness check. A packaged liquid crystal cell is put between a crossed polarizer pair with its alignment direction (optical axis) 45° to the incident beam's polarization

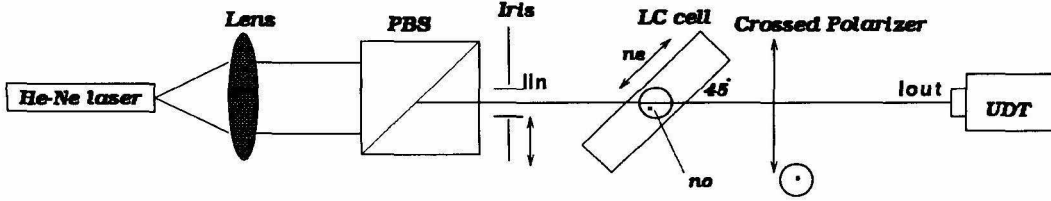


Figure 2.10: Liquid crystal cell package testing experimental setup.

direction. As shown in Figure 2.11 clearly, if the input amplitude is A , then the output amplitude is $B-C$ that can be represented as:

$$B - C = A \cos \beta e^{i\delta_e} \sin \beta - A \sin \beta e^{i\delta_o} \cos \beta \quad (2.7)$$

where β is the angle between IN polarizer and alignment axis, δ_e and δ_o are the phase delays of extraordinary and ordinary light respectively after passing through the liquid crystal medium. Define $I_{in} = |A|^2$. So the output intensity is given by:

$$I_{out} = I_{in} \sin^2 2\beta \left| \frac{e^{i\delta_e} - e^{i\delta_o}}{2} \right|^2 \quad (2.8)$$

Here $\beta = 45^\circ$, define phase delay between extraordinary and ordinary light after passing through the liquid crystal medium $\delta = \delta_e - \delta_o$, the final output intensity is:

$$I_{out} = I_{in} \sin^2 \left(\frac{\delta}{2} \right) \quad (2.9)$$

Since the index modulation is only a function of the driving voltage and it is independent of cell thickness, the phase delay is then only a function of the thickness for the same driving voltage. By measuring the intensity variation with the voltage, and comparing with the numerical modeling results of different cell depths, we can easily define the cell's real thickness. Figure 2.12 shows the cell thickness test results. The

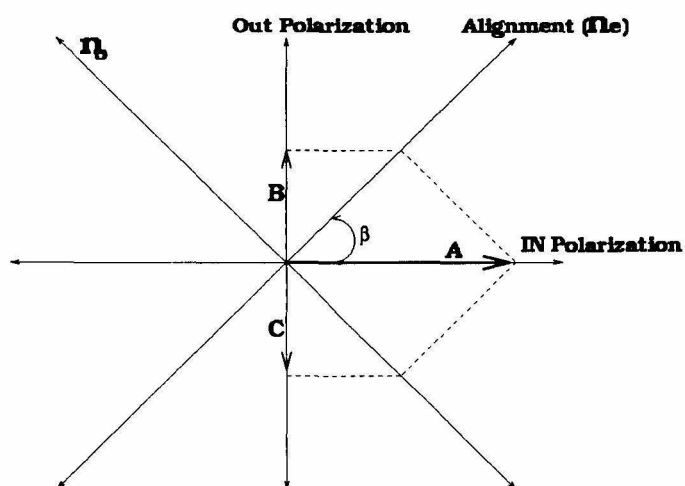


Figure 2.11: Output intensity is a function of phase delay difference between ordinary and extra-ordinary light with crossed polarizer setup.

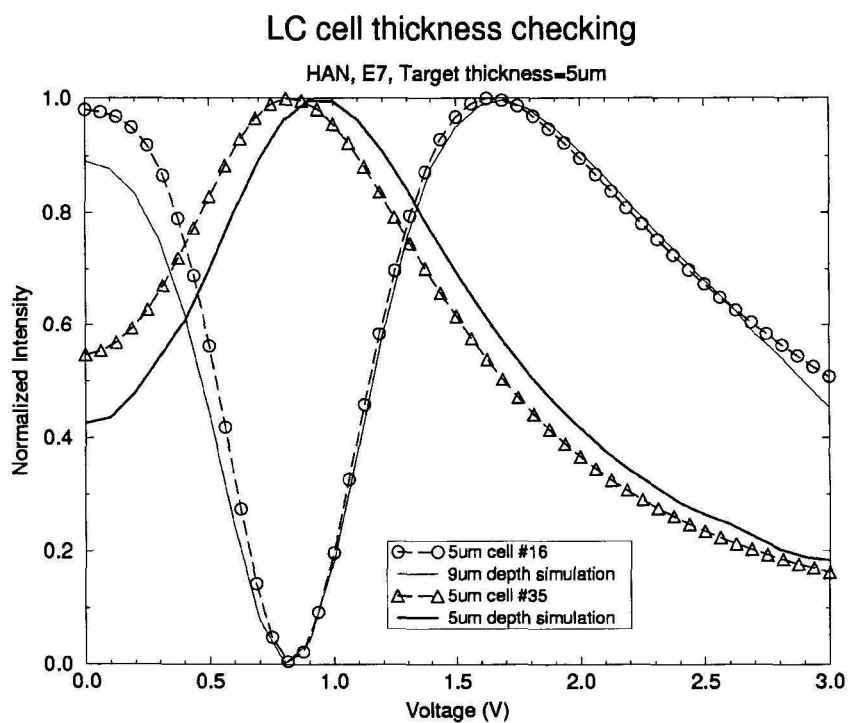


Figure 2.12: Liquid crystal cell thickness check.

targeting cell thickness is $5\mu\text{m}$ with the packaging spacer of $5\mu\text{m}$. Through testing results, sample #35's performance agrees well with $5\mu\text{m}$ cell numerical modeling results while sample #16's performance actually agrees quite well with the $9\mu\text{m}$ cell's simulation. The reason that sample #16 has a larger thickness could be partially explained by the fact that two $5\mu\text{m}$ fiber spacer might somehow add on the same location so that actually a spacer about $10\mu\text{m}$ thickness is used. This experiment clearly demonstrates the power of our numerical analysis of liquid crystal electro-optics and the necessity/importance of a good reference tool for monitoring the fabrication process.

Chapter 3 Liquid crystal on silicon (LCOS) beam steering device

Non-mechanical beam steering devices have many applications in optical interconnects [12], optical fiber communication [13], projection displays [14] and optical data storage [15]. Recently, there have been several non-mechanical beam steering devices developed by different research groups. However, these devices either require high voltage operation, such as electro-optic crystal deflectors [16] and PLZT deflectors [17], or require costly technology, for example, the silicon-ion implantation technique is needed for the phased array beam deflector [18]. With its low driving voltage and mature (low cost) fabrication technology, liquid crystal seems to be an ideal candidate for beam steering devices. The effort of developing liquid crystal beam deflectors can be traced back to the early 1970s. In the 1970s, Borel [19] patented an idea to steer the beam with a liquid crystal diffraction grating, where the binary rectangular diffraction grating is used as the carrier of liquid crystal. Its steering efficiency is very low due to the grating's binary phase. Fray [20] demonstrated another index matching approach using a prism as the light coupling component. This mechanism works reasonably well, and it is still used in some applications. In the 1990s, Dorschner [21] patented an optical phased-array beam steerer, where the well-known phased-array technology used in microwave radar is adopted to the optical frequency domain. The main idea is as follows: a prism inserted in the aperture of an optical system would introduce an optical path delay (OPD) which is greater on one side of an aperture than the other side. This tilts the phase front across the aperture, thereby steering the optical beam. It offers high steering efficiency and large steering angles. However, its complicated special fabrication process as well as the dispersion problem limits its applications. After that, several groups have been working on this technology to improve the spectral response as well as the dispersion compensation.

As we can see, although there are many different mechanisms to operate this kind of beam steering device, the essential idea is pretty much the same, where the diffraction (blazed) grating is used as the key component to deflect the incoming light. It seems that the future research direction should be concentrated on high performance and low fabrication cost. We have proposed and developed two kinds of liquid crystal beam steerers that will be described in the following two chapters.

A low cost, high performance reflective type liquid crystal beam deflector based on Liquid Crystal On Silicon (LCOS) technology [1] is demonstrated in this chapter. Seven steering angles with as high as 92.7% steering efficiency have been achieved from the prototype and it can be operated faster than video rate. To the author's knowledge, it is the first report of phased array type liquid crystal beam deflector using commercially available MOSIS foundry and HAN configuration. Comparing with the other reported phased array liquid crystal beam steering device [18], this deflector is capable of true gray-scale or analog phase modulation at very low voltage, and the fabrication cost is very low, which is quite attractive for some budget-tight application. For information processing applications, its relative low speed, compared with those ferroelectric type counterparts, is dramatically offset by its low fabrication cost, and ease of use of the nematic liquid crystals. Furthermore, it is ideally suited for some applications where the main concern is not high speed or other components are limiting the system's speed.

The device's operation principle is introduced first, followed by the design considerations. Then the fabrication process is described and the device characterization results as well as the discussion, such as fringe field analysis, hologram recording experiment, and programmable deflector design, are presented.

3.1 Introduction

Figure 3.1 shows the cross section view of this reflective type beam steering device. A custom designed VLSI chip is used as the substrate. A thin transparent glass coated with ITO layer is mounted on top of this VLSI chip, separated by the fiber spacer of

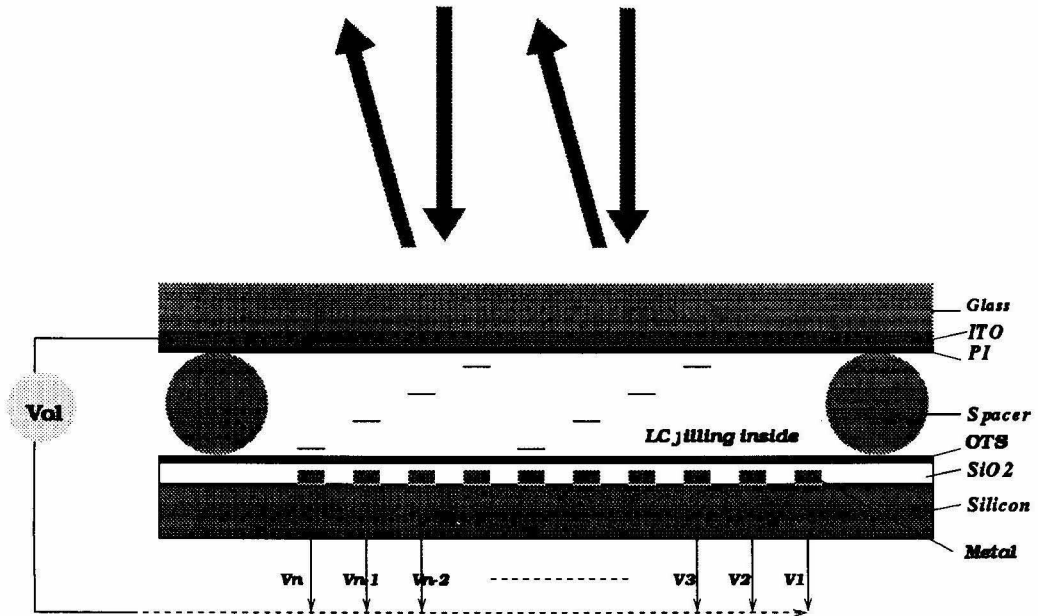


Figure 3.1: Liquid crystal on Silicon (LCOS) beam deflector.

a few microns. A thin layer of nematic liquid crystal is sandwiched between the VLSI die and the transparent cover plate. The metal electrodes patterned on the VLSI chip and the transparent metal layer coated on the cover plate electrically drive the liquid crystal to change the refractive index (or phase) information of the incident light. So it is essentially a phase modulator. Obviously, if a blazed phase grating can be set up on top of this VLSI chip, the incident light will be deflected to blaze with very high efficiency at a certain diffraction order depending on the phase modulation.

Exploiting the electro-optic effect of nematic liquid crystal, where the liquid crystal's refraction index for extraordinary light is continuously changed with the driving voltage, by assigning appropriate voltage distribution along the metal electrodes in the VLSI chip, a virtual blazed phase grating can be built inside this liquid crystal light modulator to steer the incident light to a certain angle. The way to achieve multiple steering angles is to dynamically program this virtual blazed grating's period since the steering angle is a function of the grating period. Figure 3.2 illustrates the

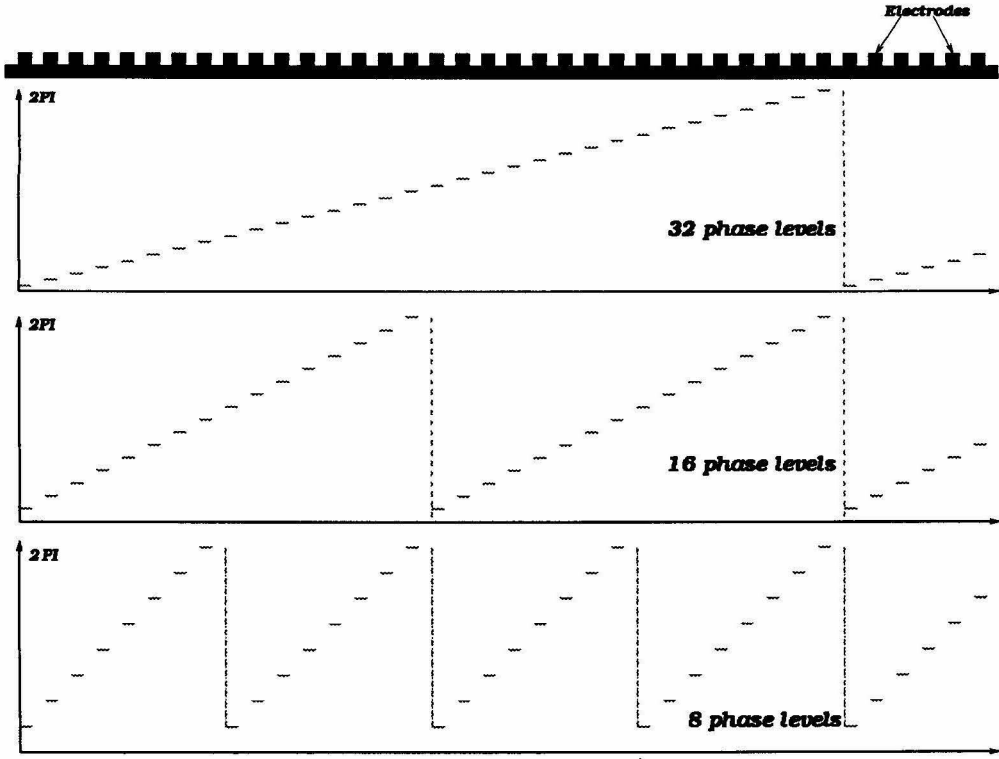


Figure 3.2: LCOS multiple angle addressing approach.

multiple angle addressing approach. On the VLSI chip, 512 conductive electrodes are patterned over a 6.1mm x 3.6mm active area with $8\mu\text{m}$ wide upon $12\mu\text{m}$ centers. In order to minimize the wiring connection overhead, those electrodes are grouped into 16 subgroups; i.e., electrode 1, 33, 65, ..., 481 share the same output pad. This relaxes our wiring overhead from 512 to 32; however, it limits the number of steering angles at the same time. Obviously, if we repeat the same voltage assignment every 16 pads, then the virtual blazed grating period is half so that a twice larger steering angle can be obtained. To ensure high efficiency, the minimum number of phase levels is chosen as 8; therefore, 3 different steering angles can be obtained at each side for this device. (From experiment, 4 phase level can also get blaze angle, but its efficiency is not so good as that from those larger number of phase levels.) Applying the nematic liquid crystal's electrical non-polarity response, the opposite direction blazed grating can

also be built up so that another 3 angles could be obtained on the other side; this gives us the total addressable angles of 7. More steering angles can be easily obtained by increasing the chip die size, or using a smarter addressing approach, which will be introduced later in this chapter.

There is one more issue needed to be addressed here. As we can see from Figure 3.1, liquid crystal is driven by the voltage applied to the ITO layer of coverglass and the electrodes patterned within the VLSI chip. Notice that there is a protection SiO_2 layer on the top of those electrodes, which is called overglass layer in VLSI design methodology for preventing all the underneath circuits from outside electric static discharge (ESD). Due to the poor conductivity of SiO_2 , the voltage actually driving the liquid crystal is less than the voltage applied. In fact, this driving voltage loss calculation can be determined from the Maxwell equation's boundary condition of electrical field:

$$\vec{D}_{LC_n} - \vec{D}_{SiO_2_n} = \sigma = 0 \quad (3.1)$$

Where \vec{D} is the electric displacement, σ is the surface charge density which is zero in our analysis. Plug in the corresponding dielectric constants of liquid crystal and SiO_2 , with the reported overglass thickness of $0.6\mu m$ for Orbit $2.0\mu m$ CMOS process [22], the final results shows that about 40% of the applied voltage is lost across this SiO_2 layer.

3.2 Design considerations

3.2.1 Liquid crystal analysis

First, the hybrid alignment nematic (HAN) [10] configuration is chosen. There are two reasons that we chose the HAN configuration rather than the commonly used homogeneous alignment configuration: (1) The HAN configuration has no threshold voltage for the onset of the liquid crystal's electro-optic response, which generally occurs for the homogeneous alignment configuration. Therefore, it can provide the full

analog phase modulation, which ensures a very low driving voltage compared with the homogeneous alignment configuration. (2) It is not easy (not cost-saving in that sense) to make a homogeneous alignment on top of the VLSI chip surface since the common surface-rubbing method will damage the chip bonding wires if not using a custom designed special rubbing machine. On the other hand, the homeotropic alignment can be easily formed by spin-coating the VLSI chip surface with Octadecyltriethoxysilane (OTS), which is a surface coupling agent inducing vertical anchoring of the liquid crystal molecule.

The refractive index (or phase) information obtained from the HAN molecule director orientation simulation (see Chapter 2) is the starting point of the device's diffraction analysis. Obviously, this diffraction analysis will be helpful for our comparison between theoretical predictions and experimental results. Even more important, it can be used to optimize the device's performance. In other words, with the help of this diffraction analysis, we can find the optimal voltage assignment along the electrodes where the highest diffraction efficiency can be achieved.

3.2.2 Diffraction analysis

A detailed analysis on “virtual” blazed grating's diffraction is carried out to guide through the whole design procedure. Figure 3.3 shows the cross section view of this deflector. The light penetrates the coverglass, liquid crystal, and SiO_2 , then is reflected back from either the silicon substrate or the metal electrodes. Due to different reflectivity of the silicon substrate and metal electrodes, this “virtual” blazed grating is actually an amplitude plus phase grating; we call it a mixed type blazed grating. Given the relatively large grating period (about $96\mu\text{m}$ minimum for 8 phase levels), the scalar theory is used. A strict vector theory is needed if the feature size of the electrodes are made smaller in the future. For the modeling, each electrode can be considered as a slit whose complex amplitude transmittance at the surface of the coverglass after a round-trip in the cavity is defined by the metal reflectivity and phase delay. It is marked as “region10, region20, ...” in Figure 3.3. The spacing

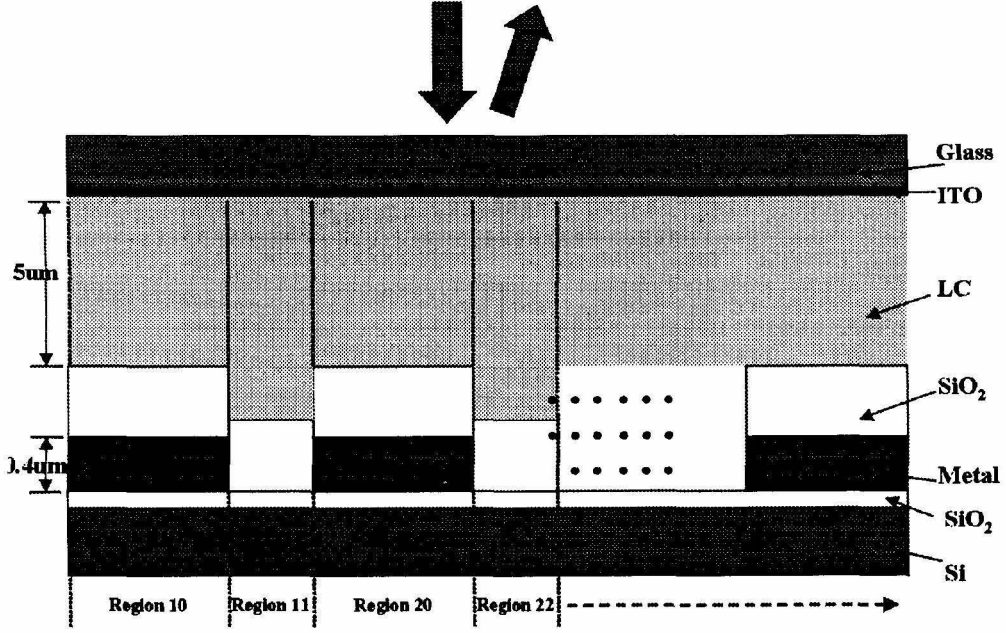


Figure 3.3: LCOS deflector diffraction modeling.

between electrodes can be treated in the same way as marked by “region11, region21, ...” in Figure 3.3. Each subgroup then can be considered as a “virtual” prism whose transmittance is the summation of all transmittance of each electrode and spacing within one subgroup. The transmittance $A(x)$ of each subgroup with 32 electrodes is given by:

$$\begin{aligned}
 A(x) = & \text{rect}\left(\frac{x-4}{8}\right)A_{10}e^{i\phi_{10}} + \text{rect}\left(\frac{x-10}{4}\right)A_{11}e^{i\phi_{11}} + \\
 & \text{rect}\left(\frac{x-16}{8}\right)A_{20}e^{i\phi_{20}} + \text{rect}\left(\frac{x-22}{4}\right)A_{21}e^{i\phi_{21}} + \dots + \\
 & \text{rect}\left(\frac{x-378}{8}\right)A_{320}e^{i\phi_{320}} + \text{rect}\left(\frac{x-384}{4}\right)A_{321}e^{i\phi_{321}}
 \end{aligned} \quad (3.2)$$

where ϕ_{10} and ϕ_{11} are the phase delay for region 10 and region 11 after round-trip respectively. A_{10} and A_{11} are the amplitude reflectance for region 10 and region 11 after round-trip respectively. From standard Fourier optics [23], the whole blazed grating can be considered as a periodic slit array convolved with a tiny prism at each

slit. The whole grating's transmittance $T(x)$ can then be represented as $T(x) = A(x) * G(x)$, where $G(x)$, generated by the slit array, is the grating envelop transmittance that is given by:

$$G(x) = \sum_m \delta(x - mp) \text{rect}\left(\frac{x}{W}\right) \quad (3.3)$$

where p is the length of each subgroup and W is the whole illumination width. Finally, the far field distribution is the Fourier transform of the whole grating's transmittance $T(x)$:

$$F.T.\{T(x)\} = F.T.\{A(x) * G(x)\} = F.T.\{A(x)\} \bullet F.T.\{G(x)\} \quad (3.4)$$

In the diffraction analysis, we calculate the diffraction efficiency for two cases, which are the linear phase assignment and linear voltage assignment along each electrode subgroup. Although the linear voltage assignment has simple off-chip driving circuitry, it does not produce the linear blazed phase distribution due to the liquid crystal's nonlinear relationship between driving voltage and refractive index. The voltage distribution which generates linear phase could be easily defined through the calculation results shown in Figure 2.8 in Chapter 2. This voltage distribution is called the optimal voltage assignment in the following. The diffraction analysis comparison between the optimal voltage assignment and the linear voltage assignment is shown in Figure 3.4. As we can see clearly, the performance of the optimal voltage assignment case is much better than that of the linear voltage assignment case. The diffraction efficiency is increased from 82% to 98% and the contrast ratio jumped from 7.4 to 78. Due to reasons explained later, we will use the intensity contrast ratio rather than diffraction efficiency when comparing with experiment results.

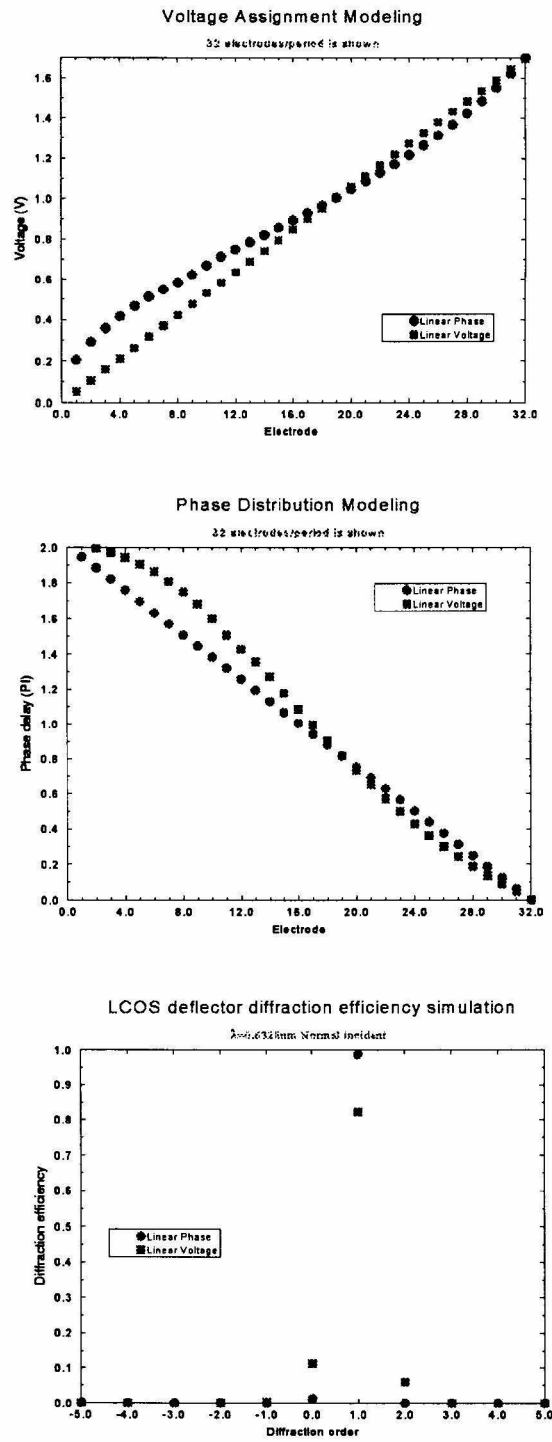


Figure 3.4: Diffraction efficiency simulation comparison between optimal voltage assignment and linear voltage assignment along the electrodes.

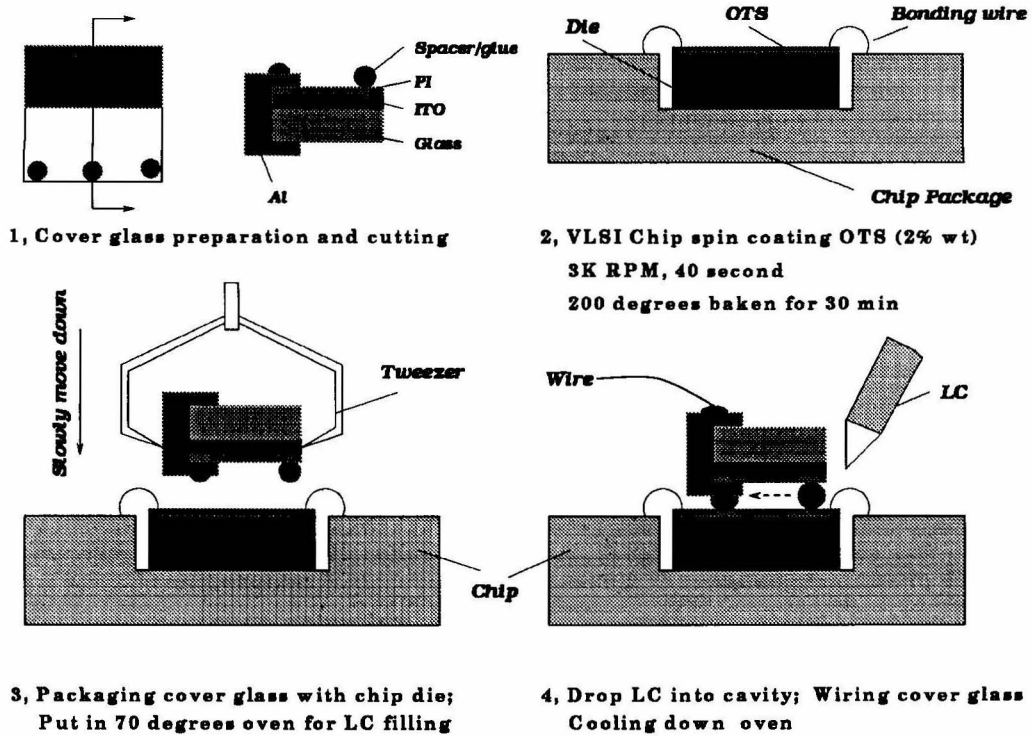


Figure 3.5: Custom developed LCOS deflector packaging process.

3.3 Fabrication

A customized fabrication process, which is fully compatible with the Orbit 2.0- μm CMOS technology provided by MOSIS, is developed to make this novel liquid crystal modulator on top of the VLSI chip just through a few simple post-processing steps. Figure 3.5 illustrates the whole packaging process. A medium chip (4.6mmx6.8mm) is designed for the bottom VLSI chip while the metal electrodes patterned inside this chip is made with the first metalization level of the Orbit 2.0 μm process, since the second level metal of that process is reported to have poor surface quality. These patterned electrodes are used to apply voltages across the modulator and as the optical mirrors. The topmost layer of the whole chip is the silicon dioxide layer which protects the underneath circuits and helps OTS, the homeotropic alignment surface coupling agent, to bind to the surface of the die. An OTS solution (2% mass in Ethyl

Alcohol-200) is spun onto the chip die at 3000 revolutions per minute (RPM) for 40 seconds and then baked at 200°C for 30 minutes. This low temperature operation does not affect the electrical circuit performance. The cover glass plate is coated with a 20 Ω per square ITO transparent layer and spin coating/rubbing polyimide solution (1% mass in 1-Methy-2-Pyrrolidinone), the homogeneous alignment surface coupling agent. Aluminum is evaporated onto one edge of the cover glass plate to allow a good wire contact to the ITO back plane. A 5 μ m thick spacer, which consists of a mixture of chopped glass fibers and Norland 91 UV-cured optical adhesive, connects the cover glass plate and the substrate chip. During this chip packaging procedure, the ITO coverglass should not touch the chip bonding wires, which otherwise could short the circuitry inside the chip. The final resulting cavity is filled with Merck E7 liquid crystal in the isotropic phase. The mesogenic substance enters the nematic phase as the device slowly cools down.

Compared with the ferroelectric liquid crystal device's small cell gap (usually on the order of 1~ 2 μ m), the larger cell gap of our nematic liquid crystal device relaxes the strict surface topology requirement, which makes the fabrication process less painful and cost-saving, since we do not generally need a planarization treatment to improve the surface uniformity as the ferroelectric liquid crystal device normally does. This is also why our LCOS modulator's substrate can still be safely fabricated by the low-cost commercially available MOSIS service, even with its infamous 0.3 ~ 0.8 μ m surface roughness contributed by the overglass layer.

3.4 Characterization

3.4.1 Experiment setup

Figure 3.6 is the experimental setup for the LCOS deflector's characterization. The device is illuminated by a collimated polarized beam at 632.8nm with about 2° incident angle. The liquid crystal is driven by a 1-kHz DC-balanced square wave of variable amplitude through a custom designed liquid crystal driving board. A computer

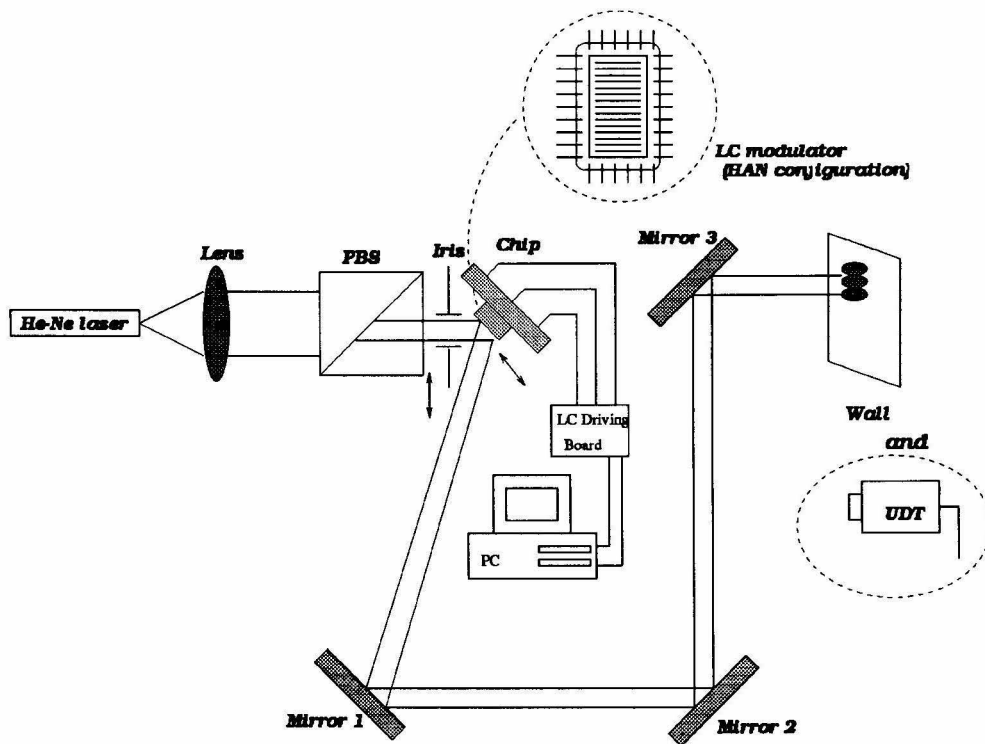


Figure 3.6: Characterization setup of LCOS deflector.

controls the driving board to program the voltage assignment to different electrodes. The output far field beam spots are collected using a power meter connected with a computer I/O interface. The picture of the device as well as the liquid crystal driver board is shown in Figure 3.7. Since the refraction index of liquid crystal only changes

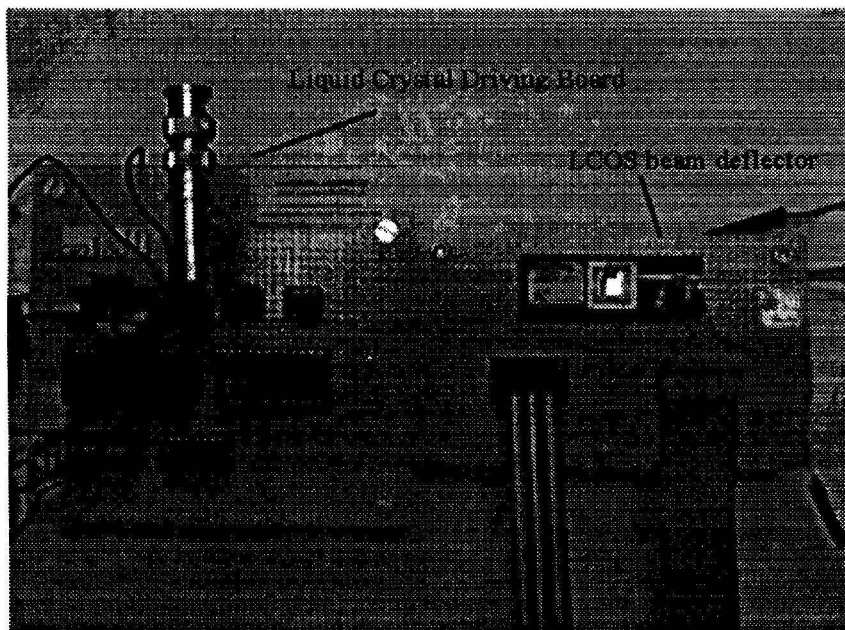


Figure 3.7: Picture of LCOS deflector and liquid crystal driver board.

with the driving voltage for the extraordinary light, this LCOS deflector actually is a polarized beam steering device. The linear polarized incident beam must have the same polarization direction as the cover glass plate's rubbing direction which is the extraordinary axis (optical axis) of the liquid crystal.

Considering that the device itself is a high frequency grating (with a grating period of 12 μ m, duty cycle of 2/3) even with no voltage applied, we used a slit to collect the zero order only. Those higher orders generated from this high frequency grating are all blocked in our experiment. This makes it difficult to calculate the experimental diffraction efficiency for later comparison with numerical modeling. Considering the relative large optical absorption coefficient for E7 being about 55cm⁻¹ and the energy loss by absorption/reflection/scattering through the VLSI chip, we use the steering

efficiency rather than the diffraction efficiency to characterize the device. The steering efficiency is always normalized to the off-state (without voltage applied) zero order intensity. The diffraction analysis discussed before can be applied here through the intensity contrast ratio between the strongest and the second strongest order.

3.4.2 Optimal voltage vs linear voltage

We carried out a comparison experiment with a linear voltage distribution and an optimal voltage distribution applied respectively. The experimental data is plotted in Figure 3.8. It is shown that the linear voltage distribution case demonstrated an

LCOS deflector optimal voltage vs linear voltage distribution

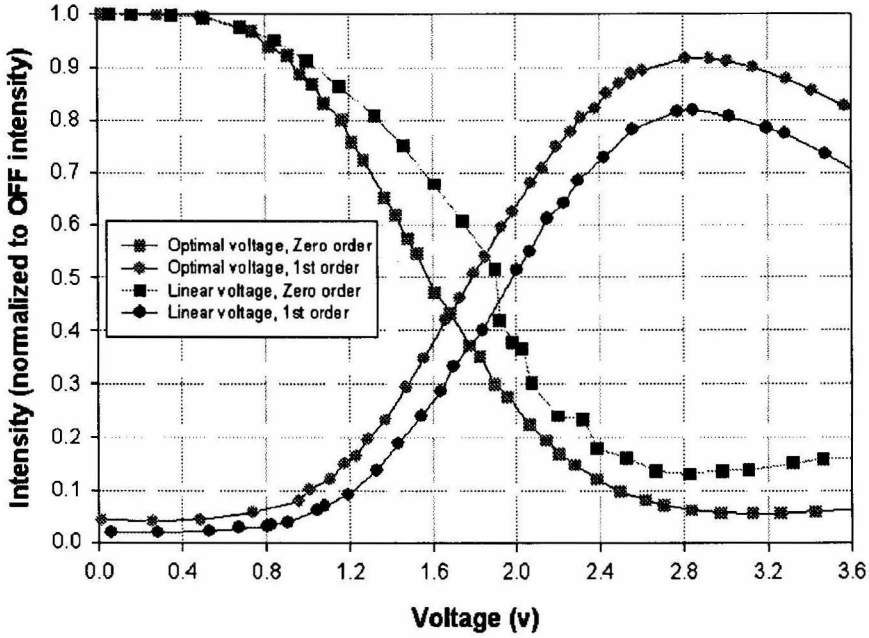


Figure 3.8: Experimental data comparison between optimal voltage assignment and linear voltage assignment along the electrodes.

intensity contrast ratio of 6 and it agrees very well with the theory prediction of 7.4. While the optimal voltage distribution case achieved an intensity contrast ratio of 18, which also agrees well with 78 from the theory prediction. (Notice that the contrast

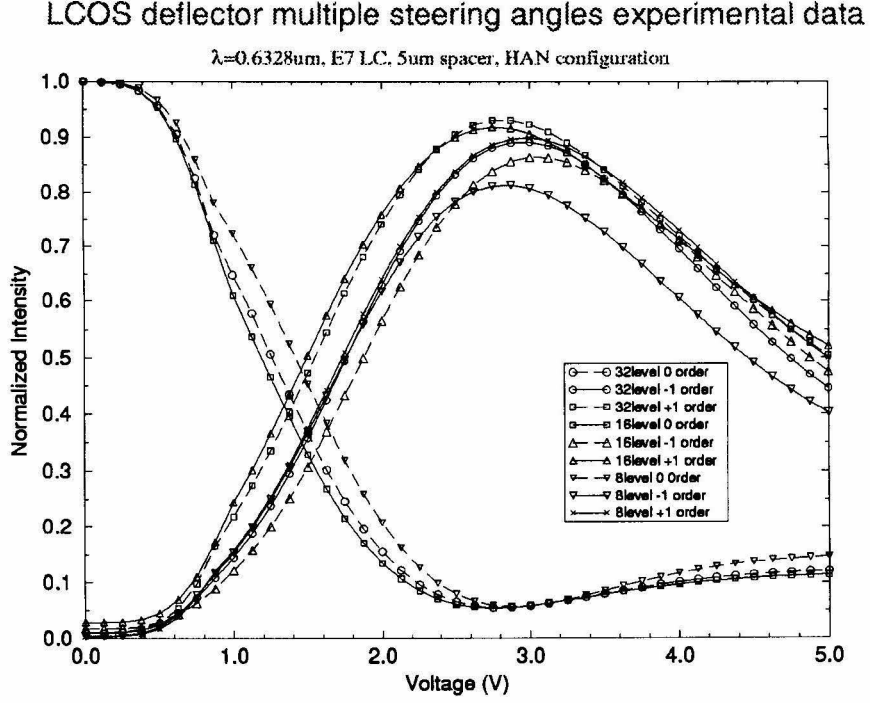


Figure 3.9: Measurement data of those 7 steering angles.

ratio begins to vary dramatically when it reaches high efficiency. For simplicity, just taking into account two diffraction orders, 80% diffraction efficiency gets a contrast ratio of 4, 82% gets 4.5, but 96% gets 24 and 98% gets 49! This is why we say the agreement is good.)

3.4.3 Multiple steering angles

Seven dynamically addressable angles with very high steering efficiency have been achieved. The measurement data is listed in Figure 3.9. As mentioned before, the steering efficiency is normalized to the ZERO order intensity with no voltage applied. Experimentally, the LCOS deflector with 32 electrodes as each subgroup has demonstrated as high as about 92.7% steering efficiency. With the reduction of the number of electrodes for each subgroup, the steering efficiency slightly drops. This issue will be discussed in great detail later in the fringe field section. Nevertheless, the largest

supplied operation voltage is about 2.85V, which is corresponding to an actual liquid crystal driving voltage of 1.71V, considering the 40% voltage loss discussed previously. From the calculation result of refractive index with voltage for the HAN configuration in Chapter 2 (see Figure 2.8), the calculated 2π phase delay voltage for our LCOS deflector is about 1.7V for this device, which agrees very well with the above voltage loss estimation. Figure 3.10 shows beam spot picture of those 7 steering angles (0° , 0.1° , 0.2° , and 0.4°) with corresponding driving conditions as well as virtual blazed grating periods.

Finally, we measured the response time of this LCOS deflector by observing the first diffraction order intensity's time variation when 2.85V applied voltage is on. The measured rising and falling time are about 9ms and 20ms respectively, which are shown in Figure 3.11. Here we gain some advantages in response time by using reflection operating mechanism since it offers faster switching speed than its transmission type counterpart which requires a thicker liquid crystal layer. This level of response time allows the device to operate at video-rate (30 Hz) so that it could be used for a large screen projection display or a micro-display. Even more, the device's response time can be further improved by driving it with larger voltages, since the response time of nematic liquid crystal is proportional to the magnitude of the driving voltage. Another approach to achieve a faster switching speed is to use ferroelectric liquid crystal (FLC), which can reach micro-second level response time. However, due to FLC's natural binary operation mode, analog modulation of FLC still remains to be a big challenge.

3.5 Discussions

3.5.1 Fringe field effect

Figure 3.9 shows that, experimentally, the deflector's steering efficiency is lower with smaller grating period, i.e., less electrodes within one subgroup. This observation contradicts the scalar diffraction theory prediction, which says that a diffraction grat-

Beam Steering experimental results








<u>Steering angle</u>		<u>Operation Status</u>
0 degree		Zero voltage
0.1 degree		voltage=2.85v period=384um
0.2 degree		voltage=2.85v period=192um
0.4 degree		voltage=2.85v period=96um
-0.1 degree		voltage=-2.85v period=384um
-0.2 degree		voltage=-2.85v period=192um
-0.4 degree		voltage=-2.85v period=96um

Figure 3.10: Picture of 7 steering angle beam spots.

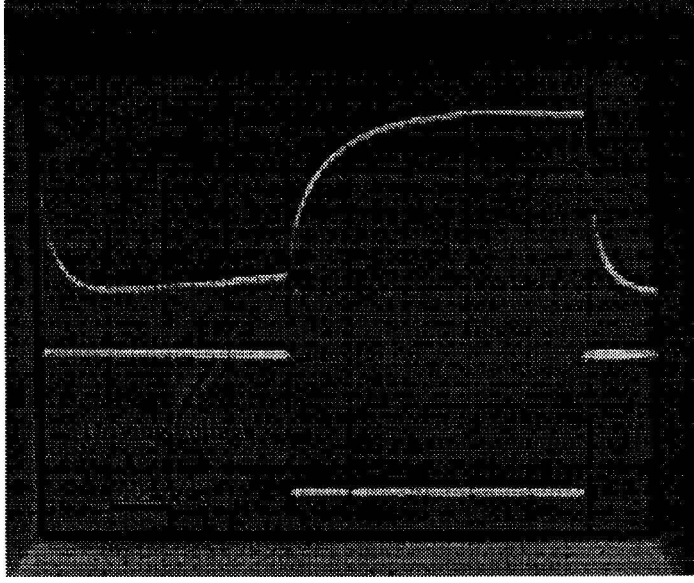


Figure 3.11: LCOS deflector response time measurement.

ing's efficiency is not a function of the grating period. This contradiction could be explained by the so-called "flyback" issue, which is illustrated in Figure 3.12. In short, the flyback is caused by the liquid crystal's visco-mechanical properties. For LCOS deflector, at the transition region of the phase delay changing from one subgroup to the other one, i.e., 2π to 0, there is an orientation angle abrupt change within a limited space (usually a few microns). Physically, liquid crystal molecule director can not change its orientation direction suddenly and it needs a minimum spatial extent to gradually vary its orientation. Taking into account this flyback issue, the diffraction efficiency formula could be represented as

$$\eta = \frac{\sin^2(\frac{\pi}{N})}{(\frac{\pi}{N})^2} \times (1 - \frac{L_F}{L})^2 \quad (3.5)$$

where N is the number of phase levels. For pure analog (blazed) phase shape, N is considered to be ∞ . L_F is the width of the flyback region and is pretty much fixed

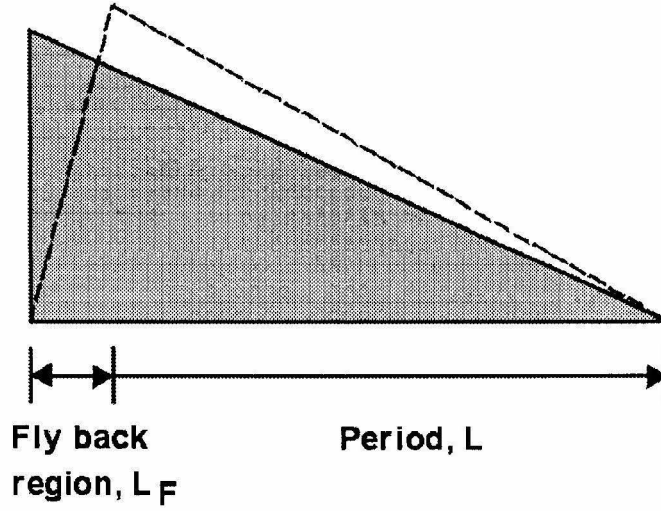


Figure 3.12: Flyback issue.

to be about $4\mu\text{m}$ (the spacing between each electrode) and L is the width of each subgroup, which is decided by the number of phase levels. From Equation 3.5, more phase levels gives larger L so that both first term and second term are larger, which gives out larger diffraction efficiency. This explains why the steering efficiency is a function of grating period as shown in Figure 3.9.

One more issue, previously, we assumed the electrical field distribution along those VLSI chip's electrodes is only existing within each electrode region and stopped at boundary of each electrode. But, in reality, this is not the case. The electric field must be continuously distributed inside the whole medium. Obviously, there is still some electric field distribution between those electrodes, which is the so-called fringe field. Figure 3.13 illustrates the fringe field effect in the LCOS deflector with HAN configuration. Then the current question is that: can we find the molecule director orientation angle as well as the voltage distribution inside the question mark region? The numerical modeling notation is shown in Figure 3.14. For this modeling, basically we need to solve an equation set where two nonlinear partial differentiate equations (PDEs) are coupled together. One is the field equation which defines the electrical

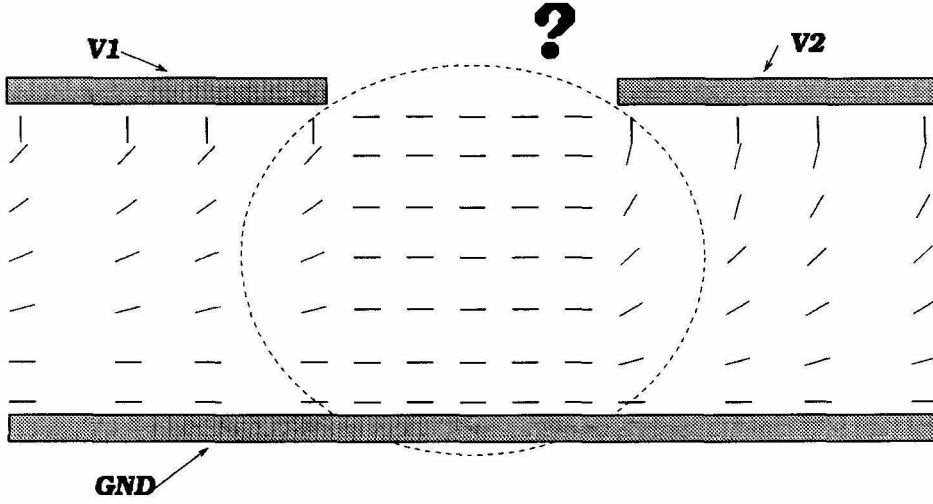


Figure 3.13: Fringe field introduction.

field distribution inside the whole medium.

$$\nabla \cdot \vec{D} = 0 \quad (3.6)$$

Here we assume no free charge inside the whole medium. So it is essentially a Poisson equation. The other one is the molecule director equation which defines the liquid crystal molecule director distribution inside the whole medium. The equation is the 2-D version of Equation 2.1 in Chapter 2.

Let us start with the definition of the electric displacement \vec{D} . As we already knew, liquid crystal is an anisotropic medium, which gives different directions for electrical field and electric displacement due to the vector/tensor property of the dielectric constant. Figure 3.15 shows the relationship between \vec{E} and \vec{D} . From this notation, we have

$$\vec{D} = \vec{D}_\perp + \vec{D}_\parallel = \epsilon_o \epsilon_\perp \vec{E}_\perp + \epsilon_o \epsilon_\parallel \vec{E}_\parallel \quad (3.7)$$

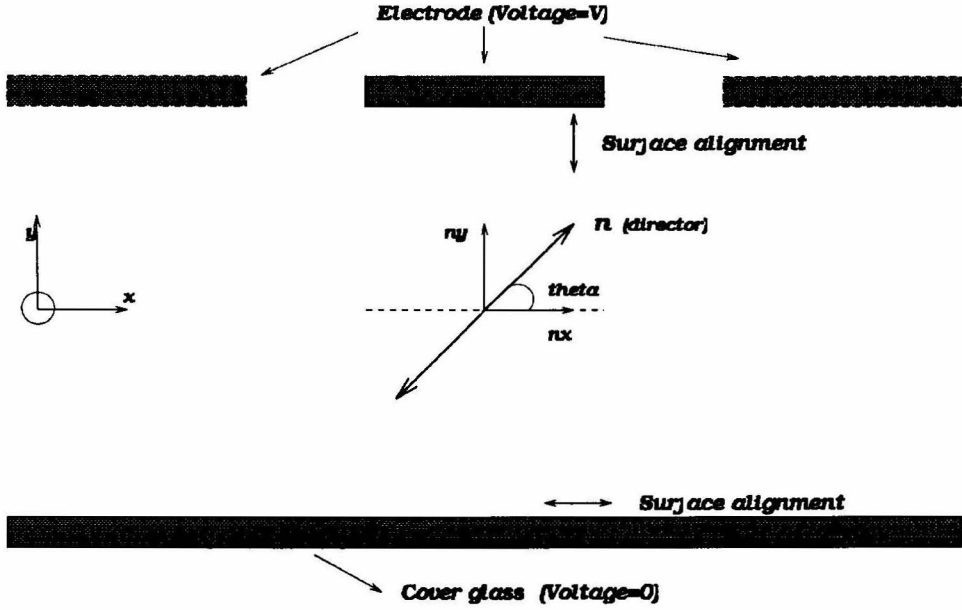


Figure 3.14: Simulation of fringe field effect.

As we can see from Figure 3.15, $\vec{E}_\perp = \vec{E} - \vec{E}_\parallel$ and $\vec{E}_\parallel = (\vec{E} \cdot \hat{n})\hat{n}$, we have

$$\vec{D} = \epsilon_0[\epsilon_\perp \vec{E} + (\epsilon_\parallel - \epsilon_\perp)(\hat{E} \cdot \hat{n})\hat{n}] \quad (3.8)$$

Plugging in this definition of electric displacement \vec{D} into Equation 3.6, we have

$$\begin{aligned} &(\epsilon_\perp + \Delta\epsilon \cos^2 \theta) \frac{\partial^2 V}{\partial x^2} + (\epsilon_\perp + \Delta\epsilon \sin^2 \theta) \frac{\partial^2 V}{\partial y^2} + \Delta\epsilon \sin 2\theta \frac{\partial^2 V}{\partial x \partial y} \\ &+ \Delta\epsilon \left(-\sin 2\theta \frac{\partial \theta}{\partial x} + \cos 2\theta \frac{\partial \theta}{\partial y} \right) \frac{\partial V}{\partial x} + \Delta\epsilon \left(\sin 2\theta \frac{\partial \theta}{\partial y} + \cos 2\theta \frac{\partial \theta}{\partial x} \right) \frac{\partial V}{\partial y} = 0 \end{aligned} \quad (3.9)$$

Through the standard procedure of variational calculus method, after a long derivation, the 2-D liquid crystal molecule director orientation equation is finally

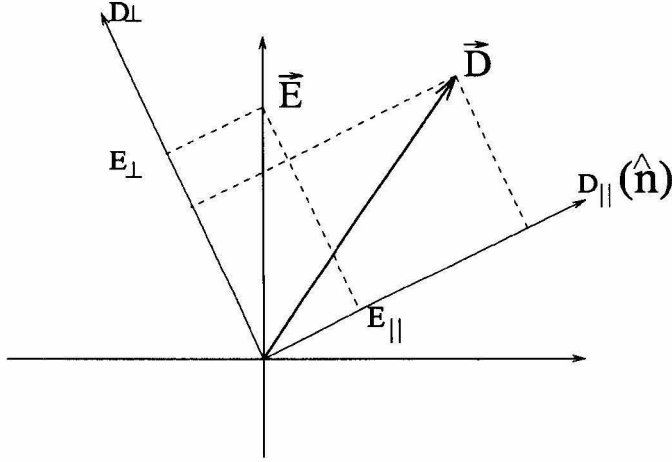


Figure 3.15: Relationship of electric displacement D and electric field E for liquid crystal medium.

obtained as follows:

$$\begin{aligned}
 & (K_{11} \sin^2 \theta + K_{33} \cos^2 \theta) \frac{\partial^2 \theta}{\partial x^2} + (K_{33} - K_{11}) \sin 2\theta \frac{\partial^2 \theta}{\partial x \partial y} \\
 & + (K_{11} \cos^2 \theta + K_{33} \sin^2 \theta) \frac{\partial^2 \theta}{\partial y^2} - \frac{1}{2} (K_{11} - K_{33}) \sin 2\theta \left(\frac{\partial \theta}{\partial x} \right)^2 \\
 & - \frac{1}{2} (K_{33} - K_{11}) \sin 2\theta \left(\frac{\partial \theta}{\partial y} \right)^2 - (K_{33} - K_{11}) \cos 2\theta \frac{\partial \theta}{\partial x} \frac{\partial \theta}{\partial y} \\
 & + \frac{1}{2} \epsilon_o \Delta \epsilon \left[-\sin 2\theta \left(\frac{\partial V}{\partial x} \right)^2 + \sin 2\theta \left(\frac{\partial V}{\partial y} \right)^2 + \cos 2\theta \frac{\partial V}{\partial x} \frac{\partial V}{\partial x} \right] = 0 \quad (3.10)
 \end{aligned}$$

Equations 3.9 and 3.10 builds up a nonlinear coupled partial differentiate equation set. It is almost impossible to analytically solve this equation set without any further assumptions for simplification. We numerically solve this nonlinear coupled PDE by combining the finite difference method and Successive Over Relaxation (SOR) method [4]. The finite difference method basically divides the whole structure into a fine 2-D grid, where each cell can be solved with the known boundary conditions. The whole procedure is essentially using the iteration technique. First, we assume the electrical field distribution V_{ini} is known to solve the Equation 3.10 to get the molecule director distribution θ_{ini} , then using this calculated molecule director distribution

θ_{ini} to solve Equation 3.9 to get electrical field distribution V_{new} , finally iterate those previous two steps to reach a stable solution of electrical field V_{final} and liquid crystal molecule director orientation θ_{final} . After that, we can easily calculate the refractive index distribution inside the whole medium with different conditions since that is the important parameter we need to concentrate on for future application.

As a reminder, our motivation for this fringe field analysis is two-fold: First, to figure out the index distribution in the spacing region between each electrode to see how it helps (or degrades) the device's overall performance. Second, we want to see what is the limitation of this LCOS approach for beam steering when the electrode size is scaled down. Figure 3.16 presents the calculated refractive index distribution along the two electrodes at different driving voltages with the ratio of electrode width and liquid crystal depth to be 1. As we expected, the index rounds off along the electrode's boundary region and a larger driving voltage achieves a bigger index modulation. Also, at zero voltage, the refractive index already has some modulation which is due to the HAN configuration's surface splay-bend conformation. Other than the previous thought that the spacing region between electrodes contributes nothing to the LCOS deflector's index modulation, this region does offer some kind of index modulation whose magnitude actually lies in between those from two neighboring electrodes. This fact turns out to be very helpful for our LCOS deflector to achieve a smoother blazed shape within one subgroup. However, for the phase delay transition between each subgroup, this fact is not good and further deteriorates the flyback issue. Nevertheless, this shortcoming could be compensated for by designing a larger space between each subgroup.

In order to justify this compensation technique, we calculate the refractive index distributions at different driving voltages with the ratio of electrode width over liquid crystal depth as 10. Intuitively, now that the aspect ratio is much larger, the fringe field effect would be greatly suppressed. Figure 3.17 shows clearly this trend. The refractive index at the boundary of the electrodes rounds off very quickly and keeps pretty much flat at the whole center part of the spacing region. Designing a large spacing region between each subgroup not only reduces the fringe field effect due to

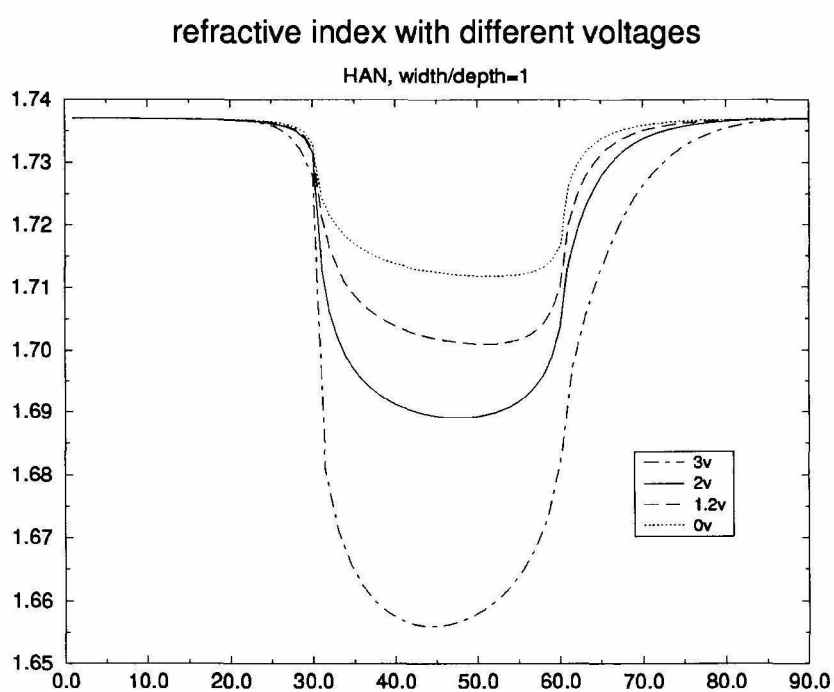


Figure 3.16: Fringe field effect modeling result of refractive index at different voltage with depth/width ratio of 1.

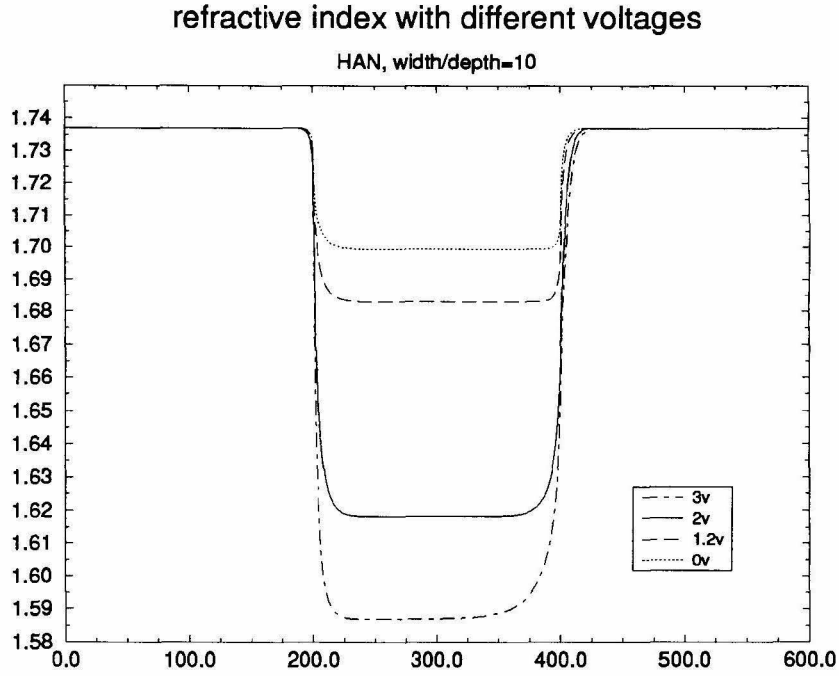


Figure 3.17: Fringe field effect modeling result of refractive index at different voltage with depth/width ratio of 10.

the much smaller index modulation in the spacing region, but also reduces the flyback issue since now we have more spatial extent for the liquid crystal molecule director to relax itself from a large orientation angle to a small one.

After comparing the refractive index distribution at aspect ratio of 1 and 10, a logical step is then to figure out what is the limit of this aspect ratio with a given tolerable fringe field effect. Figure 3.18 shows the refractive index distribution at 1.2V driving voltage with different width/depth ratios. As we can see clearly, the ratio should be at least 5 in order to keep the fringe field negligible. This puts some limitation there of the index modulation for an ultra small geometry device. Nevertheless, as we mentioned earlier, the fringe field is not always a problem. For some application, it might be a good thing, i.e., it helps to smooth the field between electrodes within the same subgroup so that it is quite beneficial for achieving a better blazed phase shape. In short, as long as we can model/control this fringe field effect

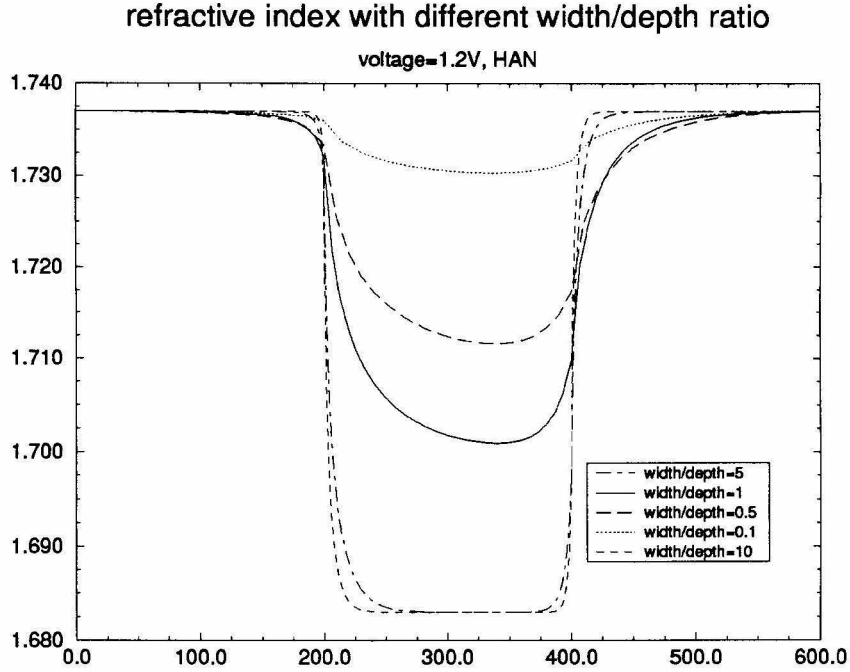


Figure 3.18: Fringe field effect modeling result of refractive index at different depth/width ratios with 1.2V driving voltage.

with the application considered, we can always do some optimization/tradeoff here.

3.5.2 Hologram recording with the LCOS deflector

Multiple holograms have been successfully recorded using the developed LCOS deflector as the angle addressing device in a 90° geometry angle multiplexing holographic recording system. The experimental setup is shown in Figure 3.19. Polarizing beam splitter (PBS) divides the collimated laser beam into two beams, where the signal beam is the passing beam whose polarization is converted into the same polarization as the reference beam by a half-wave plate. The reference beam is the reflecting beam from PBS and incident onto the LCOS deflector. A telescope system is setup to enlarge the reference beam spot for obtaining larger interfering area within the crystal. With different images imprinted into the SLM corresponding to different addressing angles from LCOS deflector, multiple holograms (interference patterns

between signal beam and reference beam) could be recorded inside the crystal. The recorded holograms can be readout by blocking the signal beam path and addressing corresponding angles to output the image onto the detector through an imaging lens located behind the crystal. In the setup, iris 1 is used to define the illumination beam area for the LCOS deflector to reduce the scattering from the substrate and iris 2 is used to block those higher diffraction orders from the LCOS deflector's high frequency grating. Seven holograms have been successfully recorded with the LCOS

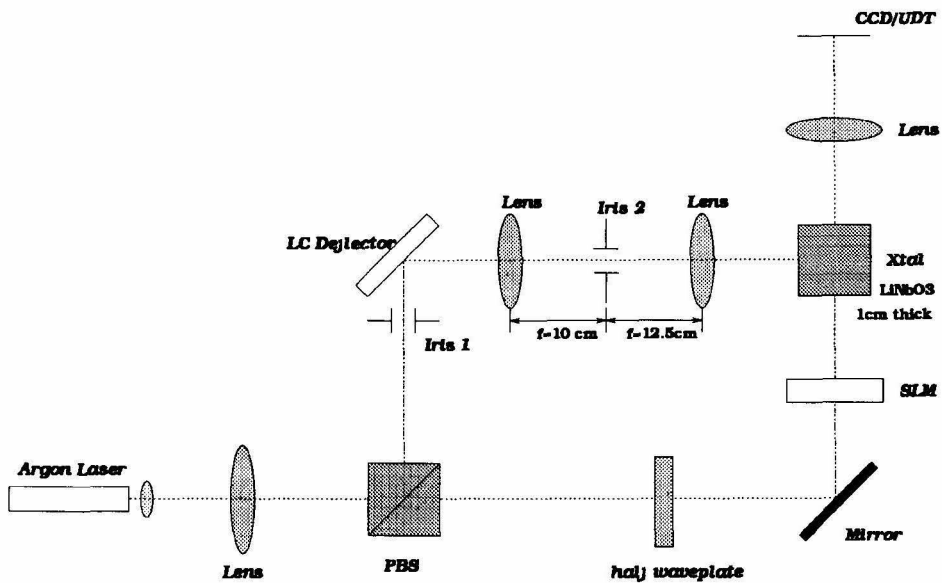


Figure 3.19: Experimental setup for multiple holograms recording with LCOS deflector.

deflector and there is no visible cross-talk observed. The readout of those holograms is shown in Figure 3.20.

The above experimental results show the LCOS deflector's great potential application in the holographic volume memory. However, there are still a couple of limiting factors: (1) Low diffraction efficiency due to the scattering from multiple layers of the structure as well as liquid crystal's absorption. This could be improved by coating the surfacing as well as adding some doping into the liquid crystal. (2) Limited number of addressable angles. This could be improved by novel designs which are

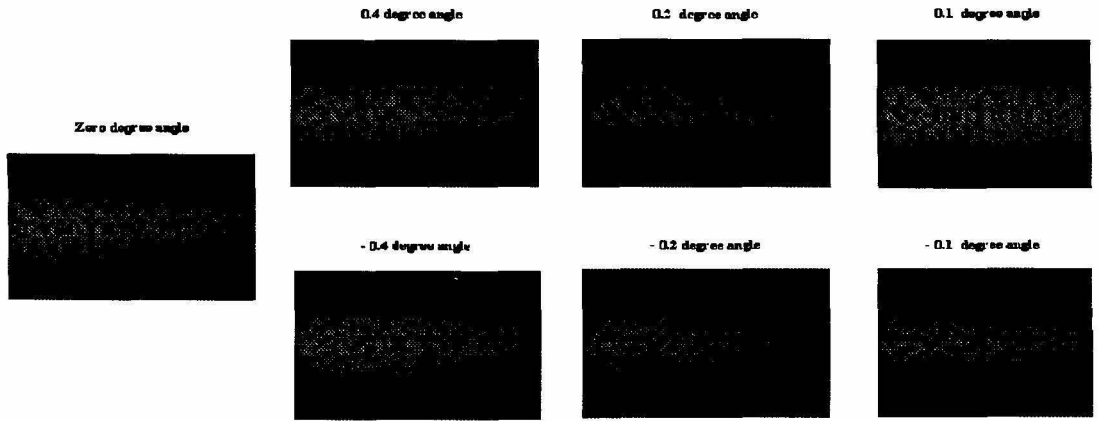


Figure 3.20: Multiple holograms recording and readout with LCOS deflector.

discussed in the next section. (3) Possible slow response time for future holographic system. Currently the demonstrated response time is good enough for most holographic recording systems since current systems' operation speeds are being limited by some other components in the systems, such as SLM and detecting speed, etc.

3.5.3 Programmable deflector design

A virtual blazed grating period programmable LCOS beam deflector with much more powerful angle-addressing capability (estimated about 97 angles) is designed to explore the feasibility of using this LCOS deflector into the final compact memory module. Due to the time constraint, the device is not characterized yet. Here we introduce the basic idea of the design for future developers' reference.

As we noticed, one limitation of the previously described LCOS deflector is the limited number of addressable angles. In order to comfortably use this device in a holographic memory system, a large number of addressable angles, say 100 angles, is commonly desired. One straightforward solution is to use a bigger chip to accommodate more controlling electrodes within the die. However, the resulting prohibitively high manufacturing cost obsoletes this approach quickly. One more clever way to

achieve this goal is to design a grating period programmable deflector.

Figure 3.21 illustrates the design idea. It is basically a 1-D analog scanner. The metal-electrodes are the liquid crystal driving medium in substrate chip. The corresponding driving voltage assigned to each electrode is sequentially reading in from the Voltage-in node by a passgate, where these voltages at the Voltage-in node are generated from off-chip circuitry. The passgate switches are controlled by the shift-registers (SRs). The shift registers shift in the direction of left to right. A new bit is loaded into the start of the shift registers at the end of a scan by means of the wired NAND, which computes the OR of low bits in the shift register. The pulldown (PD) transistor is usually made weak for biasing purpose only. The blocks at the bottom of this figure represents a digital shift-register that controls the scanning process. With each clock cycle, whatever bit is in a given stage is shifted to the next stage. Whatever bit is in the last stage in the line gets shifted out and disappears forever. Typically, there will be a single register that holds a high bit, and all the other registers will hold a low bit. That one register with high bit determines which passgate is on in that clock cycle for assigning the voltage-in into the metal-electrode. The line coming into the bottom of each SR is the global single-phase clock input. The wired NAND circuit logically NANDs together all the SR high so that a new high bit is generated when only low bits are left in the register. This arrangement is self-initializing and requires no off-chip control. With the very limited spacing between each electrode, we did not put the capacitor for each electrode for storing the assigned liquid crystal driving voltage. This could result in a voltage decaying at each electrode, which makes it very hard to fine tune the optimal driving voltage. However, as long as we can scan fast the electrode addressing clock as well as the shift register's timing clock, which is commonly true, this voltage decaying problem is negligible.

Figure 3.22 is the designed programmable LCOS deflector's VLSI chip layout. The whole chip area is 6.8mmx4.6mm, where the layout area is about 6.1 mmx4mm, designed with 1.2 μ m AMI 2 metal 2 poly nwell process. During the chip layout, in order to squeeze the multiple-transistor addressing circuits (shift registers) within each electrode size (only a few microns wide), each of the eight shift registers are

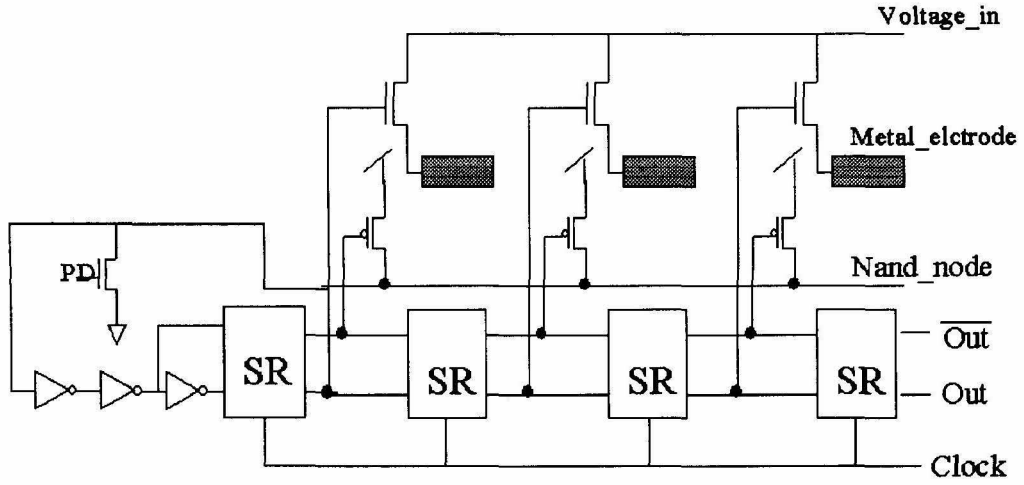


Figure 3.21: Programmable LCOS beam deflector addressing circuitry.

narrowed down to be one group and the connection lines are made with up and down loops to save area. The middle part of the chip is 384 electrodes that could be addressed sequentially by the scanning timing clock. By design, each electrode is $4\mu\text{m}$ wide with $8\mu\text{m}$ center to center space. The minimum number of electrodes for each subgroup is chosen as 8. The maximum subgroup consists of 384 electrode. Then for each side of the virtual blazed grating, we can address $384/8=48$ angles. As explained before, by taking into account the nonpolarity response of nematic liquid crystal, the total addressable angles will be $2 \times 48 + 1 = 97$, which is a quite impressive number. Assume 633nm wavelength, the field of view of this deflector would be 0.567° with the resolution of 0.0118° .

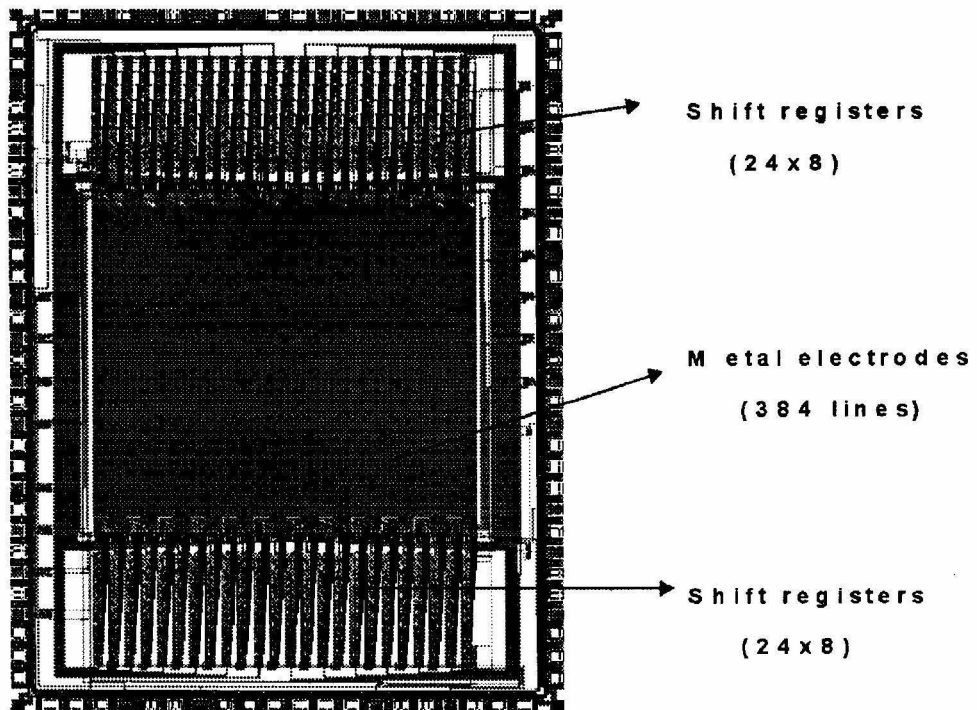


Figure 3.22: Programmable LCOS beam deflector chip layout.

Chapter 4 Liquid crystal blazed grating beam steering device

A transmission type non-mechanical multiple-angle beam steering device using liquid crystal blazed gratings has been developed. Sixteen steering angles with a contrast ratio of 18 has been demonstrated. A detailed analysis of the LC/PMMA blazed grating deflector was carried out to provide guidance during the deflector's development. Although the developed device's target application is for a compact holographic memory system, it is also a good candidate for many other applications, such as fiber communications [13], liquid crystal on silicon microdisplay [24], and optical scanners [25].

The device's working principles and design considerations are described first, and then the fabrication process is introduced. Finally, we present the characterization results and some discussion.

4.1 Introduction

Figure 4.1 is a cross section view of one layer of the liquid crystal beam deflector. The device's substrate is a polymethyl-methacrylate (PMMA) blazed grating made by direct E-beam lithography [26] on top of a transparent metal Indium-Tin-Oxide (ITO) coated glass. A transparent cover glass (also ITO-coated) is put on top of this PMMA blazed grating, separated with fiber spacers of a few microns. A thin layer of nematic liquid crystal is then sandwiched in between. The ITO layer deposited underneath the PMMA grating and another ITO layer coated on the bottom surface of cover plate are used to electrically drive the liquid crystal to change the phase information of the illuminating light. The essential idea to operate this LC/PMMA composite grating is to exploit the electro-optic effect of nematic liquid crystal, [3] where its refractive

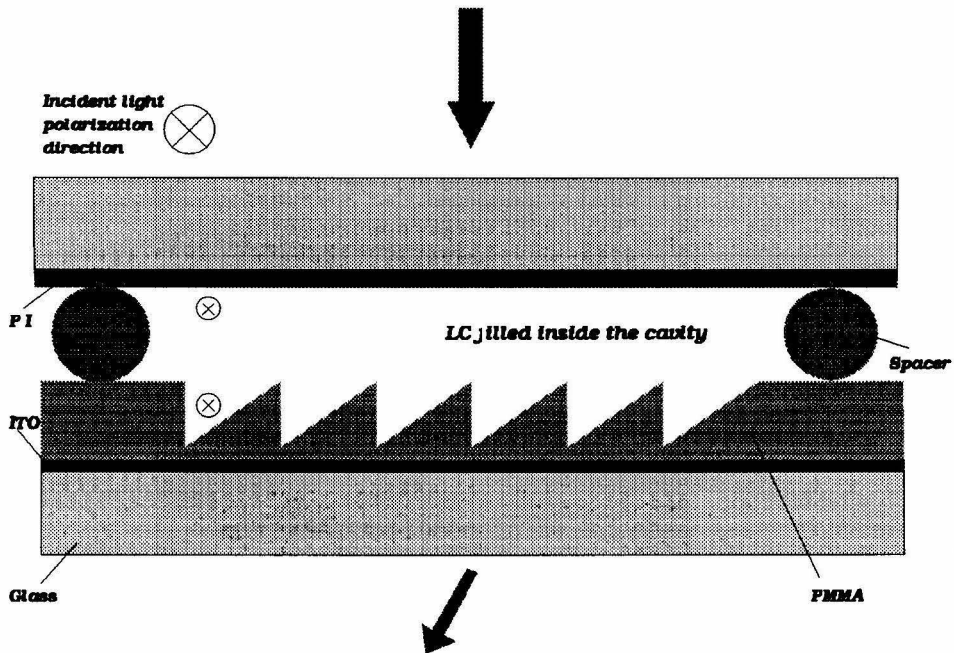


Figure 4.1: Liquid crystal blazed grating beam deflector.

index for extraordinary light can be modulated by the driving voltage. When no electric field is presented, the refractive indices of the PMMA substrate and liquid crystal are different, and strong diffraction is produced by the refractive index/phase difference of this “OFF” state. The diffraction efficiency is determined by the blazed grating parameters, such as grating depth, grating period, as well as blaze profile. When an electric field is applied, the refractive index of the liquid crystal is decreased and at a certain driving voltage, “index matching” occurs between the PMMA and the liquid crystal. The whole LC/PMMA composite grating structure can then be considered as an optically flat plate, and no diffraction occurs in this “ON” state. In such a way, the device can be viewed as an electrically controlled binary switch. The incident beam can be either deflected (the “OFF” state) or un-deflected (the “ON” state). Furthermore, this device belongs to the so-called polarized beam deflector since the above-described electro-optic mechanism only works for extraordinary light. Because of that, we have to make sure the incident light’s polarization direction is

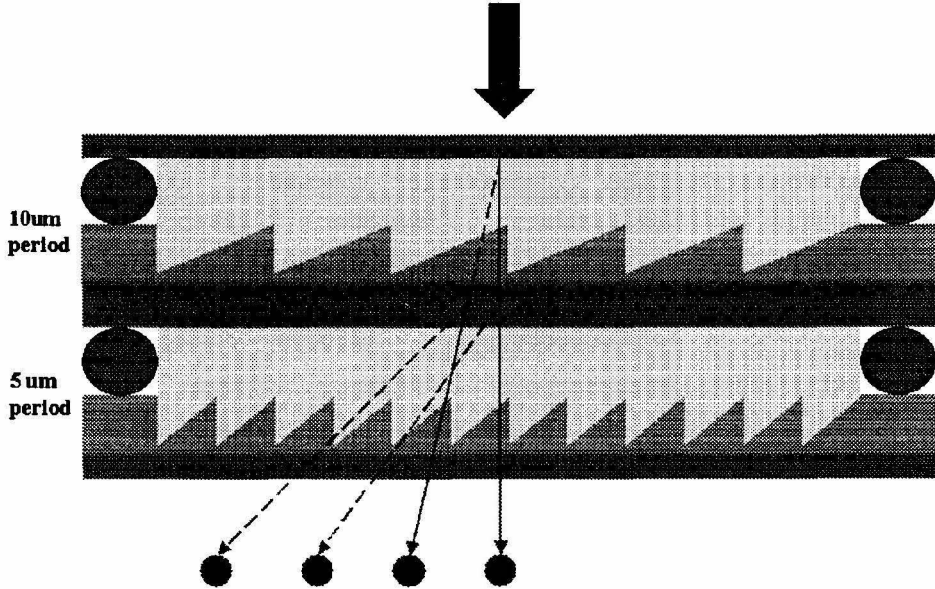


Figure 4.2: Multiple layer stacking concept to achieve multiple deflection angles.

the same as the liquid crystal extra-ordinary light direction (optical axis direction), which is the rubbing direction for homogeneous alignment configuration (see Chapter 2).

In order to obtain multiple angles, we stack several layers of this PMMA/LC composite blazed grating with different grating periods as in Figure 4.2. During the stacking, the top grating's period is made to be twice the period of the bottom grating to make all steering angles clearly resolvable. By applying different driving conditions on each layer, multiple steering angles are easily achieved. Obviously, the available number of steering angles is 2^N , where N is the number of stacked layers, i.e., in Figure 4.2, the output can be one of four different outputs depending on the driving condition combinations. The motivation here is to implement this kind of device with 1024 addressable angles by stacking 10 layers. However, the feasibility of this approach is strictly limited by each layer's diffraction efficiency. Currently, we have demonstrated 16 dynamically addressable angles by stacking 4 layers with a negligible cross-talk. It is expected that, with the same cross-talk, more stacking layers (corresponding to more addressing angles) could be easily implemented

provided that better diffraction efficiency could be achieved in each layer. The possible approach to improve each layer's diffraction efficiency is to either make better samples, especially better blazed grating profiles, or to use new liquid crystal materials that could offer larger Δn and smaller n_0 than n_{PMMA} so that we can better match the refractive indices of PMMA and liquid crystal with relatively small driving voltages.

4.2 Design considerations

4.2.1 Diffraction analysis

To understand the behavior of this device, a detailed analysis of the blazed grating diffraction is quite necessary. Considering that the device has a fairly large feature size relative to the illumination wavelength, scalar diffraction theory is used for its simplicity and fast-modeling time. As illustrated in Figure 4.3, the whole aperture

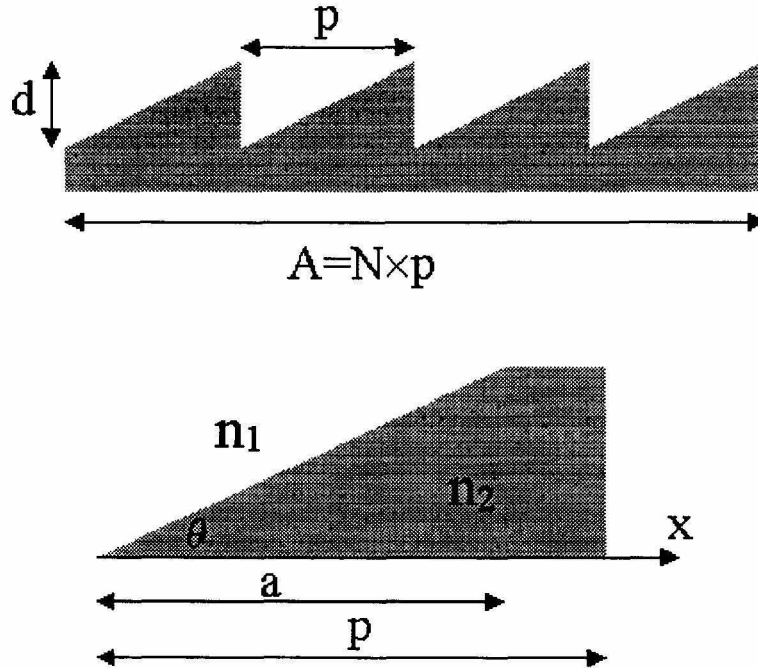


Figure 4.3: Liquid crystal blazed grating diffraction model.

transmittance $T(x)$ of the blazed grating is considered as a prism function $P(x)$ convolved with a periodic grating function $G(x)$:

$$T(x) = P(x) * G(x) \quad (4.1)$$

The periodic grating function is

$$G(x) = \sum_{m=1}^N \delta(x - mp) \text{rect}\left(\frac{x}{A}\right) \quad (4.2)$$

where p is the blazed grating period, and A is the illumination width. For the prism function $P(x)$, the fabrication error shown in Figure 4.3 is also taken into account in this analysis as follows:

$$P(x) = \text{rect}\left(\frac{x}{p}\right) e^{i\Delta(x)} \quad (4.3)$$

where $\Delta(x)$ is defined as

$$\begin{aligned} \Delta(x) &= \frac{2\pi}{\lambda} (n_1 - n_2) x \tan \theta & (0 < x \leq a) \\ \Delta(x) &= \frac{2\pi}{\lambda} (n_1 - n_2) d & (a < x < p) \end{aligned} \quad (4.4)$$

where the duty cycle is defined as a/p . Then the far field is the Fourier transform of this aperture transmittance,

$$E(x) = F.T.\{T(x)\} = F.T.\{P(x)\} \bullet F.T.\{G(x)\} = P \bullet G \quad (4.5)$$

Obviously, P results in a $\text{sinc}(x) = \frac{\sin(\pi x)}{\pi x}$ function profile in the far field and its peak location is defined by the prism depth d . G defines the diffraction order locations and samples the prism-produced $\text{sinc}(x)$ function to define the final diffraction pattern. If the blazed grating is well designed so that the prism-produced $\text{sinc}(x)$ function profile peaks at 1st diffraction order position, then theoretically the 1st order will have 100% diffraction efficiency and all other diffraction orders will have zero diffraction

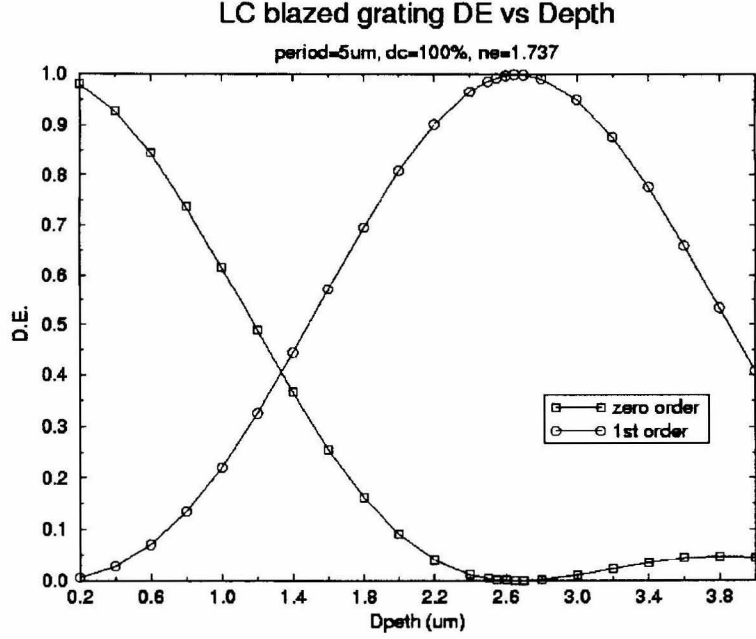


Figure 4.4: Optimization of the blazed grating depth.

efficiency. This also suggests that, even for one layer of LC/PMMA grating, it is possible to get multiple deflecting angles if the PMMA blazed grating depth is large enough so that the phase difference between PMMA and liquid crystal could reach the multiple integer numbers of 2π , say 4π , or 6π , which are corresponding to 2nd or 3rd diffraction order blazed respectively. However, for those cases, the switching speeds would be very slow due to the liquid crystal's large thickness since the response time of the liquid crystal device is proportional to the square of its thickness, i.e., a 2nd order blazed deflector's switching speed is 4 times slower than that of a 1st order blazed deflector.

For our LC/PMMA blazed grating, the illumination wavelength is 633nm, the refractive index of PMMA is taken as 1.49, and the refractive index of extraordinary light for liquid crystal E7 is taken as 1.737. With the ideal profile (100% duty cycle), the blazed grating's optimal depth is calculated to be $2.67\mu\text{m}$ as shown in Figure 4.4. We fabricated four PMMA samples with the grating periods of $5\mu\text{m}$, $10\mu\text{m}$, $20\mu\text{m}$

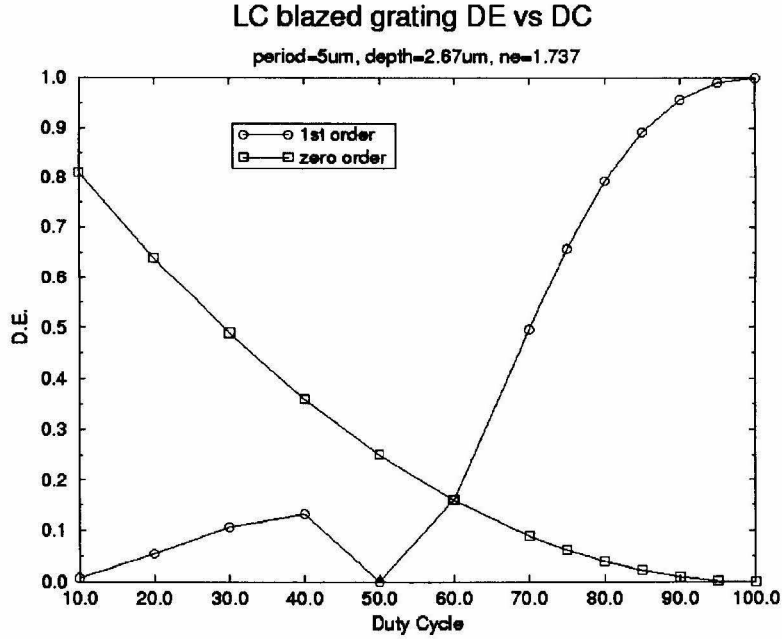


Figure 4.5: Influence of blazed grating duty cycle on diffraction efficiency.

and 40 μ m. From scalar diffraction theory, this optimal depth is the same for all grating periods. Using this optimal depth, the diffraction efficiency is calculated as a function of duty cycle in Figure 4.5. It clearly shows that the non-optimal duty cycle degrades the performance significantly. Also, 50% duty cycle blazed grating has zero diffraction efficiency into the 1st diffraction order, which also validates our numerical modeling's correctness to some degree.

We also verify our program's validity by using DIFFRACT [27], a software package based on full vector coupled-wave theory and developed by Massachusetts Institute of Technology Lincoln Laboratory. The program can model linear (periodic in 1-D) or crossed (periodic in 2-D) surface-relief diffraction grating. The program takes indices to be complex for both dielectrics and metals. Thin film, a "coatings", and multiple thin layers are also allowed. This feature offers us a way to include coverglass, polyimide, and ITO layers of the device into the calculation, which is more closer to the real structure. The simulation result from the program is illustrated in Figure 4.6.

LC Blazed Grating Deflector Design Goal

(E7 LC, wavelength=0.6328 μ m)

10 μ m period, depth=2.67 μ m, dc=100%

5 μ m period, depth=2.67 μ m, dc=100%

D.E. Order	ON	OFF
1	0.48%	0.29%
0	94.06%	0.28%
-1	0.68%	84.32%
-2	0.15%	0.12%

D.E. Order	ON	OFF
1	0.48%	0.35%
0	94.21%	0.47%
-1	0.67%	83.06%
-2	0.16%	0.27%

10 μ m & 5 μ m sample stacking together

Voltage source	Steering angle	Design D.E. goal
Both OFF	10.8 degree	83.06% x 84.32% \longrightarrow 70.4%
10 μ m ON 5 μ m OFF	7.2 degree	83.06% x 94.06% \longrightarrow 78.1%
10 μ m OFF 5 μ m ON	3.6 degree	94.21% x 84.32% \longrightarrow 79.4%
Both ON	0 degree	94.21% x 94.06% \longrightarrow 88.6%

Figure 4.6: Simulation result from DIFFRACT program.

Those results are quite agreeable with our scalar theory calculation. Considering that the much longer calculation time for DIFFRACT, we will use the scalar theory analysis afterwards.

4.2.2 Driving voltage loss and non-uniformity

Numerical simulation results from Chapter 2 are used here for our device development. Specifically, the homogeneous aligned nematic configuration is chosen for our deflector since this configuration features a larger index modulation than other configurations. This lowers our blazed grating's depth requirement for reaching the 2π phase delay corresponding to the 1st diffraction order. This smaller depth requirement also offers us a quicker switching time.

For our device, the driving voltage is applied between two ITO layers. However,

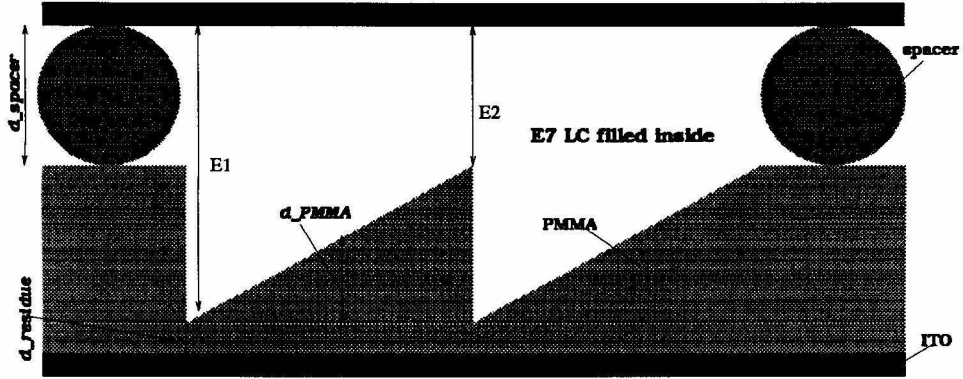


Figure 4.7: Illustration of liquid crystal blazed grating deflector's driving voltage loss and non-uniformity.

the PMMA blazed grating is made on top of the substrate's ITO layer to simplify the fabrication process. This obviously will reduce the driving voltage on the liquid crystal since PMMA is a poor conductor. (The conductivity is reported to be about 10^{-11} S/m in the glassy state at room temperature with dielectric constant of about 3 [6].) Also, the PMMA blazed grating profile results in different driving voltages on the liquid crystal at different locations. Figure 4.7 illustrates the above mentioned driving voltage loss issue and voltage non-uniformity issue.

The driving voltage loss calculation can be determined from Maxwell equation's boundary condition on electric field:

$$\vec{D}_{LC_n} - \vec{D}_{PMMA_n} = \sigma = 0 \quad (4.6)$$

where \vec{D} is the electric displacement and σ is the surface charge density, which is zero in our analysis. Based on the dielectric constants of E7 liquid crystal and PMMA, and considering that there is a residual PMMA layer at the bottom of the LC/PMMA grating, the effective voltage, V_{eff} , on the LC/PMMA grating can be obtained from the following equation:

$$V_{eff} = \frac{1-r}{1+5r} V_{apply} \quad (4.7)$$

where V_{apply} is the applied voltage on those two ITO layers and r is the ratio of the residual PMMA layer thickness and the depth summation of spacer and PMMA grating. From this we can define the actual driving voltage on the liquid crystal V_{LC} at different positions:

$$V_{LC}(x) = \frac{1 - rr(x)}{1 + 5rr(x)} V_{eff} \quad (4.8)$$

where $rr(x)$ is the depth ratio between the PMMA grating and spacer at different locations. From calculations, only 18% to 60% of the driving voltage is actually applied on the liquid crystal with the parameters of $5\mu\text{m}$ spacer, 0.6mm residual uniform a PMMA layer, and PMMA grating depth of $2.67\mu\text{m}$ assuming a 100% duty cycle.

The phase delay caused by the LC/PMMA composite structure at different locations within one period was calculated at different applied voltages. Figure 4.8 shows that, although the voltage on the liquid crystal is different at different positions, the phase delays at those positions actually become more uniform at higher voltage. The reason is that, at locations with thinner PMMA, the driving voltage loss is less, which results in a smaller liquid crystal refractive index. At locations with thicker PMMA, the voltage loss is greater so that the refractive index of the liquid crystal is remaining relatively large, which compensates the low index of PMMA to reach the roughly same phase delay as those thinner PMMA parts. This analysis improves our understanding of device's working principles in the "ON" state. Normally, it is difficult to reach index matching between liquid crystal and PMMA at every location due to the applied voltage's non-uniform distribution. However, we can reach uniform phase distribution at every location at a higher voltage, which ensures the device's successful operation. In that sense, it is more meaningful to discuss the phase matching rather than the index matching.

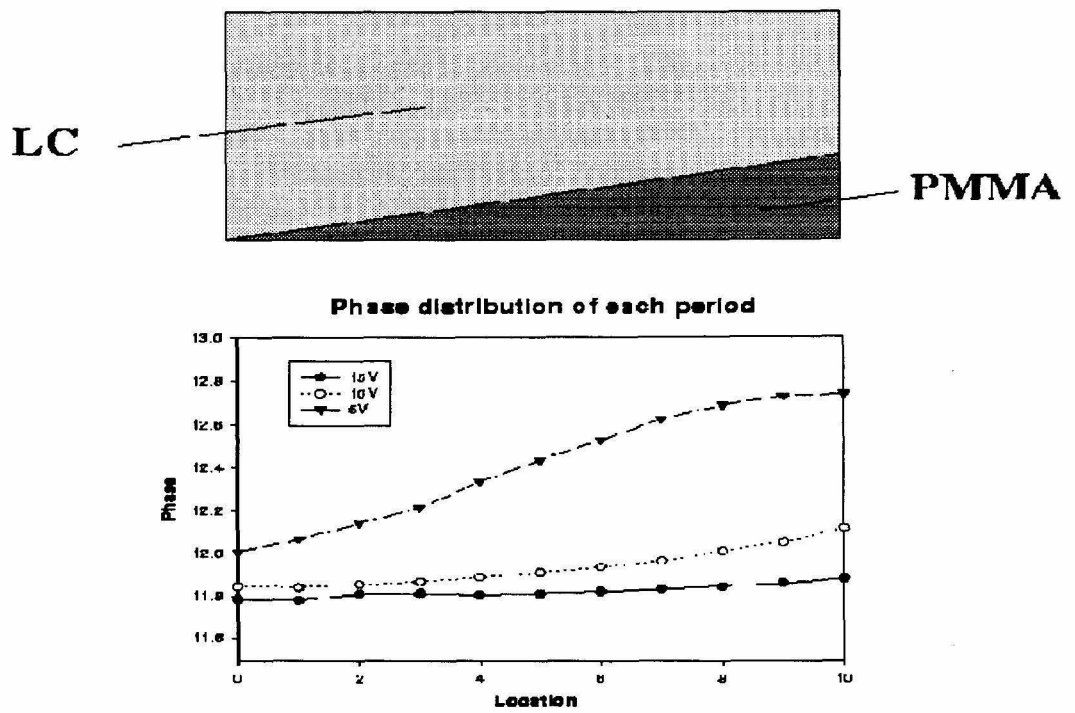


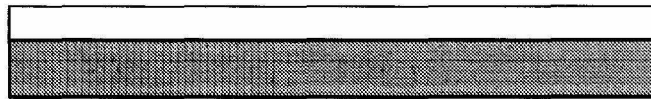
Figure 4.8: Liquid crystal blazed grating deflector's index matching.

4.3 Fabrication process

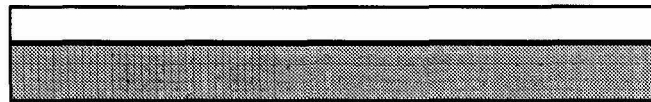
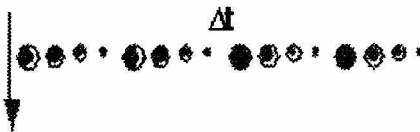
The PMMA blazed gratings were fabricated by direct-write electron-beam lithography [26]. Figure 4.9 shows the basic flow chart of the process. The ITO-coated substrates were prepared by spinning in succession five layers of PMMA to achieve a total thickness of $3.3\text{ }\mu\text{m}$. Each deposition sequence included a bake-out for 60 minutes at 170°C . Prior to exposure, the sample was over-coated with 10nm of aluminum, which acted as a discharge layer preventing de-focusing due to surface charge buildup. The E-beam exposure patterns for the blazed grating were composed of square pixels ($0.5\text{ }\mu\text{m}$ for $5\text{ }\mu\text{m}$ period grating, $1\text{ }\mu\text{m}$ for $10\text{ }\mu\text{m}$ period grating, etc.). Within each pixel, the E-beam spot was rastered to uniformly expose the pixel area. The pixel doses were determined from the desired depths, taking into account the nonlinear depth versus dose response of the PMMA and the E-beam proximity effect (backscattered dose from the substrate). The proximity effect for these substrates (50 kV acceleration voltage) was measured to have a Gaussian $1/e$ radius of $10.75\text{ }\mu\text{m}$ and an integrated strength of 0.5 of the initial dose. Fourier transform deconvolution of the proximity effect function was performed on the pixelized dose profile as described in [28].

The gratings were exposed using a JEOL JBX-5DII E-beam lithography system at 50 kV with a beam current of 4 nA, which corresponds to a spot size of $0.3\text{ }\mu\text{m}$. This is larger than would be used for precision lithography, but it somewhat smoothes the surface of the blazed grating and reduces writing time. The total exposure time for each grating having an area $3.2\text{ mm} \times 3.2\text{ mm}$ area was 70 minutes. After exposure, the aluminum overcoat was removed and the grating was developed in pure acetone using a Solitec spinner equipped with an electronically controlled Tridak resist dispenser. The substrate was spun at 1000 RPM while the acetone was squirted down at the center of rotation. At the end of 8 seconds, the acetone was abruptly cut off and replaced by a blast of dry nitrogen. This quenched the development and at the same time dried the surface of the PMMA. Additional development steps with times as short as 0.5 seconds were used to achieve the desired grating depth. The

Thin film of PMMA on ITO-coated glass



50 keV
electrons



After acetone development

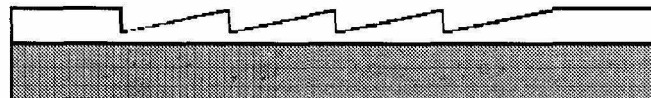


Figure 4.9: PMMA blazed grating fabrication process flow chart.

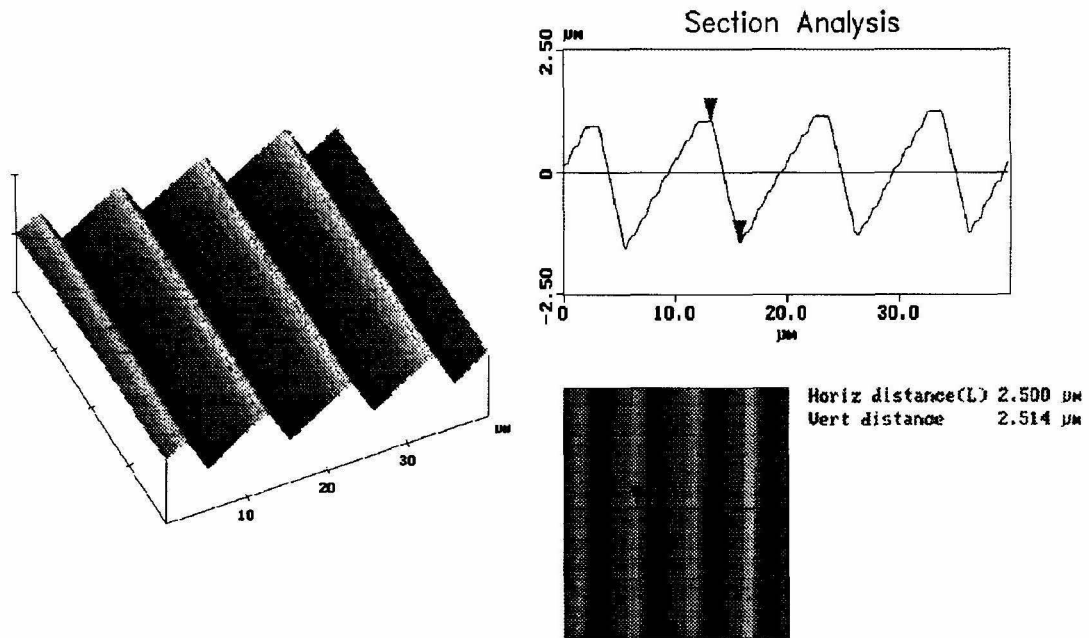


Figure 4.10: Surface profile of 10 μm period grating measured by AFM.

depth was gauged by measuring the diffraction from a computer-generated hologram (on the same substrate) that was designed to produce a null zero order. Near the final depth, the grating profile was measured directly using a Digital Instruments Nanoscope III atomic force microscope. Figure 4.10 shows the final surface profile of the 10 micron period grating. As we can see, the blazed slope is quite good although the top plane has small portion of flatness, which induced a non-100% duty cycle. Nevertheless, the 40 μm sample's duty cycle is much better. More contour surface parameter verifications will be discussed in the next section.

The final device package process is based on the liquid crystal cell with homogeneous alignment packaging process described before (see Chapter 2) with the following exceptions: (1) PMMA grating sample is not rubbed. The reason is that the E-beam fabricated blazed grating surface has tiny grooves along the blazed slope (see Figure 4.10) that can be utilized as the natural alignment layer if we fill the liquid crystal along the groove direction. However, it is very important that the

LC Blazed Grating Deflector Fabrication Process Diagram

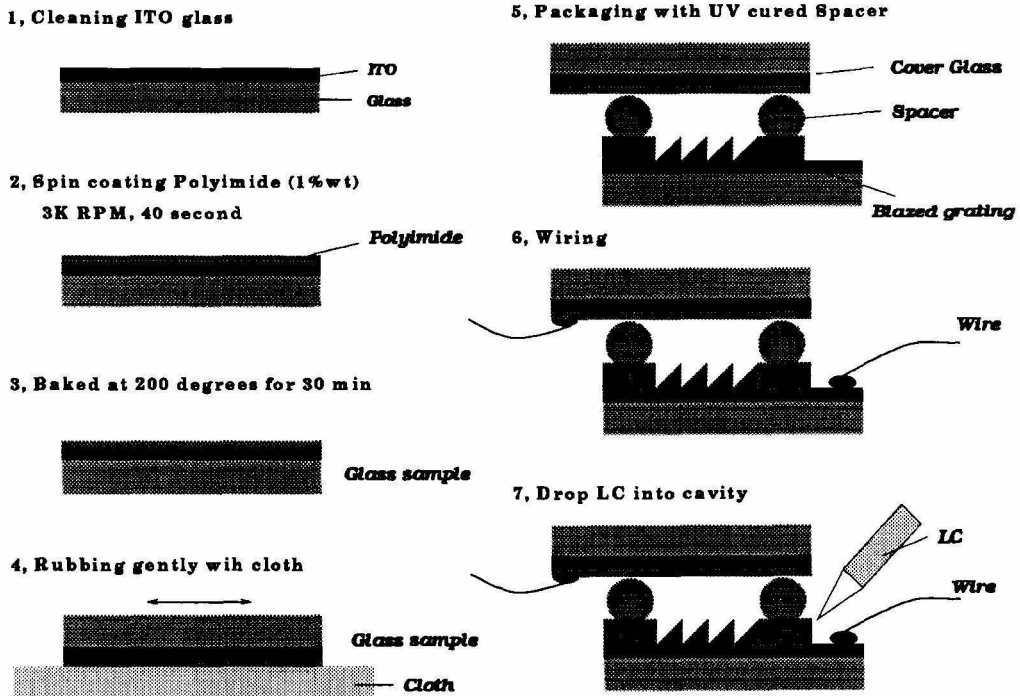


Figure 4.11: Liquid crystal blazed grating deflector packaging process.

cover plate's alignment direction be parallel to the grating groove direction to reach the homogeneous alignment configuration. (2) The filling process has to be finished in room temperature since the PMMA can't sustain high temperature due to its $\sim 110^{\circ}\text{C}$ melting point. The whole packaging procedure is illustrated in Figure 4.11.

The following are some considerations for stacking multiple layers of this liquid crystal/PMMA composite grating. First, in order to make full use of each layer's manufacturing-limited effective area, an accurate alignment of those samples is necessary. This can be achieved by continuous adjustment monitored by a microscope. Second, the extraordinary axis directions of each layer must be aligned during stacking since the device is operated in polarization mode. Third, each layer's deflection direction should be the same so that each layer's deflection could be monotonically accumulated. Finally, in order to reduce scattering, the best stacking order for illu-

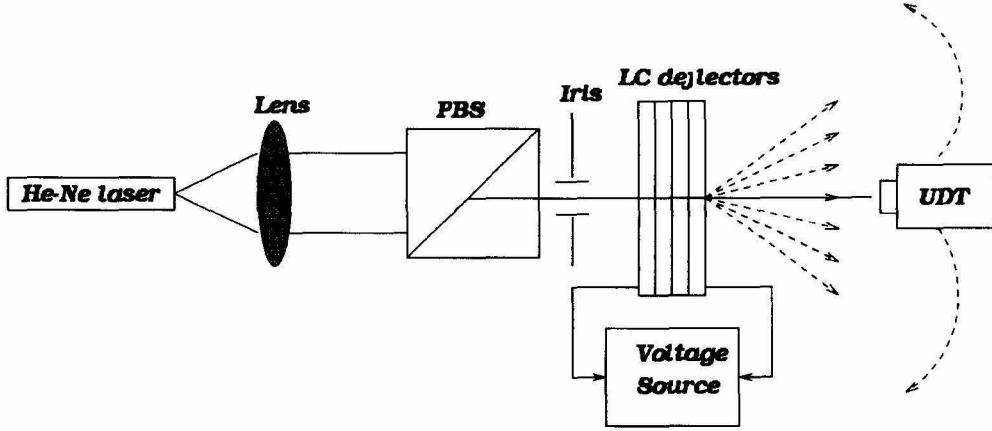


Figure 4.12: Device's characterization experimental setup.

mination is $40\mu\text{m}$, $20\mu\text{m}$, $10\mu\text{m}$ and $5\mu\text{m}$. Illuminating the $40\mu\text{m}$ grating layer first will generate the smallest deflection angle (approximately 0.9°) so that for subsequent layers, the incident angle can still be considered as approximately normal.

4.4 Experiment and discussion

The experimental setup is shown in Figure 4.12. A polarized beam is incident on the deflector with its polarization direction parallel to the liquid crystal alignment direction since it is a polarized beam deflector. Four individually controllable DC-balanced 1KHz square waveforms are applied onto four stacked liquid crystal blazed gratings respectively. A detector mounted on a scanning translation stage measures the far field intensity at each diffraction order to calculate the diffraction efficiency.

4.4.1 Define sample profile parameters

Before stacking the LC/PMMA layers, we need to accurately determine the PMMA blazed grating profiles' parameters. The parameters are determined by combining three measurements. The first step is to use the AFM profile measurement data as

shown in Figure 4.10. However, due to the finite size of the AFM tip and the sharp transition corners of the blazed grating, the AFM tip does not typically probe the deepest region of the grating surface, so the depth measurement is not quite reliable. Nevertheless, it does at least accurately give us the duty cycle information, which is used for the next two steps. The second step is to compare the experimental measurement and theoretical prediction of the diffraction from the PMMA blazed grating in free space (no liquid crystal). The third step is implemented after filling liquid crystal into the PMMA blazed grating. This is to compare the experimental measurement and theoretical prediction of the diffraction from the LC/PMMA composite grating without any applied voltage. Figure 4.13 shows an example of defining contour parameters with the $10\mu\text{m}$ sample. The optimal parameters, given by the best match between experimental data and the model prediction of the diffraction orders, are $2.74\mu\text{m}$ depth and 82% duty cycle for the sample. Similarly, the other sample profiles' parameters are finalized as follows: $5\mu\text{m}$ sample is $2.85\mu\text{m}$ deep with 90% duty cycle, $10\mu\text{m}$ sample is $2.74\mu\text{m}$ deep with 82% duty cycle, $20\mu\text{m}$ sample is $2.71\mu\text{m}$ deep with 94% duty cycle, and $40\mu\text{m}$ sample is $2.87\mu\text{m}$ deep with 99% duty cycle.

4.4.2 Single layer deflector characterization

During this characterization, we measured the intensity variations while scanning the driving voltage from zero to 8V for each liquid crystal blazed grating. The experimental data for the $10\mu\text{m}$ sample is plotted in Figure 4.14. Note that the diffraction efficiency at a small voltage (1.5V) is actually higher than that at zero voltage for the OFF state. The reason is that, suggested from the profile parameters definition, the fabricated PMMA samples's depth is slightly higher than the optimal design depth. As discussed previously in the scalar diffraction analysis, the micro-prism produces a $\text{sinc}(x)$ function which could shift the blaze location to different diffraction orders, corresponding to different prism depths reaching a 2π phase delay. The phase delay

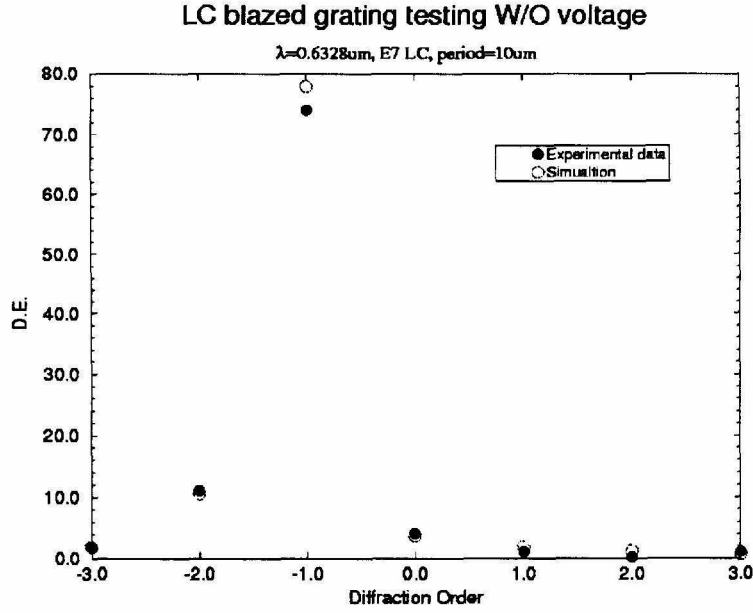


Figure 4.13: Determination of grating surface profile parameters.

difference $\Delta\phi$ between liquid crystal and PMMA is:

$$\Delta\phi = \frac{2\pi}{\lambda} \Delta n d \quad (4.9)$$

where Δn is the refractive index difference between PMMA and liquid crystal, and λ is the illumination wavelength. If the depth d is slightly larger than the optimal one, $\Delta\phi$ is larger than expected so that the peak will be shifted slightly to the right side of the desired position. We can shift this $\text{sinc}(x)$ function peak back to the desired location by reducing Δn and hence reaching the optimal $\Delta\phi$. This trick is based on the fact that liquid crystal's refractive index can be modulated by applying a driving voltage. We call this small voltage as “virtual” OFF voltage of the liquid crystal deflector.

The above discussion also gives us a hint for the device fabrication. Actually what we should really care about during PMMA blazed grating sample fabrication is the grating shape rather than the strict control of grating depth. As long as its depth

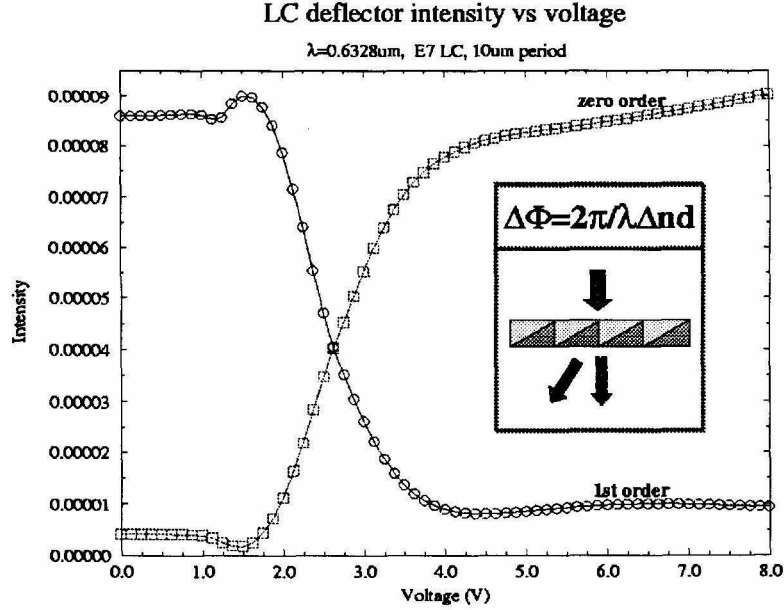


Figure 4.14: Liquid crystal blazed grating diffraction intensity vs driving voltage.

is larger than the optimal design goal, the fabrication defect can always be compensated by using a “virtual” OFF voltage. This property eases sample fabrication since accurate control of the depth is somewhat painstaking. (Of course, the depth can not exceed the design goal too much since it might cause other problems for the beam steering; say, the PMMA depth is very large and the voltage loss is big so that a very large ON voltage will be needed to reach phase matching. Or, the depth is so large that the grating will be blazed at other higher orders, etc.)

Using this “virtual” OFF voltage trick, we first tested the four liquid crystal deflectors separately. The maximum applied voltage was 15V. Considering the voltage loss calculated before, the real voltage driving the liquid crystal is about 2.7V to 9V. All measurement data are listed in Figure 4.15. The measured diffraction efficiencies at ON and OFF state are all in the range of 81.7% to 93.6%. The cross-talk turns out to be very small. (The intensity ratios between the brightest spot and the second brightest spot are in the range of 32~60.)

4 PMMA/LC samples performance parameters

<div> period D, μm order </div>	5 μm		10 μm		20 μm		40 μm	
	ON	OFF	ON	OFF	ON	OFF	ON	OFF
2	1.4%	2.48%	0.71%	0.85%	0.37%	0.29%	0.73%	0.31%
1	2.3%	2.15%	2.47%	0.53%	1.11%	0.44%	2.41%	0.95%
0	87.65%	2.56%	88.62%	2.03%	93.62%	1.96%	88.99%	7.71%
-1	2.4%	81.68%	2.64%	82.90%	1.56%	87.50%	4.83%	83.42%
-2	1.34%	2.05%	0.57%	0.84%	0.45%	5.34%	1.22%	5.24%

Figure 4.15: Performance of the 4 LC/PMMA blazed gratings.

4.4.3 Multiple layer deflector characterization

After characterizing the single-layer deflectors' performance, we stacked the samples to demonstrate 4, 8, and finally 16 steering angles. Again, the virtual OFF voltage trick was applied. Figure 4.16 shows the big performance improvement achieved by this virtual OFF voltage trick. The diffraction efficiency with the virtual OFF voltage applied is at least 10% higher than that without applying voltage. Correspondingly, the contrast ratio is dramatically enhanced. The steering efficiencies of the 4 angles ranged from 67% to 75%. The contrast ratio between the strongest and second strongest spots is in the range of 15~21.

Finally, the measurement data for the 16 steering-angle stacked deflector are tabulated in Figure 4.17. Experimentally demonstrated steering efficiency ranges from 28.9% to 57.6% and the contrast ratio ranges from 9.1 to 17.7. Figure 4.18 shows pictures of the laser beam steering spots as well as the driving condition. The 16 steering angles (0-13.5°) are obtained with a resolution of 0.9°.

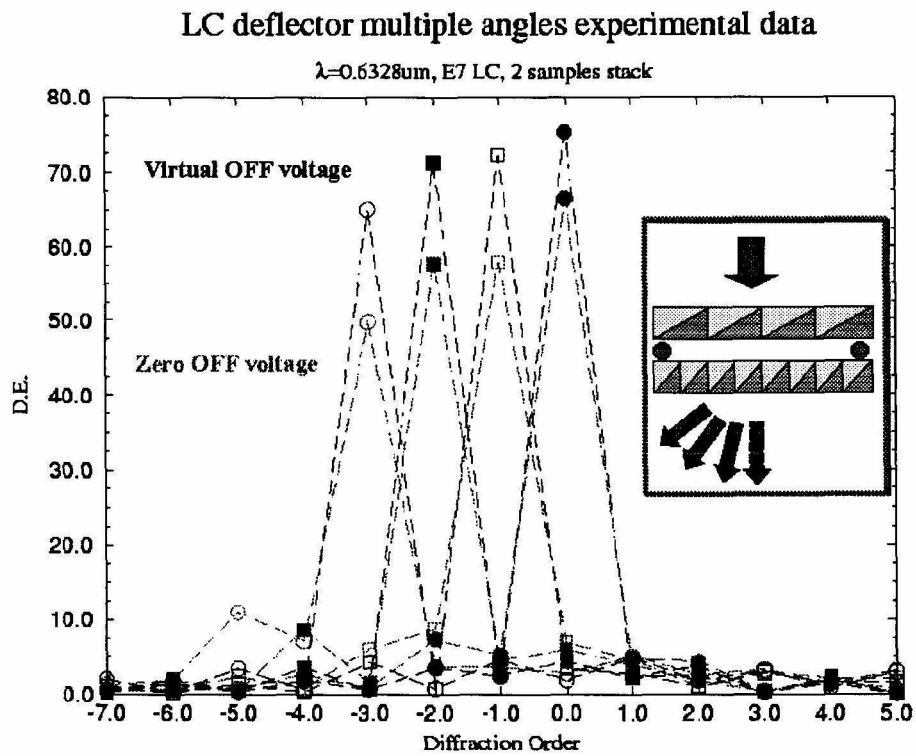


Figure 4.16: Comparison between real-OFF state and virtual-OFF state.

16 Angles Deflector Steering Testing Results

5 um	10um	20um	40um	Angle	D.E.	1st/2nd
1	1	1	1	0.0	0.5759	17.7
1	1	1	0	0.9	0.5661	17.5
1	1	0	1	1.8	0.5637	13.5
1	1	0	0	2.7	0.4400	10.2
1	0	1	1	3.6	0.5308	14.7
1	0	1	0	4.5	0.4024	12.6
1	0	0	1	5.4	0.5225	10.4
1	0	0	0	6.3	0.4125	11.9
0	1	1	1	7.2	0.4336	14.4
0	1	1	0	8.1	0.3627	12.7
0	1	0	1	9.0	0.4833	10.9
0	1	0	0	9.9	0.3734	9.8
0	0	1	1	10.8	0.4402	13.5
0	0	1	0	11.7	0.3410	9.9
0	0	0	1	12.6	0.4023	9.4
0	0	0	0	13.5	0.2892	9.1

Figure 4.17: Measurement data of the 4 stacked-grating 16-angle deflector.

















16 steering angles experimental results		
Angle (degree)		Condition
13.5		0 0 0 0
12.6		0 0 0 1
11.7		0 0 1 0
10.8		0 0 1 1
9.9		0 1 0 0
9.0		0 1 0 1
8.1		0 1 1 0
7.2		0 1 1 1
6.3		1 0 0 0
5.4		1 0 0 1
4.5		1 0 1 0
3.6		1 0 1 1
2.7		1 1 0 0
1.8		1 1 0 1
0.9		1 1 1 0
0.0		1 1 1 1

Figure 4.18: Photographs of the 16-angle deflector diffracted spots.

Chapter 5 Modeling and measuring of optical diffraction from sub-wavelength structures

Modeling of sub-wavelength features at focused spot has many applications, such as optical data storage [29], optical inspection, particularly in the semiconductor and storage industries [30, 31], digital optics [32], and metrology [33]. Currently several research groups are working on this issue. Marx et al. [34] developed a numerical modeling package based on the integral method for the diffraction of focused spot from subwavelength structure. Liu et al. [35] modeled a similar problem using finite difference frequency domain method. Yeh et al. [36] modeled the diffraction of focused beams by a multilayer-coated grating that emulates an optical disk. All those works report that there is an obvious difference in diffraction performance for differently polarized illumination beams when feature size is comparable to the wavelength.

A numerical modeling program capable of handling arbitrary 2-D features in a planar surface was developed. The original modeling motivation is to explore its application in pit-depth encoded memory, such as CD-ROM/DVD-ROM, given that the track pitch of current pregrooved optical disks is already of the order of one optical wavelength. The modeling problem, as shown in Figure 5.1, consists of a single or aperiodic subwavelength size substrate surface with a known contour and the illumination field is coming from a focusing lens with a known numerical aperture. Basically speaking, it is a two layer interface problem. For relatively large features, Fresnel's law solves the problem perfectly. However, for subwavelength structures, commonly used coupled-wave theory can not be applied since the structure is not periodic. The Integral method [37] is adopted for this problem. The essential idea is to generate surface current and solve the Maxwell equations directly with the claim that

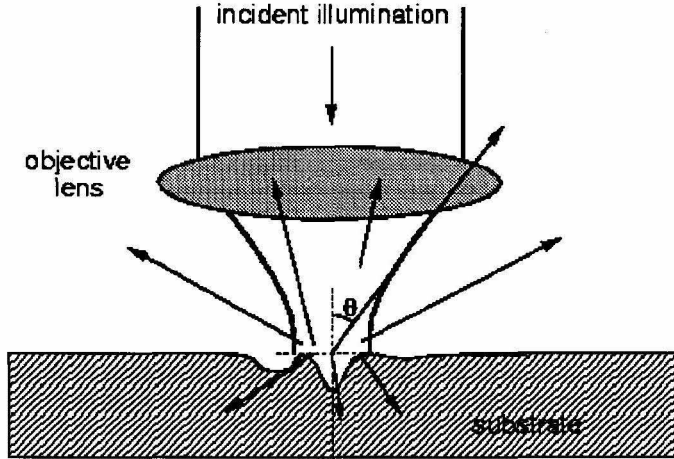


Figure 5.1: Diffraction modeling of focused spot from sub-wavelength structure.

electrical and magnetic field everywhere can be calculated from the tangential surface current in a source free domain. For the current work, we are more concentrating on the application of the program rather than the modeling itself since this has been described in great detail previously [38].

This chapter demonstrates two types of applications for our numerical modeling. One is the online inspection of semiconductor wafer, and the other is high capacity optical disc memory. Although these two applications seem quite different, the essential optical diffraction from sub-wavelength structure follows the same principle.

5.1 Introduction

We collaborated with IBM Almaden Research Center on the program's application in semiconductor wafer inspection. Specifically, we will analysis/measure/compare the scattering from isolated subwavelength features on smooth, flat substrates. For this application, a typical question is: Can we extract as much structural information as

quickly as possible? One straightforward way is to use an Atomic Force Microscope (AFM) to measure the surface profile. However, this generates two problems. First of all, the checking time (directly related to the cost issue) is a big concern. Secondly, although the resolution of AFM is quite impressive, the well-known artifact problem [39] is still troublesome. Although there are a lot of tricks [40, 41] proposed to improve this artifact problem, currently none is successful in the semiconductor industry due to the allowable limited off-line defect-checking time. Considering that, a more practical way seems to be online non-contact defect-checking. In other words, we can extract/compare the structure's information by measuring the surface scattering. Our software package is definitely a good starting point for this task.

In semiconductor wafer inspection, the main defects tend to be particles sitting on the surface and pits in the surface. Experimental work has concentrated on using monodisperse particles of known size to dust a surface [42]. [43] also reported the modeling and experimental work on surface characterization, which was basically trying to distinguish the polystyrene spheres and etch pits for periodic features. This has several experimental advantages: the defects are well characterized without having to characterize individual particles and the density of particles is generally set so that there are always several (identical) scatterers in the beam at any time, eliminating the need to search for a specific defect and increasing the signal strengths. Modeling of scattering from spheres or ellipsoids on a substrate also has the advantage of being more tractable than the case of a generalized scatterer [30].

We have chosen to look at single isolated features. For our experimental work, the features are made by a focused ion beam (FIB) process, which allows us to make features of different sizes and shapes down to the submicron range. The FIB process is very flexible in that it can etch features into a surface or deposit on a surface. It can also be used to simultaneously create fiducials which later help in locating the features for the scattering experiments. Modeling of this requires the ability to handle features with arbitrary cross sections rather than being specific to spheres or some other specific shape. The model used in this paper is restricted to two-dimensional features, but is applicable to arbitrary profiles.

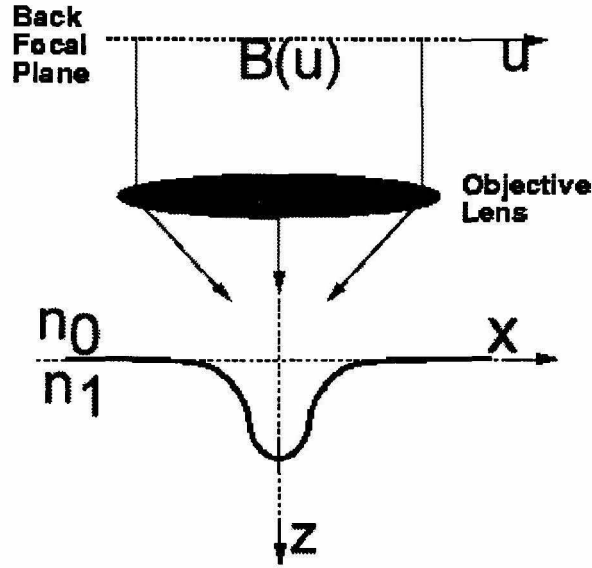


Figure 5.2: Incident field notation.

5.2 Diffraction modeling

For this particular application, the following are the modifications we made from previously developed program [38].

5.2.1 Incident beam

In previous modeling, for simplicity, the incident beam is defined as a truncated rectangular beam. Figure 5.2 shows the notation of incident beam definition. $B(u)$ represents the amplitude and phase distribution of the TE electrical field at front focal plane of the lens. The notation of TE/TM is defined as follows. The TE mode's electrical field direction is perpendicular to the incident beam plane (parallel to the groove direction), which corresponds to the conventional S polarization. The TM mode's electrical field lies in the incident plane, which corresponds to the conventional P polarization. The definition of $B(u)$ for rectangular shape incident beam is given

by:

$$B(u) = \begin{cases} 1 & |u| \leq NA \\ 0 & |u| > NA \end{cases} \quad (5.1)$$

where NA corresponds to the numerical aperture of the lens. Considering that a laser beam normally has a Gaussian distribution profile, a more accurate way to represent the incident beam is a Gaussian distribution. Here we define the optical beam intensity reduced to $1/e$ of its peak value at the NA boundary of the focusing lens. The final expression of the incident beam is:

$$B(u) = e^{\frac{-u^2}{NA^2}} \quad \text{for any } u \quad (5.2)$$

where u is the coordinate at front focal plane of the focusing lens. Figure 5.3 shows the far field diffraction comparison between rectangular shape and Gaussian shape incident beams for the same sample (profile2), where the spatial frequency $K = \frac{\sin \theta_s - \sin \theta_i}{\lambda}$, θ_s and θ_i are the scattering angle and incident angle respectively, and λ is the wavelength (633nm). For rectangular shape incident beam, the far field intensity distribution shows a strong overshooting at the focusing lens's NA boundary region, which is the well-known Gibbons phenomenon. Because of that, its predicted value at center point ($\theta_s = 0$) has some offset from its actual value. Comparing to that, the far field distribution from Gaussian shape incident beam has much better performance. It gives the correct center peak, and the whole scattering curve is much more smooth than its rectangular counterpart. Furthermore, the rectangular shape incident beam does not clearly show the scattering's dropping trend at every scattering angle (after a spatial frequency of 1.4), which is obviously present in the Gaussian shape incident beam case.

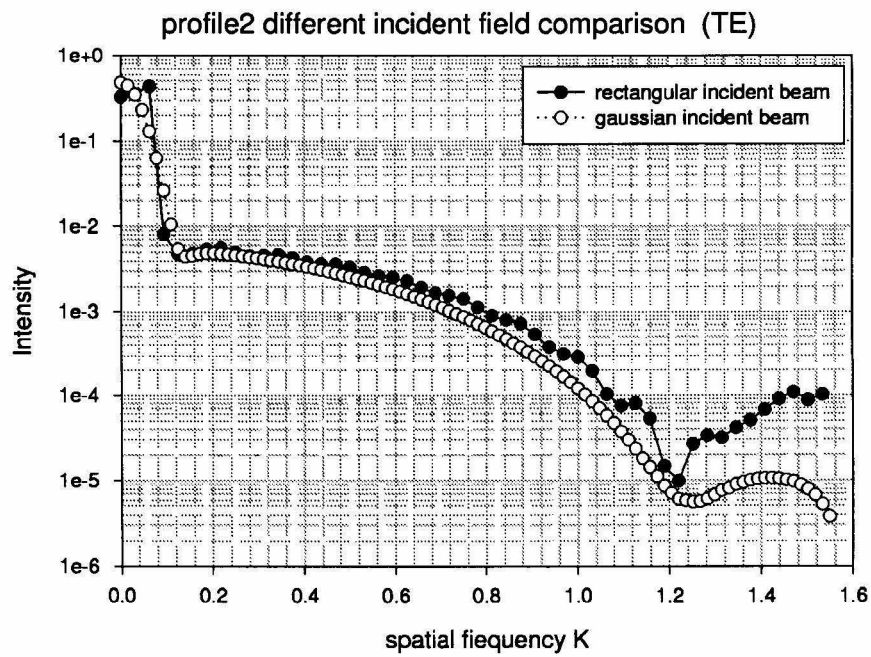


Figure 5.3: Far field diffraction comparison with rectangular incident beam and Gaussian incident beam.

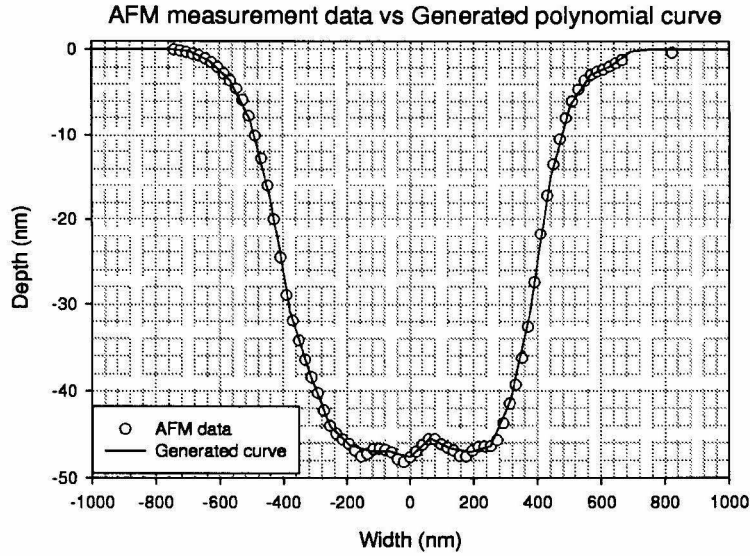


Figure 5.4: Comparison between AFM curve and sampling curve. Illustrated with profile2 contour.

5.2.2 Sample profile input

Four samples have been made for our modeling/measurement comparison study. All profile surfaces are measured using AFM first so that we have a certain number of data points along the surface curvature. The software package requires an analytical function form for each sample profile so that the necessary sampling points as well as the grid spacing along the contour can be generated for calculation. For this reason, we coded a new subroutine, compatible with the original program package, doing Spline interpolation [4] of the AFM data for each sample surface contour. Obviously, with more AFM measurement data points, this interpolating method has better accuracy. Figure 5.4 illustrates the AFM measurement data points and the calculation sample profile generated from the interpolating method. Those two curves fits very well.

5.2.3 Convergence issue

The original program package was developed especially for an optical data storage system, where a high numerical aperture (NA) focusing lens is used to achieve large storage capacity. For the current experiment, the NA of focusing lens is about 0.05 since we are measuring the sample's scattering. For the program's convergence-checking, we basically have two parameters to vary: the whole integral region/truncation length and the contour grid spacing. For small NA, the focused spot size is relatively large so that we need to extend the truncated length a little bit longer to collect all the possible contributions outside the feature region. For the grid space, there is a trade-off between smaller grid space and longer calculation time as well as the available computer memory. The convergence-checking normally takes much longer than the final run for the result since we need to extend further to make sure that the current parameter's output is really converged. Furthermore, for the calculation of multiple samples, the convergence test can be done first for the narrowest and deepest profile, as long as this profile converged with the chosen truncated length/grid space, all other profiles are guaranteed to be converged with the same truncated length/grid space.

5.2.4 Incident angle

In our experimental setup (see Figure 5.6), the reflected scattering data (specular data) within the NA region can't be collected due to the blocking from the focusing lens. So we rotate the sample 15° to collect the scattering data within this region. In order to accurately model this experimental modification, we modified the program package to this experimental case by assuming the focused light is illuminating the sample 15° from sample normal. This is done by shifting the incident field at the front focal plane by $\sin(15^\circ)$. The usual incident field is defined as Equation 5.2. For 15° case, we changed it to

$$I(u) = e^{-\frac{(u - \sin 15^\circ)^2}{NA^2}} \quad (5.3)$$

For the normal incidence case, in order to reduce the reflectance between sample surface and focusing lens, the scattering data is collected at 5° incident to sample normal. We can simply change 15° in Equation 5.3 with 5° for this scattering region modeling.

5.3 Experimental measuring

5.3.1 Sample fabrication and characterization

Starting with a polished Al substrate plated with a $10\mu\text{m}$ thick layer of NiP, we fabricated a series of sub-wavelength features in the NiP layer using a Micron 9500 focused ion beam (FIB) system. A 50 nm aperture, a beam current of approximately 50 pA, and doses in the range $0.1\sim 0.5\text{ nC}/\text{cm}^2$ were used to mill away material and create uniform linear trenches with well-defined dimensions. These trenches were designed to be $100\mu\text{m}$ long with varying widths and depths. They were fabricated in a linear array with a spacing of $150\mu\text{m}$ between adjacent trenches. Reference marks were also milled into the NiP so that the trenches could be easily located during subsequent measurements.

The topography of each trench was measured using a Digital Instruments Dimension 5000 Atomic Force Microscope (AFM). Standard silicon cantilevers with integrated single-crystal silicon tips were used in the intermittent contact mode (Tapping Mode) for height measurements. The nominal tip radius of curvature was $5\sim 10\text{ nm}$. Data was acquired over a $5\mu\text{m}\times 5\mu\text{m}$ area and averaged along each trench. The cross-sectional analysis results are shown and summarized in Figure 5.5. The root mean square (RMS) roughness of the NiP surface adjacent to the trenches was measured to be 0.5 nm . Those 4 profiles range from 180 nm wide, 15 nm deep to 840 nm wide and 170 nm deep. Profiles 1 and 3 consist of a structure pair for sub-wavelength region; profiles 2 and 4 consist of the other pair for above wavelength region. We are expecting different performance from those two structure pairs.

Using a Woollam M44 ellipsometer, the index of refraction of the NiP layer was

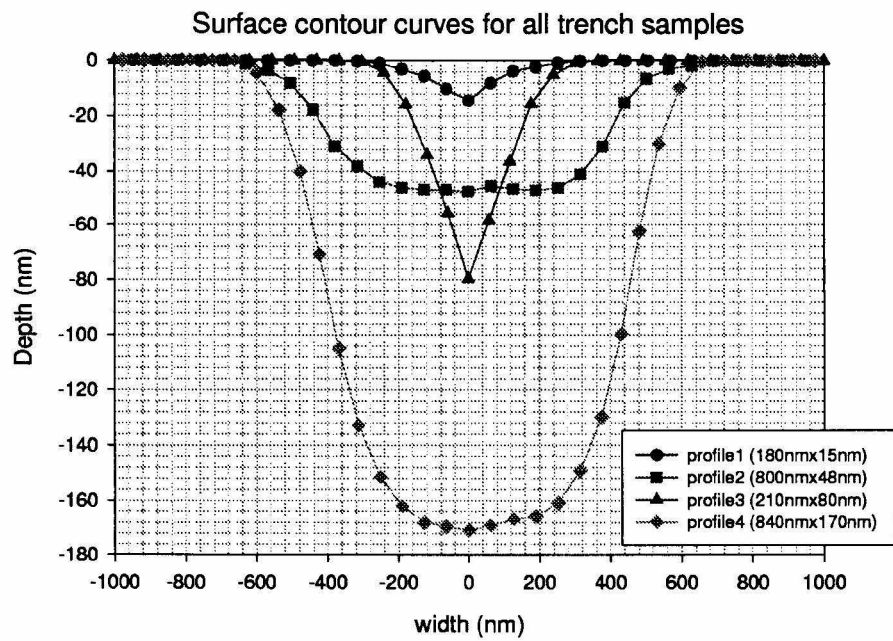


Figure 5.5: Sample surface contours measured by AFM.

measured to be 2.07-2.78i for incident light with a wavelength of 633 nm. Ellipsometric data was collected over a range of wavelengths from 500~800 nm with a fixed incident angle of 65° and analyzed with the WVASE software package provided with the Woollam ellipsometer. The index of refraction was determined by fitting the ellipsometric data with a Lorentz Oscillator model. This index data and the AFM profile measurements are used as inputs to the numerical model described previously.

5.3.2 Scatterometer system

To measure the optical scattering from our sub-wavelength features, we set up a system as in Figure 5.6. The uniform linear trenches scatter light in only one dimension, so we designed the system to make one-dimensional measurements. A 10 mW HeNe laser with a wavelength of 632.8 nm provides a Gaussian beam with a full width at half maximum (FWHM) of 0.48 mm. Neutral density (ND) filters in combination with a liquid crystal variable retarder (LCVR) and polarizing beam splitter (PBS) allow fine tuning of the laser power over a wide range of powers from 10 mW down to 10 nW. The PBS and a removable half-wave plate control the polarization of light incident on the samples so that the E-field is either parallel to the plane-of-incidence (TM/p-polarized) or perpendicular to the plane-of-incidence (TE/s-polarized). The PBS transmits TM/p-polarized light with an extinction ratio of 1600:1. The half-wave plate can be inserted into the beam downstream from the PBS in order to rotate the polarization through an arbitrary angle. In these experiments the half-wave plate is oriented to transmit s-polarized light with an extinction ratio of 1300:1. Next, a two-lens telescope expands the beam by a factor of 5.9 so that the final focusing lens ($f = 50.8$ mm) produces a focused spot with a FWHM of $5\text{ }\mu\text{m}$ at the sample surface. Using a Photon, Inc. BeamScan Laser Beam Profiler (Model 2180), we measured the FWHM of the focused spot to be $6\text{ }\mu\text{m}$.

To facilitate the description of how we orient our samples, we define a rectangular coordinate system that has its origin at the point where the incident beam comes to a focused spot at the sample surface, as shown in Figure 5.7. We call the intersection

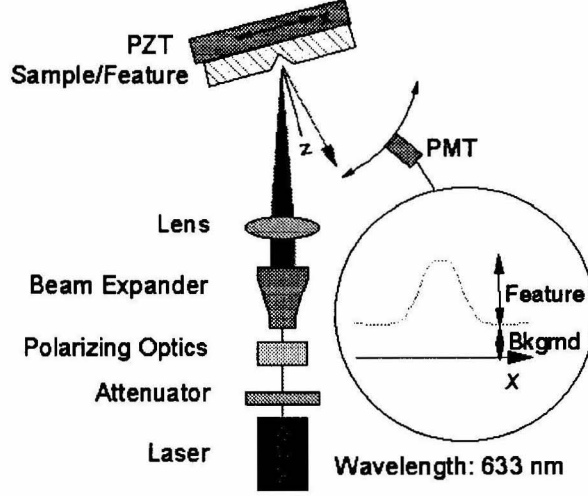


Figure 5.6: Experimental setup of measuring the scattering from sub-wavelength structures.

of the plane-of-incidence with the sample surface the x -axis, and we call the surface normal the z -axis. Our features, the trenches and ridges described above, are oriented with their long axis normal to the plane of incidence for all the experiments described here. For non-normal incidence, the polarization of the incident beam is described using the normal conventions for s and p polarizations. Several of the experiments and theoretical calculations are done at normal incidence. Because of the nature of the feature, it is still useful to distinguish between polarization aligned with the long axis of the feature or perpendicular to it. We use a notation such that an s polarized beam will still be referred to as s polarized, even at normal incidence. Since the feature orientation is fixed with respect to the plane of incidence, this means that beams polarized parallel to the feature axis are called S and those polarized perpendicular to the feature axis are called P .

The sample is mounted on a piezoelectrically driven (PZT) stage with a range of motion of 80 μm in the x -direction so that the trenches can be scanned back and forth

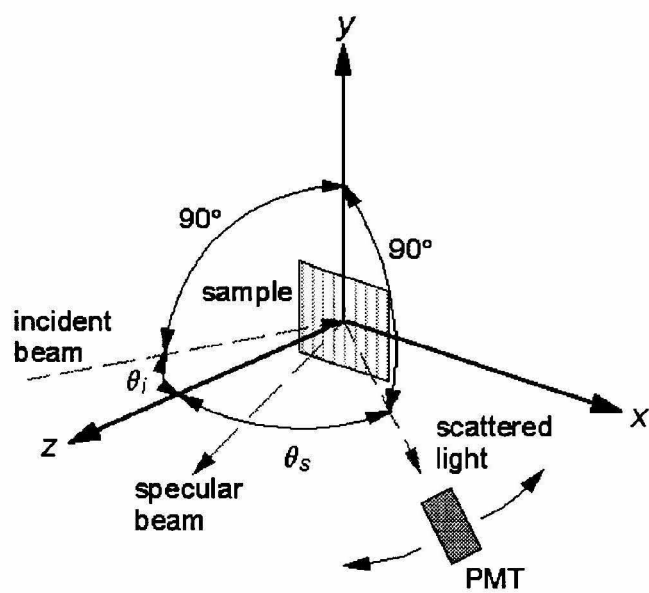


Figure 5.7: Experimental setup's coordinate system.

through the beam. The PZT stage is mounted on an x-y stage so that the sample can be moved in the x-y plane to locate different trenches on the sample surface. In addition, the sample can be independently rotated about the z-axis in order to orient the trenches along the y-direction so that they are normal to the PZT motion.

A Hamamatsu H5784 photomultiplier tube (PMT) is mounted 85 mm from the sample on a rotary stage that independently rotates about the y-axis so that the detector can scan through a range of scattering angles θ_s . In this setup the detector, the sample normal, and the plane-of-incidence all lie in the x-z plane. A narrow slit, 1 mm wide and 10 mm high oriented in the y-direction and bisected by the x-z plane, is mounted to the PMT 12 mm in front of the detector face so that only a thin band of light is collected for each θ_s . The slit is covered with diffusing material in order to spread this thin band of light more evenly over the detector face. The dimensions of the slit allow the PMT to collect all of the light in the y-direction over a small region $\Delta\theta_s = 0.81^\circ$ about θ_s . This collection geometry reduces our scattering measurements to one dimension, which facilitates comparison with the numerical modeling. In addition to the slit and diffuser, we have also mounted a laser line bandpass filter with a FWHM pass band of 10 nm in front of the detector face to suppress ambient light. To minimize multiple reflections between the filter and the sample, we have oriented the filter so that the less reflective side faces the sample.

The angle of incidence θ_i is changed by rotating the sample (along with the PZT stage and the x-y stage to which the sample is mounted) about the y-axis. For these experiments, we use $\theta_i = 5^\circ$ and $\theta_i = 15^\circ$. Using $\theta_i = 5^\circ$ we can easily collect data on both sides of the specular beam without worrying about laser feedback from the specular beam re-entering the laser cavity. However, with this geometry we can not measure the specular beam because the detector blocks the incident beam in this region. In order to measure the specular beam, we must increase the angle of incidence. Arbitrarily, we choose $\theta_i = 15^\circ$.

5.3.3 Scattering measurements

To measure optical diffraction from our FIB-produced trenches, we focus the incident beam on a single trench and rotate the PMT about the y-axis. In this way, we are able to measure the light irradiating the detector at different spatial frequencies k , where

$$k = \frac{\sin \theta_s - \sin \theta_i}{\lambda} \quad (5.4)$$

where θ_s is the scattering angle from sample normal, and θ_i is the incident angle from sample normal, λ is the illumination wavelength (633nm throughout our whole experiment). This spatial frequency k -space may be divided into two distinct regions: (1) the specular region in which the specular beam makes a significant contribution to the measured irradiance, and (2) the scattering region in which the specular beam makes a negligible contribution to the measured irradiance. We make this distinction because we use a different measurement technique for each region. In our experiments, we have defined the transition between these two regions to be at $|k| = 0.2$.

For $|k| < 0.2$, we adjust the x-y stage so that the incident beam is centered on a stationary trench, and we measure the light irradiating the detector. For $|k| > 0.2$, we oscillate the trench back and forth through the focused laser spot using the PZT stage. When the trench is not under the spot, the PMT detects only the tail of the specular beam and background light such as that due to surface roughness, ambient light, and scattering from optical components. When the trench is centered on the spot, however, the PMT detects a maximum in scattered light due to diffraction from the feature. So, as the trench is scanned through the beam, the PMT detects a peak on top of a flat background, as shown in the schematic plot of scattered light in Figure 5.6. We define the scattered light in this region as the difference between the peak and the background, which allows us to measure weak diffracted light signals in the presence of unwanted background light. Because the measured irradiance falls so quickly in the region $|k| < 0.2$, we rotate the PMT about the y-axis in relatively small increments of 0.25° . In the region $|k| > 0.2$, the irradiance changes more slowly,

and we rotate the PMT about the y-axis in larger increments of 2.5° .

In order to insure that the light irradiating the PMT remains within the detector's optimal range, we collect data in sets with different incident laser powers that are appropriate for different regions of k-space. To measure the incident power used in a particular data set, we place a Newport optical meter (Model 2835-C) in the beam between the beam expander and the final focusing lens.

There are two primary sources of error in these experiments. The first involves the accuracy with which we can center a stationary feature beneath the beam when we collect data in the region $|k| < 0.2$. This error is negligible at $k = 0$, but can be as much as 15% at $k=0.2$. The second involves the non-uniform width (7% variation) of the collection aperture used in front of the PMT. This error just shifts the data by a (small) constant factor.

During the measurement, we first verify the numerical aperture of the focusing lens by comparing the experimental data with the numerical modeling prediction. Figure 5.8 shows the experimental scattering data for mirror surface as well as the corresponding modeling results from different NAs. It clearly verifies that NA of focusing lens is 0.05, which is used throughout the whole numerical modeling.

5.4 Comparing measurement and modeling results

5.4.1 AFM curve remeasurement story

During the first phase of this work, for the data comparison, we conformed to the Bidirectional Reflective scatter Distribution Function (BRDF) since it is widely used in scattering technology field. The definition of BRDF is given by

$$BRDF = \frac{dP/d\Omega}{P_i \cos \theta_i \cos \theta_s} \quad (5.5)$$

where $dp/d\Omega$ is the power per sterradian, P_i is the incident power, θ_i is the incident angle, measured from the sample normal, and θ_s is the scattering angle, measured from the specular peak. The procedure of comparison is following: First, we get the contour

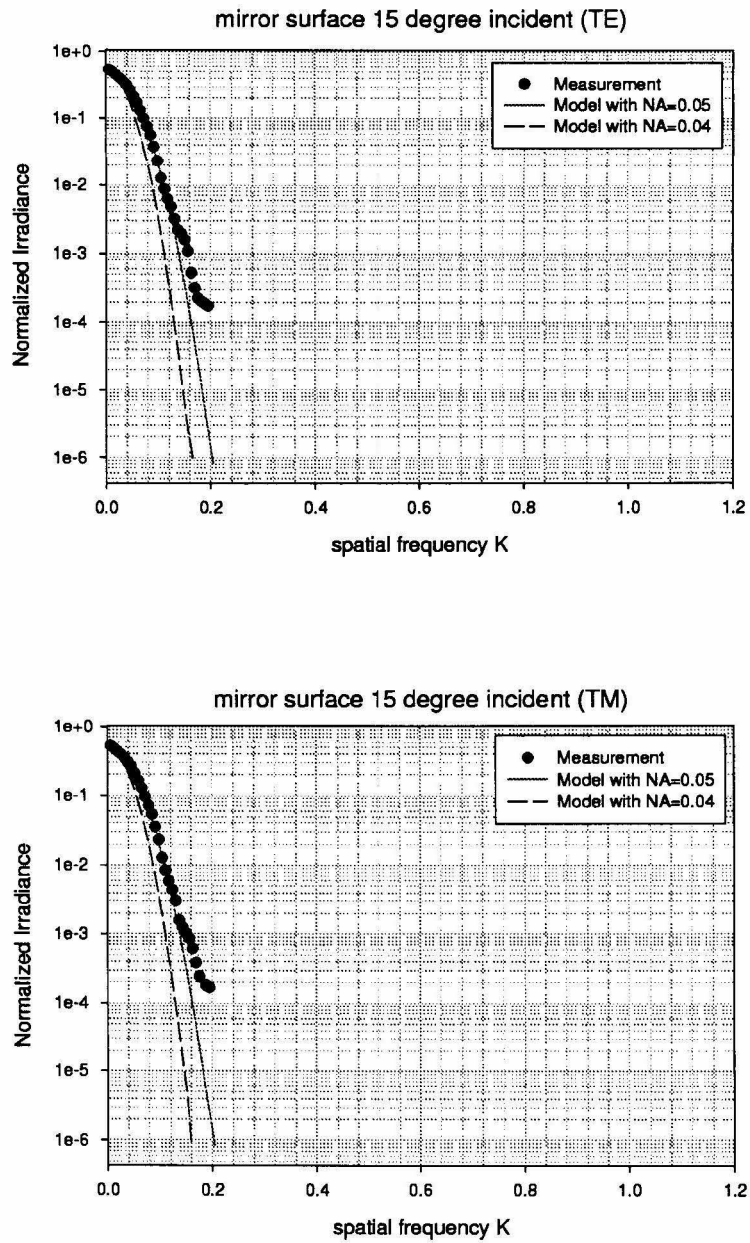


Figure 5.8: Experimental verification of the numerical aperture of focusing lens.

data from AFM measurement, which is used to calculate the far field diffraction from modeling. Then the sample's scattering is measured at each scattering angle. Finally, we compare the modeling prediction and the experimental data.

There is an interesting story about the profile's AFM measurement. The first round of comparison ended up with an offset between experimental data and the numerical modeling. After revisiting several affecting factors, we finally began to believe the modeling and suspect the AFM curve data from the argument that the finite size of the AFM scanning tip might contribute to the offset. In other words, when measuring the sample surface, the AFM outputs might have some error due to the fact that the AFM tip can't always reach the actual bottom of the sample when the sample has a very narrow bottom or the wall angle is very sharp. Because of that, we carry out an optimal searching of profile curves, which basically searches the corresponding AFM contour curve whose diffraction prediction has the best agreement with the experimental data. Obviously, this searching procedure is assuming 100% correctness of experimental data, which later fortunately turns out to be a quite reliable assumption.

Regarding this optimal searching, we are basically varying the sample's depth and width around the original AFM curve data with two claims in mind. The first one is saying that wider trench gives faster falling-off slope at scattering region. The other one is that deeper trench gives stronger scattering magnitude. Furthermore, we should make sure to obtain the best agreement in both TE and TM mode in the same time. Finally, in order to verify the optimal searching results, we also remeasure those four samples' surface profiles. It surprisingly gives out a large difference between original AFM measurement and this new AFM measurement. Figure 5.9 illustrates all those results. As we can see, the new AFM measurement agrees excellently with the optimal searching curves. This tells us two things. One is that our numerical modeling offers a powerful and reliable reference for monitoring the AFM measurement. The other one is that our experimental scattering data are quite trustable. The first round modeling and measurement comparison's discrepancy is not caused by the numerical modeling or scattering experiment but the wrong AFM measurement. As a final note,

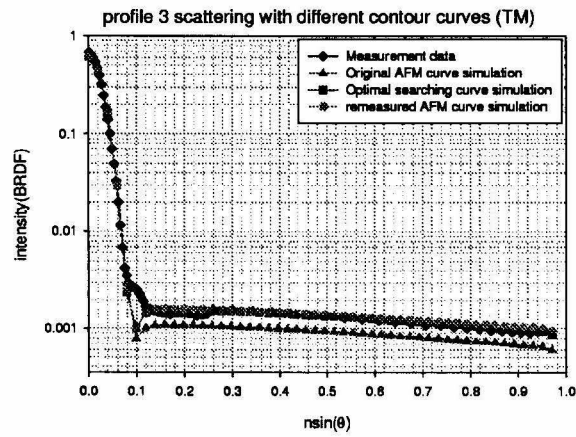
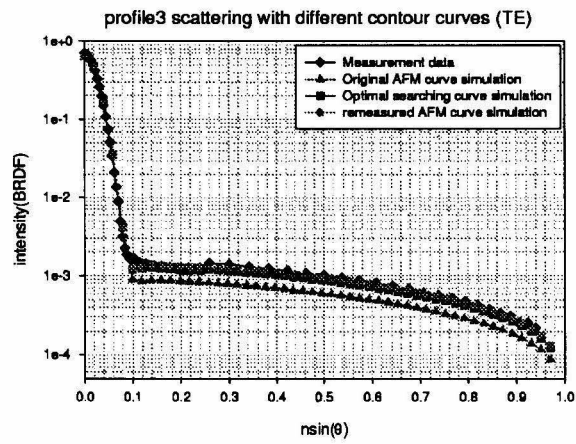
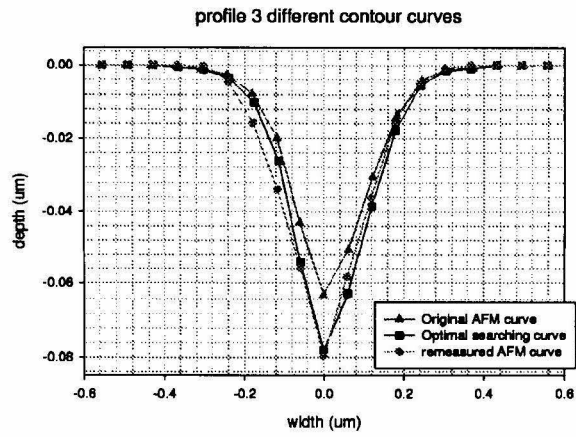


Figure 5.9: Optimal profile searching data plots.

the 4 profile contours illustrated in Figure 5.5 are obtained through the previously discussed optimal searching and remeasurement.

5.4.2 Intensity comparison

It turns out that BRDF is not a good parameter for our modeling and experimental comparison, especially in the incident angle case where the scattering angle has different definition for experiment and numerical modeling. For modeling, the scattering angle is measured from sample normal. This gives the same value of scattering angle for both 15° and normal incident cases since we do not rotate the sample at all. But, experimentally, the scattering angle is measured from the specular peak. For the 15° incident angle, the specular peak is rotated 15° from the peak corresponding to normal incident case. This gives a different value for the scattering angle. After trying for a while to keep the experimental data and modeling calculation within the same comparable frame, we realized that a more natural and physically simple parameter for comparison is the scattering intensity. So, for the latter phase of the work, we used the scattering intensity.

Here we show two sets of data for comparison. Figure 5.10 and Figure 5.11 are the plots of the scattering reflection with the beam incident at 5° to the sample normal. Figure 5.12 and Figure 5.13 are the plots of specular reflection with the beam incident at 15° to the sample normal. As explained in previous section, the data are plotted with the x axis being spatial frequency (see Equation 5.4). In all those figures, both the measured and modeled irradiance results have been normalized so that the peak irradiance of the incident beam is unity. Accordingly, the peak irradiance of the specular beam for a mirror surface is simply the reflectance R , as in Figure 5.8 at $k = 0$. It is also apparent from Figure 5.8 that the measured irradiance is Gaussian over more than two orders of magnitude. However, at low light levels the measured irradiance becomes non-Gaussian. This is primarily due to multiple reflections between the sample and the detector. This same non-Gaussian behavior is evident in some plots of Figure 5.10 and Figure 5.13 since the scattered light is

more than four orders of magnitude weaker than the specular peak for some samples. Multiple reflections and other sources of background light do not affect the measured irradiance in the region $k > 0.2$ because they are subtracted out by the data collection technique used in this region, as described in previous section. Overall, the excellent agreement between the model predictions and the actual measured scattering give us confidence in the validity of the model. It works well throughout the critical transition region from features larger than the wavelength to subwavelength structures.

Specifically, in Figure 5.10 and Figure 5.11, for the profile 2 and 4 pair, the predicted second dip is clearly observed in the experiment. Even more, the predicted dip location is strongly justified by the experiment. For the profile 1 and 3 pair, the predicted scattering curve is just slightly offset from the experimental data with a negligible value. The overall data curve is mapping extremely well.

In Figure 5.12 and Figure 5.13, for profile 2 and 4 pair, the predicted first dips are clearly demonstrated in the experiment. Again, the location of these dips are agreed quite well between prediction and experiment. For profile 1 and 3 pair, the predicted scattering curve shape is almost overlapped with the experiment data curve. The little first dip predicted from profile 3 is observed in experiment too.

Besides the demonstrated excellent agreement within the whole spatial frequency region, there are two interesting minimums (dips) in some of the scattering curves. The first dip at small scattering angle around the specular region can be explained by following: the reflected field from the top flat surface part is interfering with the reflected field from the sample bottom region, confined within the incident beam's Gaussian distribution. At certain scattering angle, those two reflected fields have a π phase difference so that de-construction happens, providing an intensity minimum (dip). The second dip is found only for those profiles whose widths are comparable to one wavelength. The explanation is that we can sort of consider two edges on contour surface, where the surface charges have large peaks, to be two separate point sources. Those two point sources interfered together in far field, at some scattering angle, their phase difference is π , which gives another intensity minimum (dip).

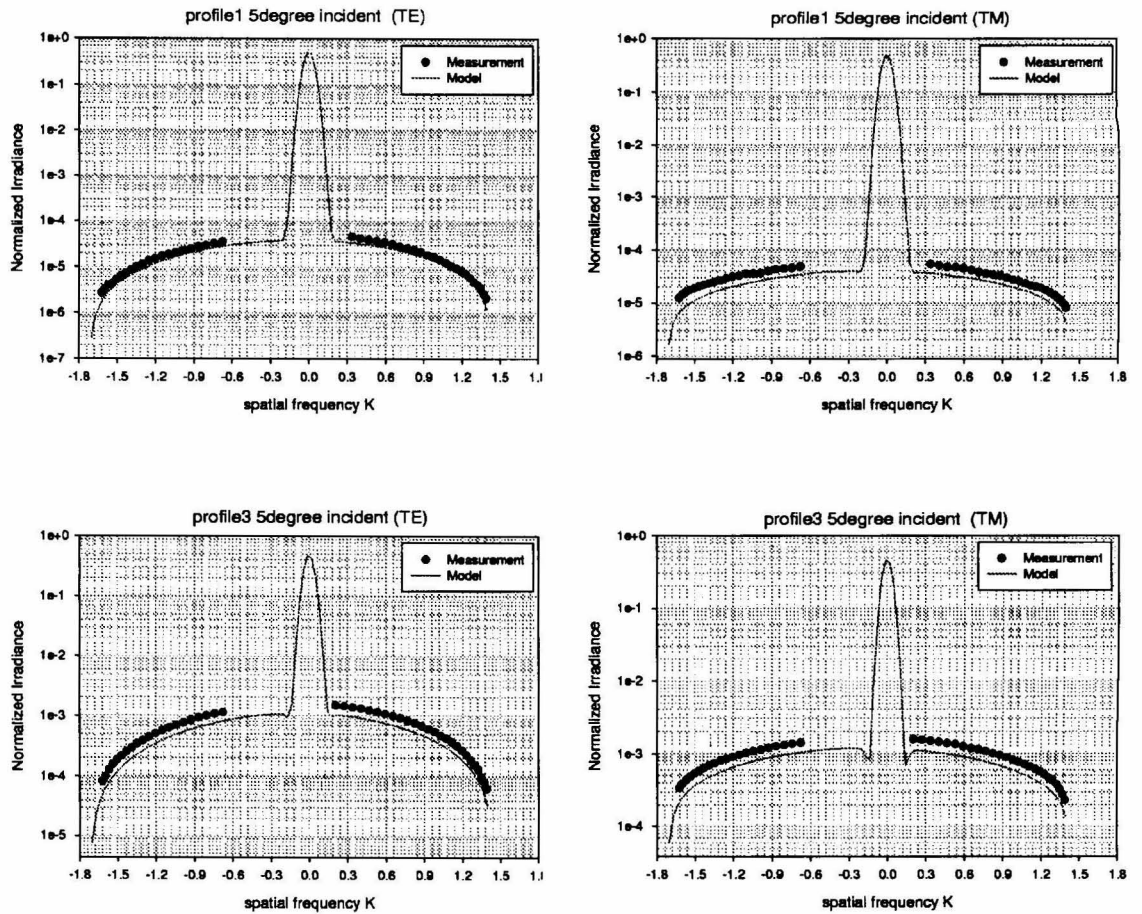


Figure 5.10: Scattering region data comparison between experiment and numerical modeling for all narrow profiles (1 & 3).

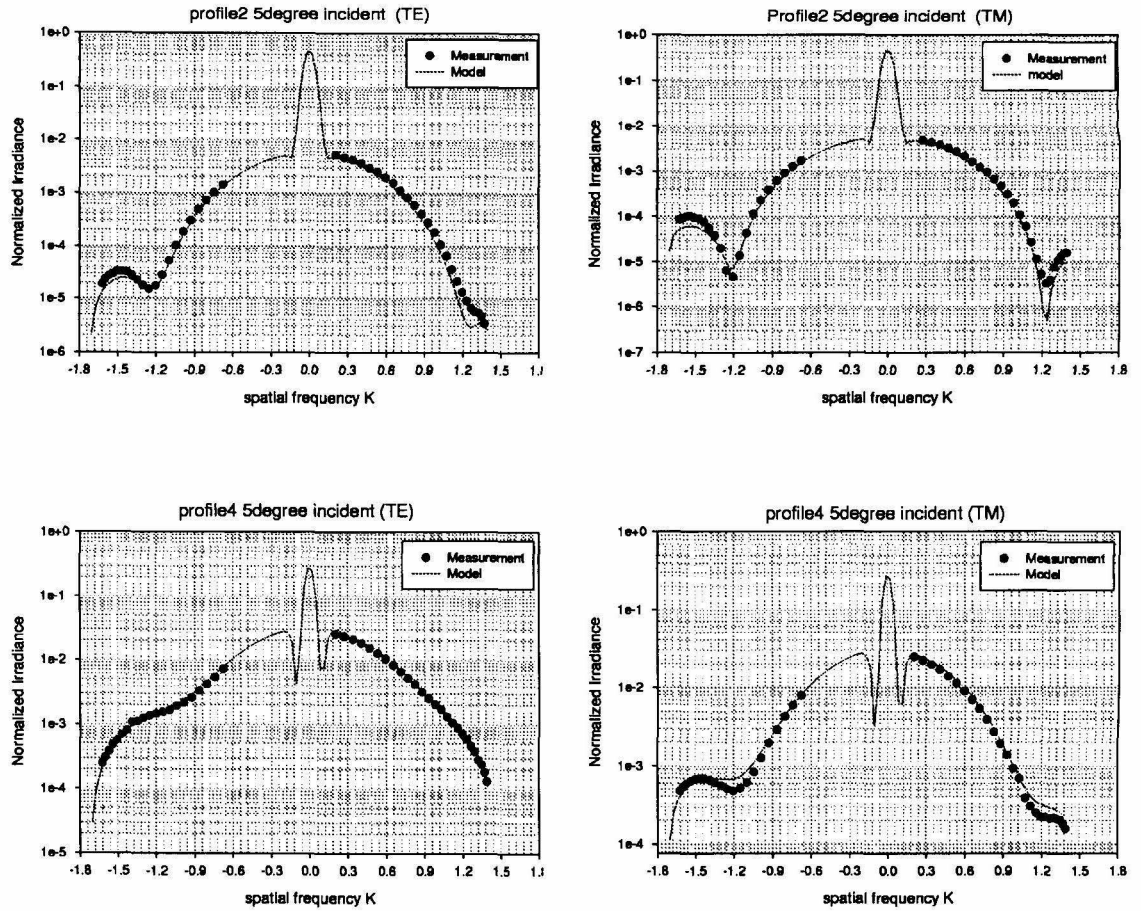


Figure 5.11: Scattering region data comparison between experiment and numerical modeling for all wide profiles (2 & 4).

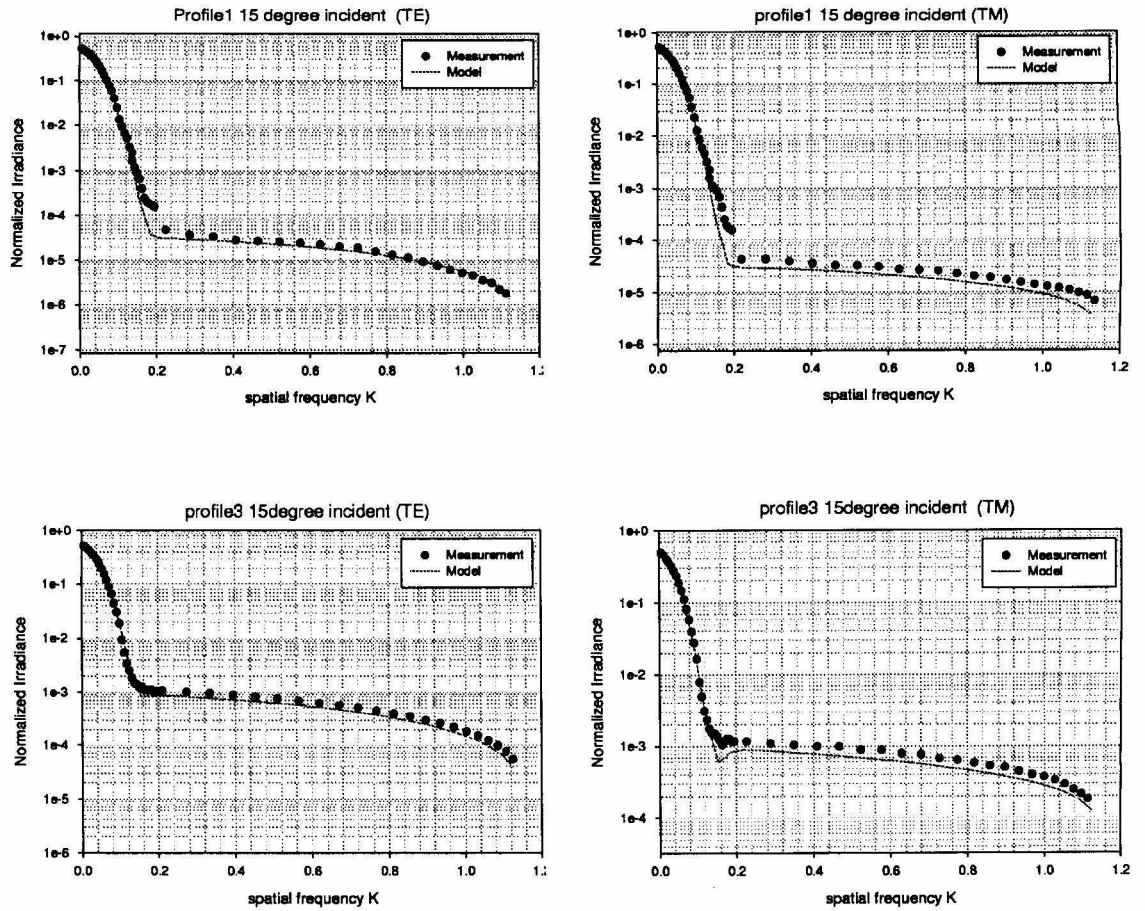


Figure 5.12: Specular region data comparison between experiment and numerical modeling for narrow profiles (1 & 3).

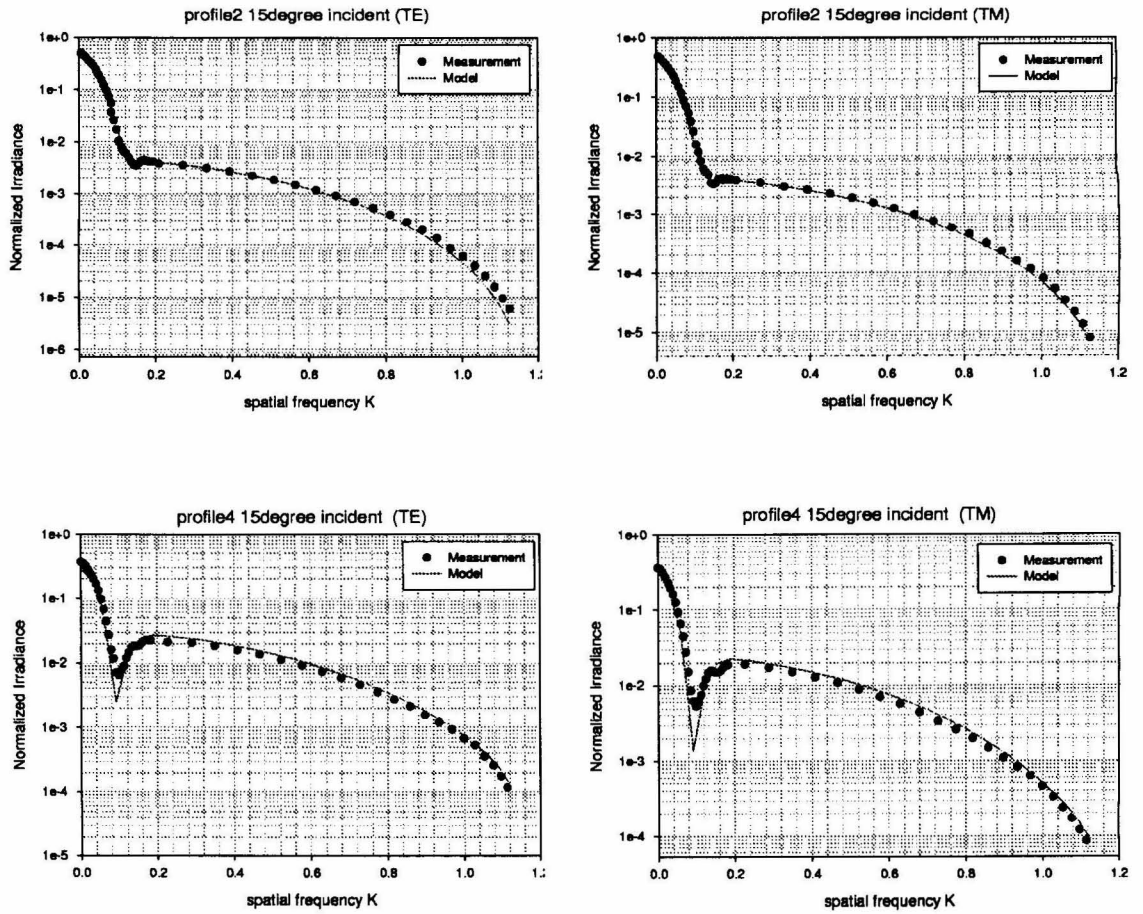


Figure 5.13: Specular region data comparison between experiment and numerical modeling for wide profiles (2 & 4).

5.5 Further discussion

From the previous comparison between experiment and modeling, we are quite confident about our modeling now. The next logical step is to see whether we can learn something from it. Here we discuss two interesting issues. One is to explore the first dip in scattering curve to extract the subwavelength structure's depth/width information as much as possible. The other one is to see whether we can have some way to distinguish the trench and ridge profile by combining the TE/TM scattering data.

5.5.1 Aspect ratio extraction

The previous explanation of the first dip in scattering curve gives us some hints that this dip contains some contour information, such as depth and width. In order to explore that further, we constructed 4 constant volume trenches with different aspect ratios of width over depth. For those small features, intuitively from scalar diffraction theory, we would expect that the level of scattering depends only on the volume (area in cross-section) of the profile, not the shape. So it is almost impossible to distinguish these profiles due to their equal volume. But with our strict vector theory, if it turns out that we can somehow extract the aspect ratio for this level of subwavelength structure, it would be very exciting news! The 4 profiles we proposed are plotted and summarized in Figure 5.14. The volume (2-D) of those profiles is around $10,000 \text{ nm}^2$ with the depth/width aspect ratio ranging from 0.24 to 1.2. The two extreme cases are profile A and D, which have 200nm width/50nm depth and 92nm width/110nm depth respectively.

Figure 5.15 illustrates the calculation results of those 4 profiles with trench shape at normal incidence case. As we can see, the scattering portions of the diffraction curves from those profiles are pretty much the same in both TE and TM mode, which agrees well with the scalar theory explanation. This makes it very difficult to extract the aspect ratio information from the scattering region at either TE or TM mode. However, in the specular region, for TM mode, there is a dip present for all profiles. Even more, if we zoom in on that dip region as shown in Figure 5.16, it is clear that

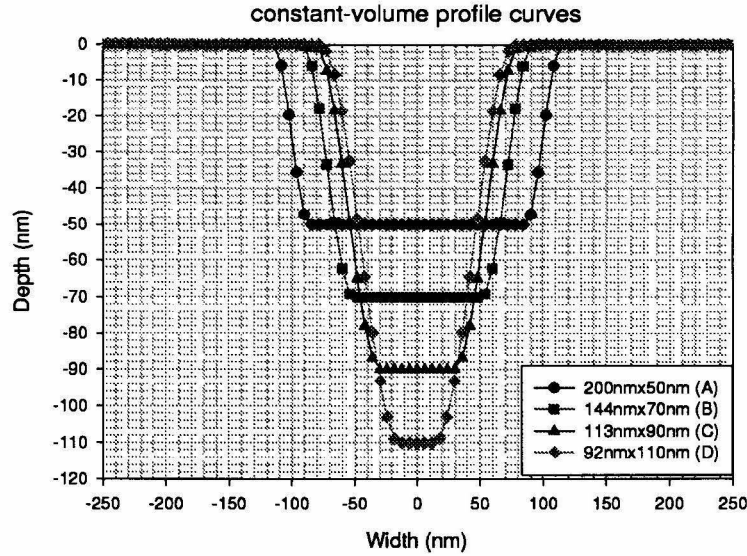


Figure 5.14: Constant-volume profiles contours.

the magnitude of the dip is closely related to the aspect ratio. A larger depth/width aspect ratio corresponds to a deeper intensity dip in the specular region. This offers us a very powerful tool to extract the aspect ratio easily by simply measuring the TM mode specular region data.

The reason that we have a dip for TM mode but not for TE mode is explained by the waveguide model. We can consider the trench as the waveguide with a feature size of one wavelength. The TE mode diffraction from the contour is then similar to the light propagation within the waveguide. (Note that our TE and TM modes don't translate directly to waveguide TE and TM modes.) From the waveguide theory, the cut-off frequency is about half of the propagating wavelength (about 312nm in our case). All those constant volume profile widths are smaller than this cut-off frequency, which means that light can not penetrate well into these narrow, deep contours. Because of that, TE sees smaller volumes and gives lower scattering. (This property can also be used for distinguishing trenches and ridges, which will be discussed later.)

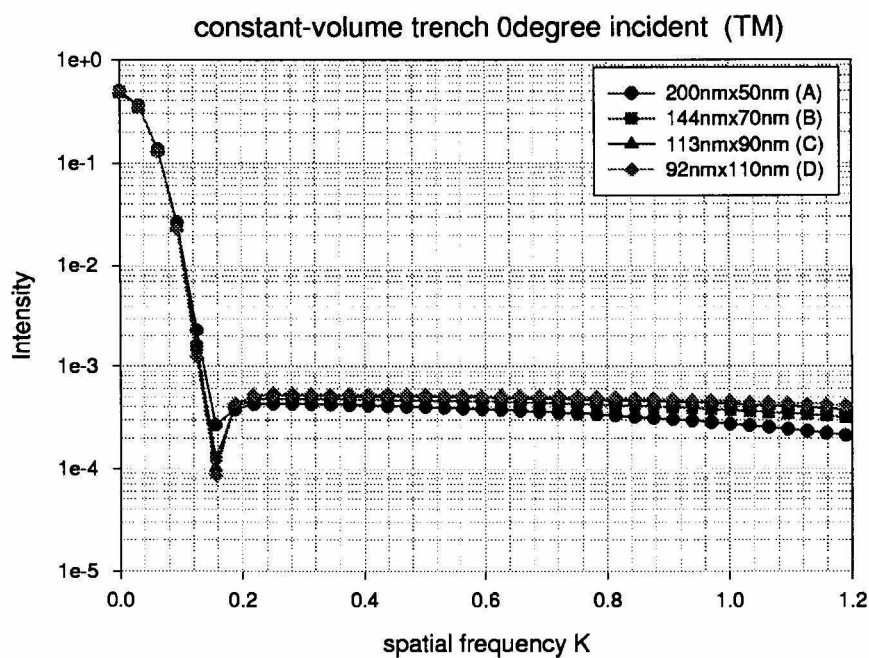
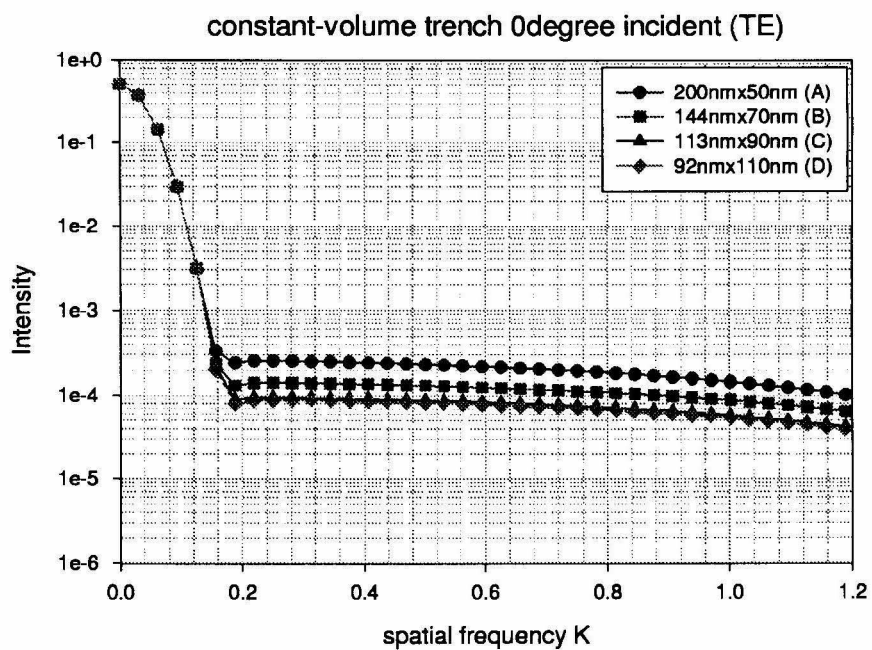


Figure 5.15: Constant-volume trenches aspect ratio extraction calculation results.

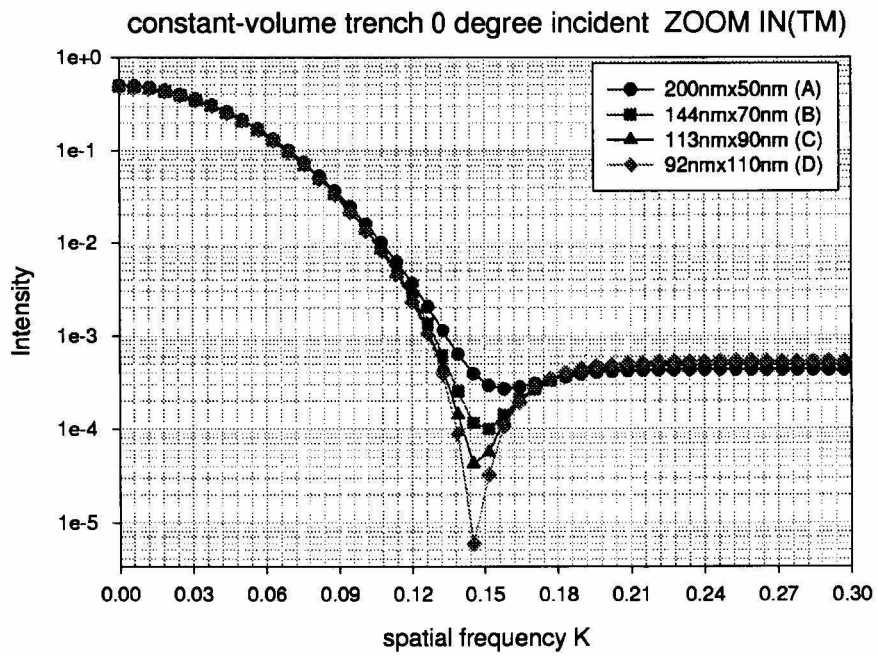


Figure 5.16: Zoom in plot of the specular region data at TM mode for all four trenches under normal incident.

For TM mode, however, there is no waveguide cut-off frequency limitation here. The light can still propagate into the contour, then reflect and interfere to generate a dip in the specular region. Obviously, the depth as well as the width information contributes to the dip's magnitude. This is where the idea of aspect ratio extraction essentially comes from. From those modeling results, this aspect ratio extraction technique is proved to be quite reliable and powerful.

To see if this aspect ratio extraction technique could be applied to any other surface geometry, we also calculated those constant volume profiles with ridge shape by inverting the depth into the height. Figure 5.17 shows the same trend of performance as trench shape for both TE and TM mode. Similarly, we zoom in the dip region for the TM mode as shown in Figure 5.18. This time, we can extract the aspect ratio if the aspect value is smaller, for example, profile A and B, or the difference between the aspect ratio is large, for example, profile B and D. For profile C and D, it is relatively hard to extract exactly the aspect ratio information since the dip's magnitude is roughly the same (although there does have small difference). Given the limited aspect ratio extraction ability from ridge profiles, it seems that this aspect ratio extraction technique we proposed works well only for trench profiles. The basic reason is that the waveguide model that works quite well for trench profiles is not valid for ridges.

5.5.2 Distinguishing trenches and ridges

From the previous comparison between trench and ridge profiles, one natural question is: Do we have some method to easily distinguish trenches and ridges? The short answer is YES! Actually we developed two approaches that both turned out to work quite well.

The first one is to distinguish trench and ridge from normal incidence by combining TE and TM mode scattering data. As explained before, for trench profiles, the TE mode scattering is smaller than the TM mode since it does not penetrate as well as TM mode does. However, for ridge profiles, the TE mode scattering is stronger than

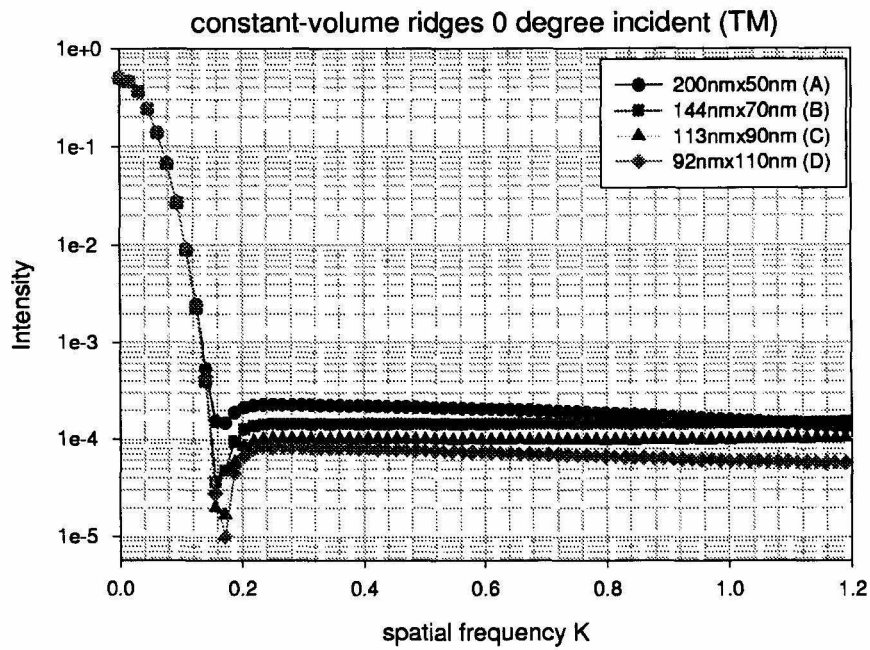
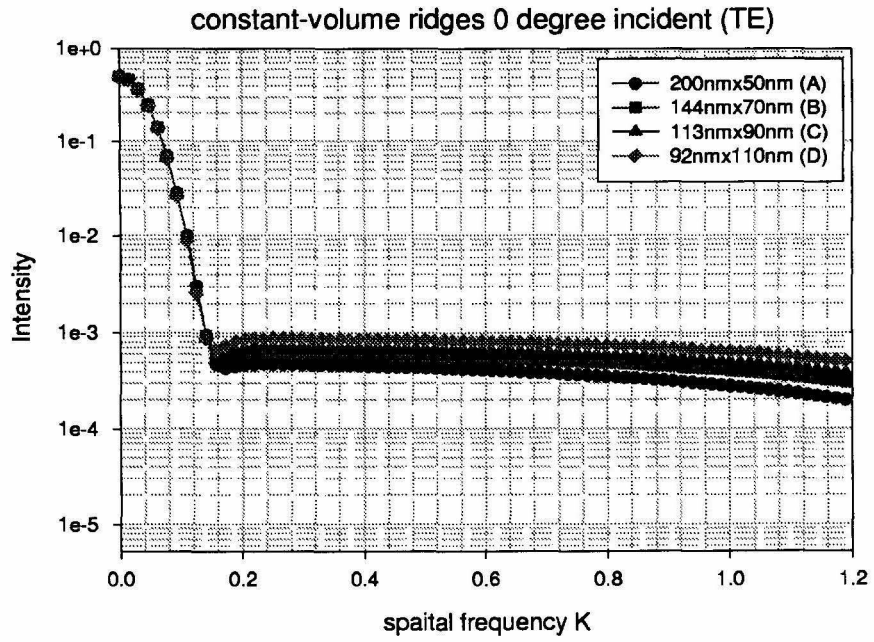


Figure 5.17: Constant-volume ridges aspect ratio extraction calculation results.

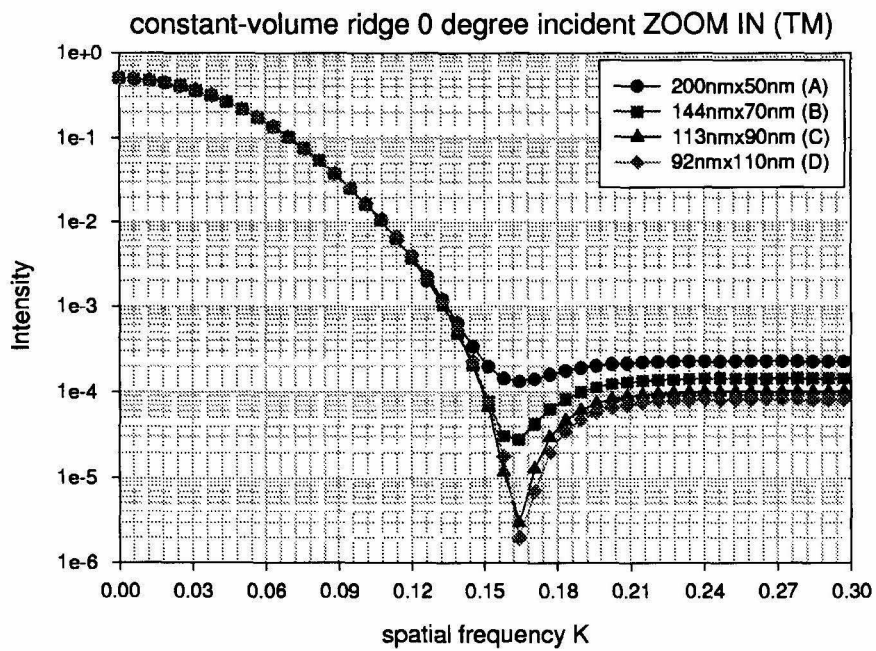


Figure 5.18: Zoom in plot of the specular region data at TM mode for all four ridges under normal incident.

the TM mode. This gives us a hint that we could use the TE/TM scattering intensity ratio to distinguish trenches and ridges. In order to justify this claim, we calculate the TE/TM scattering intensity ratios at different spatial frequencies. Figure 5.19 shows the TE/TM ratios for different aspect ratios of trenches and ridges at two scattering angles 10° and 40° (corresponding to spatial frequency of 0.3 and 1.0 respectively in previous scattering plots). As we can see, for ridge profiles, the TE/TM intensity ratio is always larger than 1 and gets bigger for larger aspect ratio. For trench profiles, however, the TE/TM intensity ratio is smaller than 1 and gets smaller for larger aspect ratios. Obviously, TE/TM intensity ratio of 1 is a quite good criteria for distinguishing trench and ridge. Even more, the slope of this TE/TM ratio is related to the contour's aspect ratio, which might be also used for extracting contour's aspect ratio. That the slope is not constant might add some difficulty for quantitative determination of aspect ratio. Nevertheless, the qualitative determination is quite obvious.

The second approach to distinguish trench and ridge is borrowing from the semiconductor wafer inspection industry. For that application, the technique to distinguish between particles on the surface (ridges) and pits in the surface (trenches) is quite desired. Considerable experimental and theoretical work has been done where the particles are modeled by spheres and ellipsoids [30, 31]. Based on this work, a common technique has been adopted by many vendors of inspection equipment that relies on using oblique incident P polarization for illumination. It has been found that the forward and backward scattering contributions from a sphere on the surface are relatively stronger than the scattering normal to the surface. For a pit, the opposite is true. Thus using two detectors to monitor forward and backward scattering and ratioing their signal to that of a third detector monitoring light scattered normal to the surface, particles can be distinguished from pits. To verify this fact that TM scattering for large angle of incident will have a minimum in intensity around surface normal direction for particles (ridges), we calculated the far field diffraction of those profiles (shown in Figure 5.14) with 60° incident angle to the surface normal.

Figure 5.20 and Figure 5.21 are the results for trench and ridge shape respectively. As we can see, for trench profiles, both TE and TM do not present the minimum

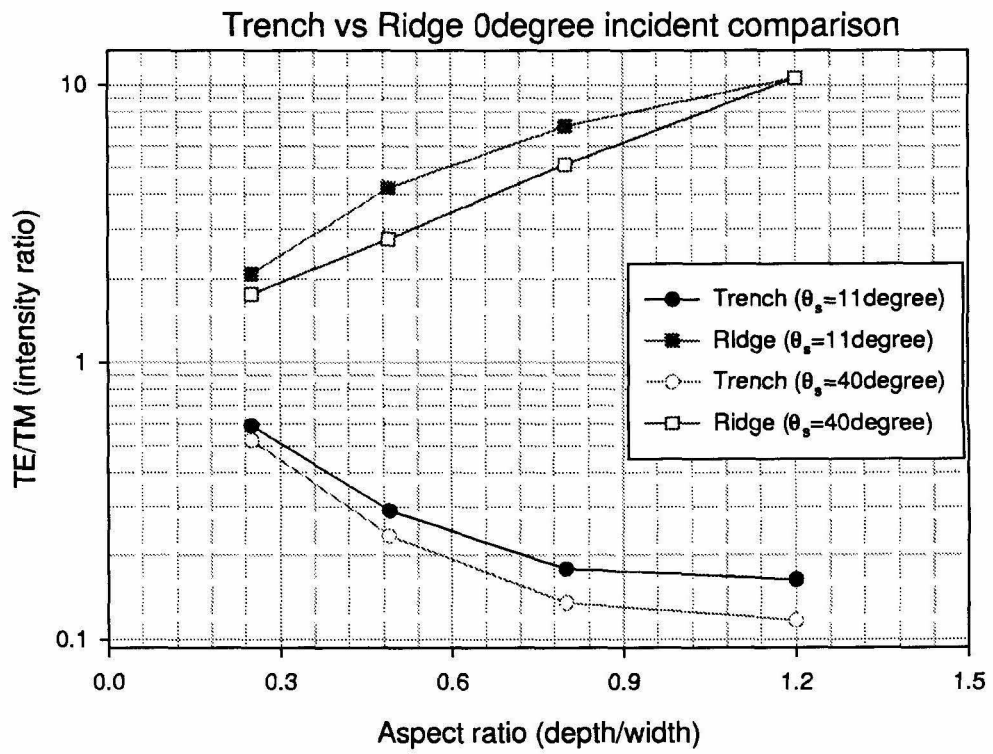


Figure 5.19: TE/TM intensity ratio vs aspect ratio at different scattering angles.

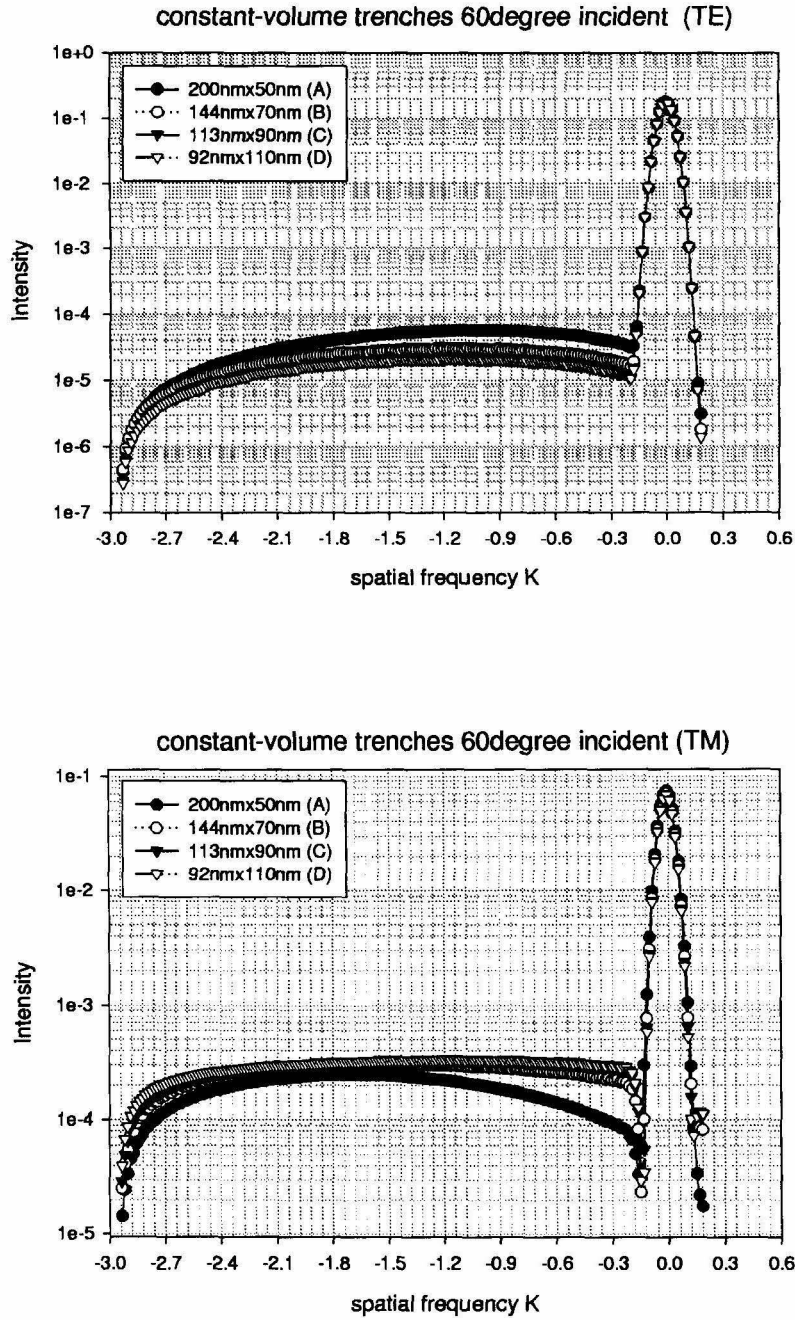


Figure 5.20: Far field scattering calculation of trenches illuminated with 60° to the surface normal.

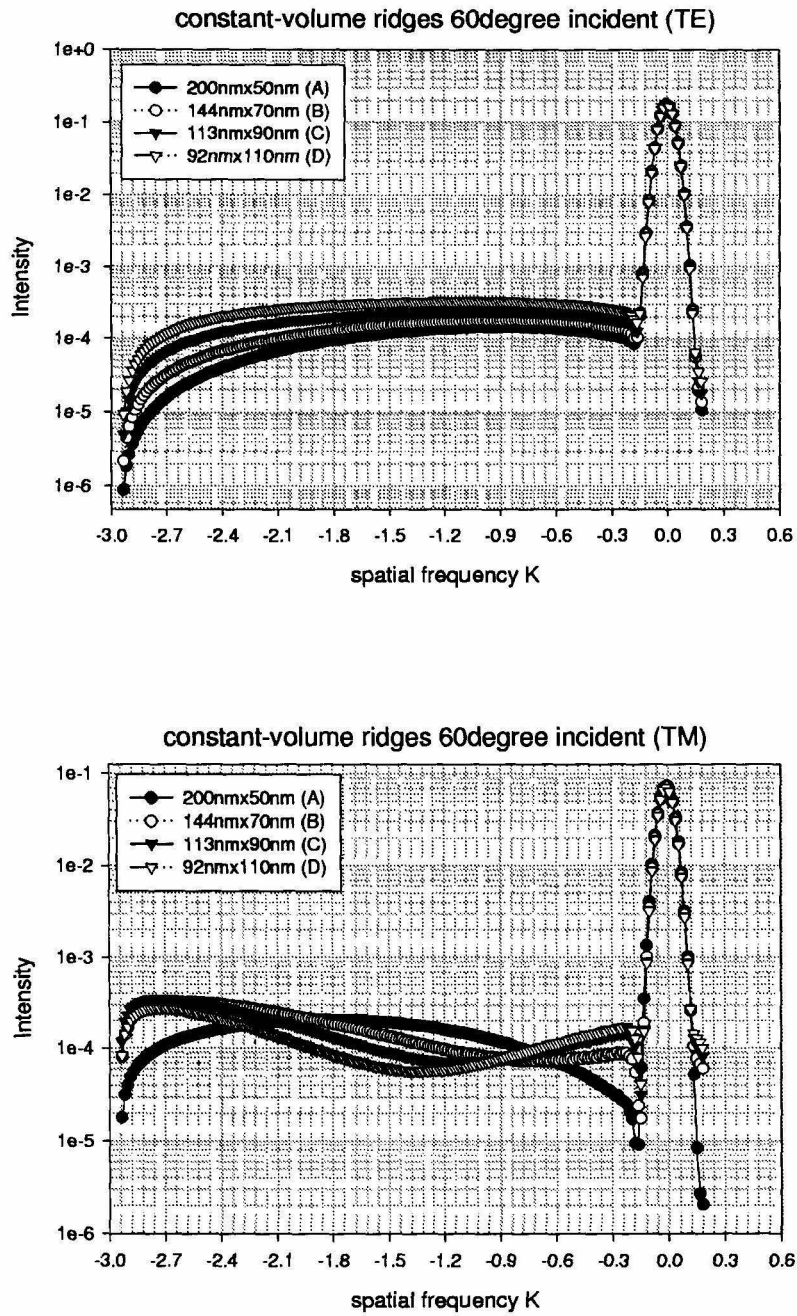


Figure 5.21: Far field scattering calculation of ridges illuminated with 60° to the surface normal.

intensity around the surface normal. For ridge profiles, however, TM mode does clearly present the minimum intensity at the surface normal (scattering angle of 0°), especially for high aspect ratio ridge. Nevertheless, for low aspect ratio (such as profile A) ridge profiles, this argument is not true any more. Our explanation is that a high aspect ratio ridge looks like an antenna. When excited by TM polarization, it sets up dipole oscillation in the ridge, normal to the surface. Therefore, there is a minimum in scattered radiation in the surface normal direction. Low aspect ratio ridges are dominated by in-plane oscillation so they have a maximum radiation in the surface normal direction. [30] indicates a similar disappearance of the dip in P scattering in the surface normal direction for an oblate spheroid with a major-to-minor axis ratio of 1:1.5.

5.6 Application in optical memory system

So far, we have demonstrated the excellent agreement between numerical modeling and experimental measurement of diffraction from subwavelength structure. Furthermore, an aspect ratio extraction and trench/ridge distinguishing technique is proposed and verified with the numerical modeling as the reference. In this section, we will explore the program's application in pit-encoded optical memory system, such as CD-ROM/DVD-ROM system.

Figure 5.22 illustrates some parameters comparison between current CD and DVD format. As we can see, the DVD offers much higher storage density by using shorter wavelength and higher NA to achieve smaller spot size so that each resolvable pit size is decreased, allowing more pits to be squeezed within the same size disk. Here we propose an ultra-high capacity pit-encoded optical memory format that could at least double the storage density of current DVD memory system. This section is organized in the following way. First, we will present the work for a single pit. It is found that there is an interesting difference between TE and TM diffraction, which could be potentially used in high density optical memory. Then a multi-pit encoding method is described to enhance the storage density of optical memory.

	DVD	CD
wavelength	650nm or 635nm	780nm
wavelength in medium	433nm or 423nm	520nm
numerical aperture	0.6	0.45
spot size (λ/NA)	$1.06\mu\text{m}$	$1.73\mu\text{m}$
track pitch	$0.740\mu\text{m}$	$1.6\mu\text{m}$
smallest pit length	$0.400\mu\text{m}$	$0.834\mu\text{m}$
channel bit length	$0.133\mu\text{m}$	$0.278\mu\text{m}$
approximate density	$5.8 \text{ bits}/\mu\text{m}^2$	$1.2 \text{ bits}/\mu\text{m}^2$

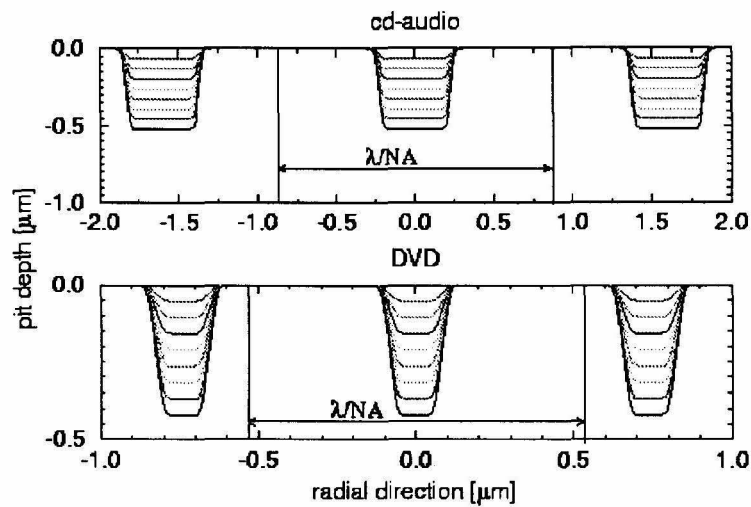


Figure 5.22: Some parameters comparison between current CD and DVD format.

5.6.1 Single pit memory

In order to make our analysis more meaningful, we take the parameter set of the DVD disk for numerical modeling. For comparison purposes, we also calculate the single trench profile with similar parameters for a single bump that corresponds to a DVD single pit. The problems under modeling are listed in Figure 5.23. Figure 5.24 illustrates the surface contours and corresponding far field's scattering intensity of single bump with different heights. The plotted intensity is taken from the 0° scattering location (center reflection point) and normalized to the peak intensity where no pit is presented. From this figure, we can see the interesting diffraction difference between TE and TM mode, which could be used to encode the pits. For example, 00, 01, 10, 11 could be encoded within one wavelength region as marked in Figure 5.24. For trench profiles with different depths, the difference between TE and TM mode is even more obvious. As shown in Figure 5.25, the most dramatic difference happens at a depth of half a wavelength, where the TE mode has a minimum and the TM mode has its maximum. This could be explained, to some degree, by our previously proposed waveguide model, where the waveguide's cut off frequency is around half a wavelength. Furthermore, diffraction of TM mode has more variation than its TE mode counterpart, which could be explained by the fact that TM mode has better penetration than the TE mode. Nevertheless, the encoding mechanism mentioned for a single bump did not work so well as for a single trench. The TE/TM difference at larger depth is pretty small.

5.6.2 Multi-pits memory

So far, we have demonstrated that the spectral intensity difference between TE and TM mode could be used to increase the resolution of DVD disk and a new encoding method to improve the storage density of optical memory. A more straightforward approach to boost the storage density of optical memory is to squeeze in more pits, and/or, with a multilevel depth for each pit, within the same illumination spot size, provided that we can still distinguish those pits.

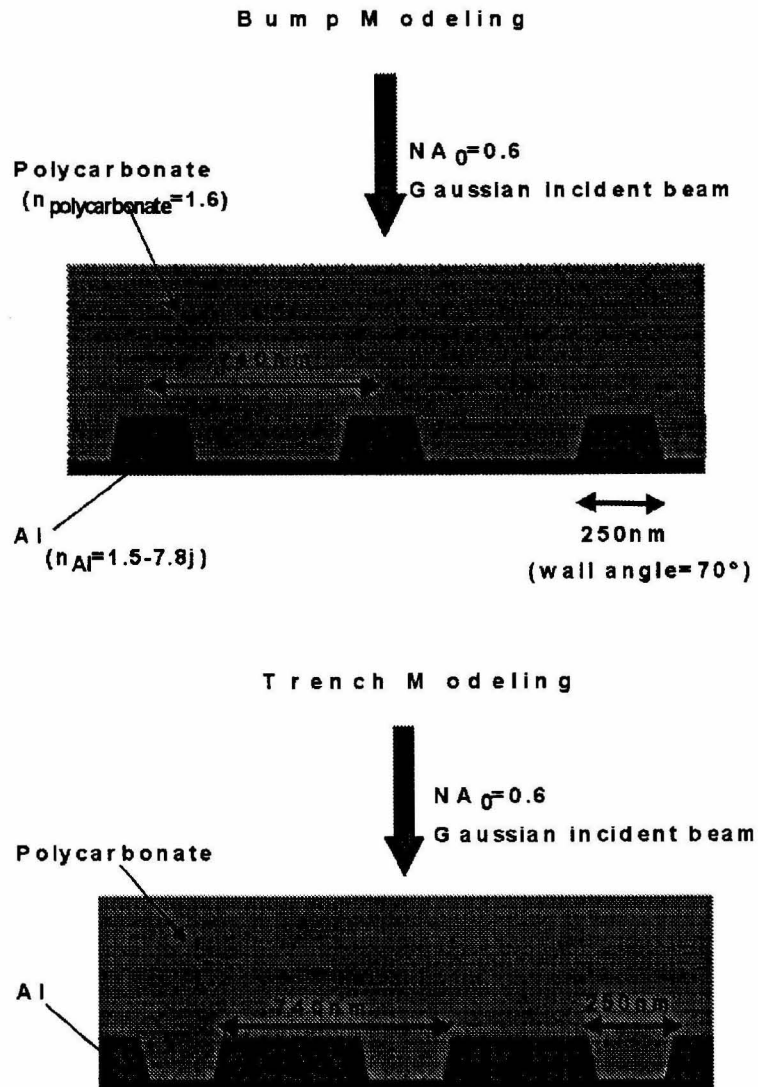


Figure 5.23: Numerical modeling of single pit. (a) single bump. (b) single trench. The parameters are adopted from DVD disc format.

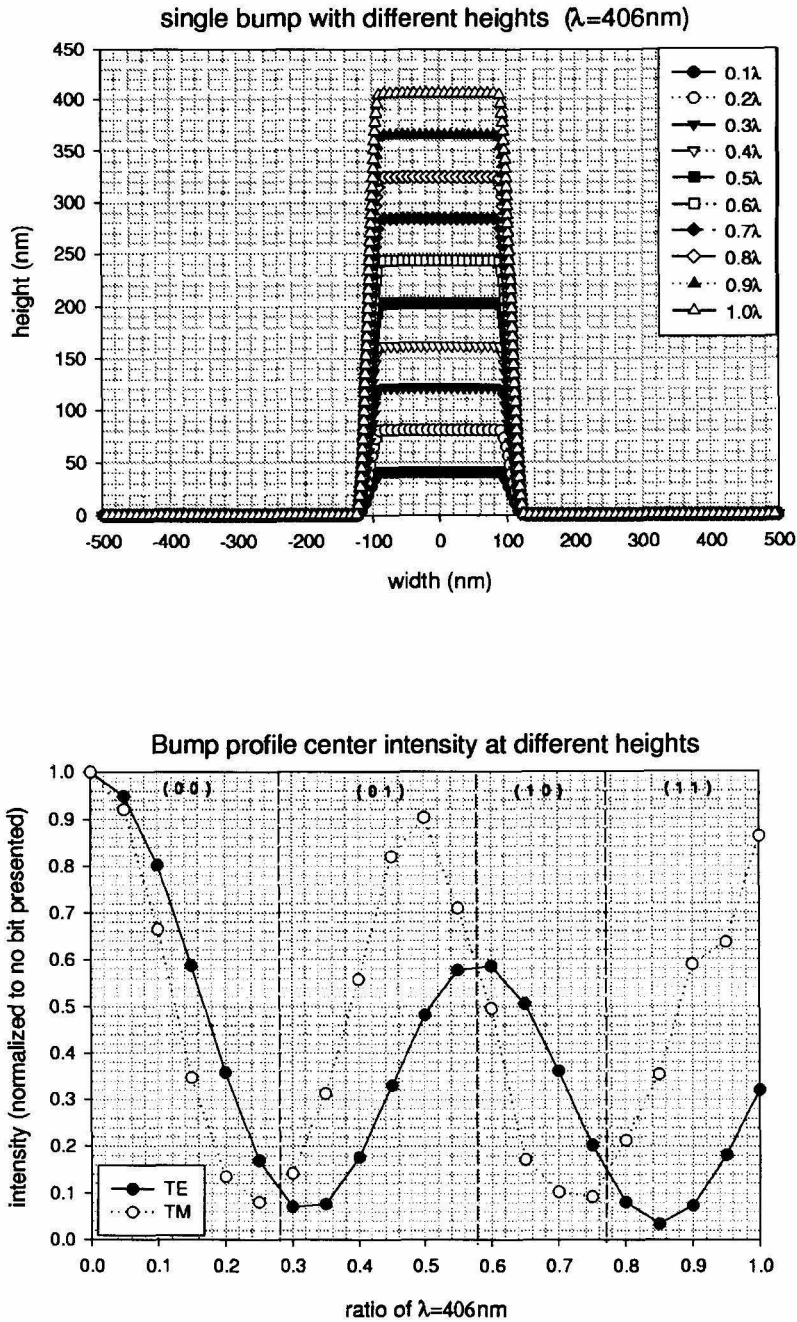


Figure 5.24: Numerical modeling of single pit. (a) contour profiles with different heights. (b) far field intensity at center point corresponding to different heights.

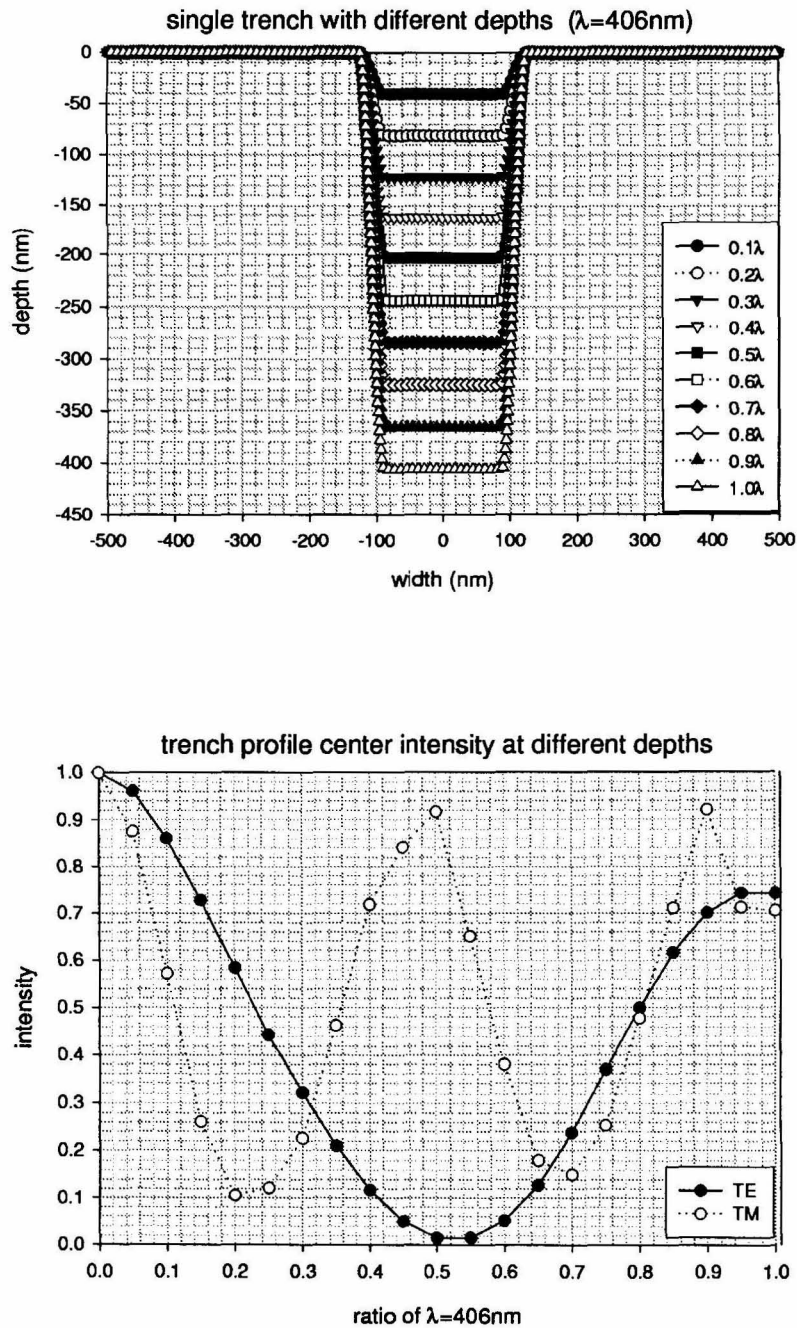


Figure 5.25: Numerical modeling of single trench. (a) contour profiles with different depths. (b) far field intensity at center point corresponding to different depths.

For this multi-pits approach, there are basically two methods to enhance the storage density. One is to keep the distance between each pit fixed and vary the depth of each pit. Another approach is to keep the depth of each pit fixed, say, commonly keep it as quarter wavelength deep, and varying the distance between those pits. Here, only the depth variation approach is explored.

For this depth variation, we keep the distance between pits fixed to be 740nm since it is the distance separation between pits in the current DVD format. The depth variation changes with a step of $\frac{1}{8}$ wavelength from a depth of 0 (mirror surface) to a depth of half a wavelength. Figure 5.26 shows the diffraction intensity of 2 pits (bumps) at central point ($\theta_s = 0$) with different depth combinations. For both TE and TM mode, it shows that, if one pit is presented with a depth of quarter wavelength, the central point's intensity has a local minimum. This means that destructive interference plays a dominant role here. Similarly, if one pit is presented with a depth of half wavelength, the central point's intensity has a local maximum. This means that constructive interference plays a dominant role here. For the case of one pit with quarter wavelength depth and the other pit with half wavelength depth, the overall competition between destructive and constructive interference generates a value between the local minimum and the local maximum. Looking carefully, more information could be extracted from this plot. If we compare the TE and TM intensity, the plot can be roughly divided into 6 regions, those regions' boundaries are located at $(0,0)$, $(0,0.25\lambda)$, $(0, 0.5\lambda)$, $(0.125\lambda,0.25\lambda)$, $(0.125\lambda,0.5\lambda)$, $(0.25\lambda,0.25\lambda)$, $(0.5\lambda,0.5\lambda)$. Furthermore, if we just vary the depth with a step of quarter wavelength, then we just have 4 regions, where the region boundaries are $(0,0)$, $(0, 0.25\lambda)$, $(0, 0.5\lambda)$, $(0.25\lambda, 0.25\lambda)$, $(0.5\lambda, 0.5\lambda)$. From the above discussion, we can encode 2 pits with at least four different codes and decode them by observing the difference between TE and TM mode. With this new coding method, the optical memory's storage density could be improved.

As a final note, although the depth variation method does offer us some way to enhance the storage density, the fabrication/implentation of those proposed pits with different depths turns out to be a very challenging job since accurately controlling the

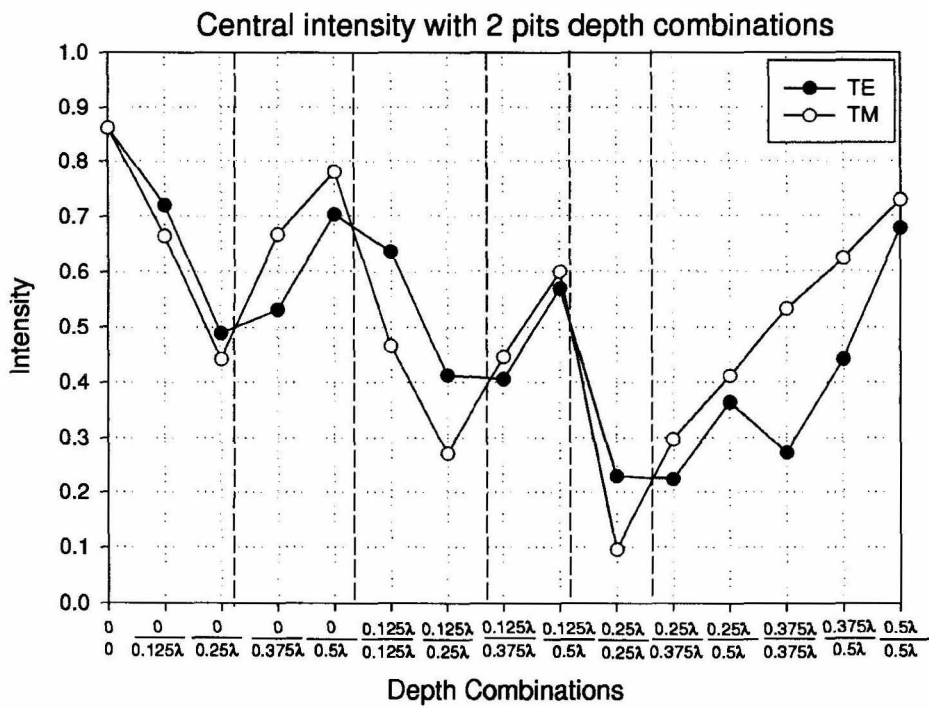


Figure 5.26: Diffraction intensity at center location from 2 pits (bumps) with different depth combinations.

etching depth, especially in a few tens of nano-meters range, is not easy. Furthermore, even if we can somehow control the pit's depths accurately, the mass reproduction of these different depth pits, which is the key factor of success in industry, remains a big question mark. In that aspect, the distance variation method seems to have advantages. The horizontal distance patterning technology is very mature and the mass reproduction of those pits could be easily achieved through a simple mold stamping, just like the current CD-ROM/DVD-ROM disk fabrication. However, this distance variation approach has a big disadvantage. The storage density's improvement is strictly limited by the illumination spot size which is shrinking very fast. This is also the main reason we did not explore this approach for the multi-pits memory system.

Chapter 6 Design of a CMOS detector

This chapter described the design of a CMOS detector as well as the noise analysis which could be used as a guide to improve the CMOS imager's performance.

6.1 Motivation

In Chapter 1, we described a compact memory module where an OEIC chip is used as both the SLM and the detector. It turns out that a system consisting of a separate SLM and detector (see Figure 6.1) could actually offer better performance. In this new system, during the recording, the signal beam is reflected from both beam splitters at the left side and horizontally reaches the crystal. The reference beam is passed through the upper left beam splitter and mirrored down to vertically reach the crystal. The interference between horizontal beam (signal beam) and vertical beam (reference beam) inside the crystal is the hologram pattern that needs to be recorded. This 90° geometry guarantees the largest storage density. Notice that during recording, the phase conjugate mirror located at the bottom of the crystal is turned off. During the readout, however, this phase conjugate mirror is turned on so that the coming reference beam can be reflected back and the resulting readout signal beam is propagating opposite to the original recording direction. This readout signal beam is then passed through the right lower beam splitter and outputs to the detector.

Comparing with the old system (see Figure 1.1 in Chapter 1), the new system has following advantages: First, without the liquid crystal driving/addressing circuit as well as the packaging pad in each pixel, simpler cell structure could result in a smaller pixel size, which is quite beneficial for obtaining higher resolution. Second, a transmission type SLM could offer less power loss and can be totally blocked during the readout so that the readout cross-talk is much less. Higher resolution and smaller cross-talk is quite desirable for increasing the storage capacity of holographic

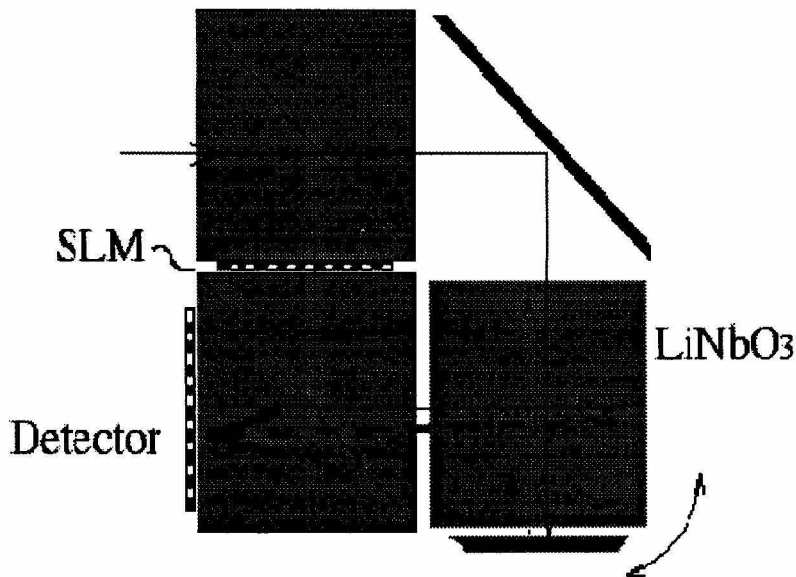


Figure 6.1: Compact system with separate detector and SLM.

memories. Finally, the new system is more practically achievable since we can always build a pixel matching SLM/detector pair. Also with this lens-less configuration, the alignment between SLM and detector can be easily obtained.

In order to demonstrate this new proposed system, a custom designed detector whose pixel size is the same as that of SLM is needed. We have chosen the CMOS imager to be our detector in the system. The reasons are justified as follows: Usually, especially in scientific application where performance is the main concern, CCD cameras are widely used for capturing the image since they have superior characteristics, such as low noise, excellent charge transfer, high quantum efficiency, high fill factor, and small pixel size. However, CCDs need special manufacturing technology where the design methodology is very specialized. On the other hand, solid state imagers, especially the CMOS imager, are getting popular with the fast advancement of CMOS technology. More important, the design methodology is quite universal and the manufacturing facilities, thanks to the tremendous effort from MOSIS, are

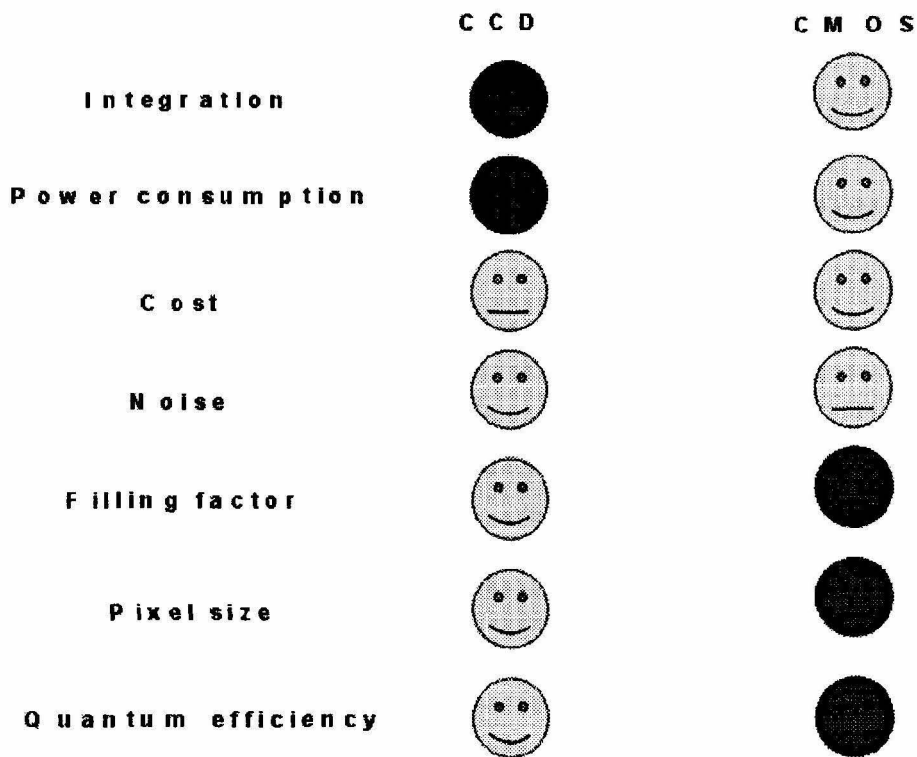


Figure 6.2: Performance comparison between CMOS and CCD detector/imager.

easily accessible. A short comparison between CMOS imagers and CCDs is shown in Figure 6.2. As illustrated in this figure, currently, CCDs still have some advantages in quantum efficiency, pixel size, and filling factor. But with the fast advancement of CMOS technology [44], these advantages are shrinking very quickly. On the other hand, CMOS imager's higher levels of integration ability, lower total system cost, and much lower power requirements far surpass the CCD. Even more, with system requirements such as A/D converters, timing chips and sync signal generators all integrated onto the same device, it will be possible to produce a one-chip camera. This attractive landscape has generated a very hot digital imaging market where the CMOS imager is the key component. Currently, a lot of companies are founded

U S A	Product Specifications
- J P L / P h o t o b i t	PB1024, color, 1024x1024, 10um PD, 8-bit on-chip ADC
- R o c k w e l l / C o n e x a n t	CN1024, color, 1024x768, 6um PD, 10-bit on-chip ADC
- T e x a s I n s t r u m e n t	TC-288, color, 640x480, Analog output
- H P	512x384, 8um PD
- P o l a r o i d / A t m e l	768x512, 15um current-mode APS
- M o t o r o l a / K o d a k	ImageMOS technology
E u r o p e	
- V L S I V i s i o n (V V L)	VV6801, color, 1280x1024, 10.7um x 8.6um, Analog output
- C - C a m / I M E C	2048x2048, 7.5um DR-PD, 8 bit on-chip ADC, 16mm die
J a p a n	
- T o s h i b a	640x480, 5.6um PD
- M i t s u b i s h i	510x493, 7.2um x 5.6um PD
- O l y m p u s	1024x1024, 10um current-mode APS, 12 bit on-chip ADC

Figure 6.3: CMOS imager major developers and their products. PD stands for Photo-Diode, ADC is Analog to Digital Conversion, DR-PD is Direct Readout PhotoDiode, and APS is active pixel sensor.

exclusively working on the commercialization of this CMOS imager to be a one-chip digital camera. Among which, several major players and their products are illustrated in Figure 6.3 [45, 46, 47, 48, 49, 50, 51]. As we can see, current CMOS imager product is reaching SVGA (1024x768) resolution and about 10um pixel size with photodiode (PD) as the standard sensing element. The largest demonstrated imager has 4 million pixel (4Meg pixel resolution) and the smallest pixel size is about $5.6\mu\text{m}$, which is quite comparable with the current status of CCD technology. For the time being, the CMOS imager is coexisting with the CCD where the former is targeted for the low to mid-end imaging market and the latter is targeted for the mid to high-end imaging market. But it is commonly believed that CMOS imager technology will dominate the whole low-to-high end imaging market in the near future, just like the CCD was dominating the whole imaging market during the past 20 years.

6.2 Design details

6.2.1 Basics

Any solid state imaging device pretty much follows the same principle to convert illumination (photons) into free electrons by the photoelectric effect. It is that any photon whose energy higher than the semiconductor material's band gap can always generate a free electron from the valance band into the conduction band. For example, the 1.1ev energy bandgap of silicon makes visible light opaque to silicon since the photo energy of visible light is higher than 1.1ev so that free electrons can be generated. For infrared, however, silicon is transparent and there is no free electron generated since the photon energy is lower than 1.1ev. A well-known formula to calculate the boundary wavelength of transparent and opaque region for a certain material is $\lambda_n = \frac{12400}{E_g} \text{\AA}$, where E_g is the energy bandgap of the material.

For this photoelectric effect, the number of free electrons is decided by the illumination light's energy and the quantum efficiency which is dependent on the material's property. The photon-generated current is represented as

$$I_{photo} = \frac{\eta q P_{in}}{h\nu} \quad (6.1)$$

where η is the quantum efficiency of the photodiode, P_{in} is the incident light power, h is Planck's constant, and ν is the frequency of the illumination light. Quantum efficiency is defined as

$$\eta = \frac{\text{number of collected electron hole pairs}}{\text{number of incident photons at frequency } \nu} \quad (6.2)$$

In order to quickly separate and collect these photon-generated free carriers before recombination happens, we need some kind of well (reservoir) to store those electrons for further processing/conditioning. This could be simply implemented by a reverse biased P-N junction, i.e., a photodiode. As a final note about this photoelectric effect, in addition to those photon-generated free electrons, spontaneously generated thermal

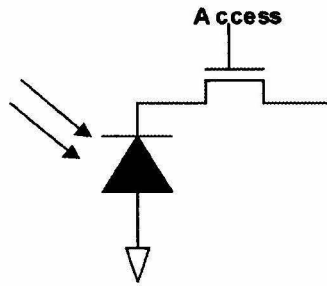


Figure 6.4: Passive photodiode pixel circuits.

electrons also appear in the device and contribute to the noise. (We will discuss the CMOS imager noise issue later in greater detail.)

6.2.2 Sensing elements

Commonly used sensing elements for the solid state imager are photodiodes, photogates, and phototransistors. Although the phototransistor offers large photocurrent gain, the non-uniformity of the gain distribution is a big drawback. Due to this, it has been gradually moved out of the main stream of the CMOS imager industry. Here we will discuss briefly how the photodiode and photogate work.

Passive Photodiode Pixel

Figure 6.4 shows the operation mechanism of passive photodiode pixel [52]. It consists of a photodiode in which the photon energy converts to free electrons and an access transistor to the column bus. After photocharge integration, the array controller turns on the access transistor. The charge transfers to the capacitors of the column bus, where the charge-integrating amplifier at the end of the bus senses the resulting voltage. The column bus voltage reset the photodiode, and the controller then turns off the access transistor. The pixel is then ready for another integration period. The passive photodiode pixel achieves high quantum efficiency due to the large filling factor and absence of an overlying layer of polysilicon such as that found

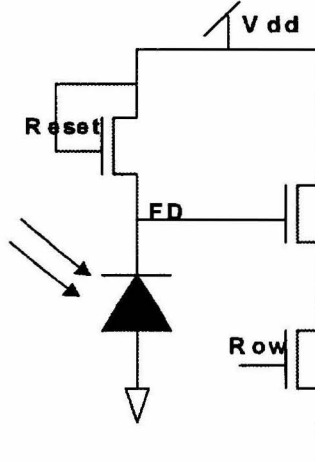


Figure 6.5: Direct readout photodiode pixel circuits.

in many CCDs. However, shortcomings still plague the passive photodiode pixel. The readout noise is high, typical of the order of 250 electrons r.m.s., compared to that of commercial CCDs which is less than 20 electrons r.m.s. of readout noise. Also, it is difficult to increase the array size and readout rate without increasing the noise.

Direct readout photodiode

Direct readout photodiode is ideal for low light application and offers true random access since it does not need integration at all. The signal is continuously read out and is proportional to the incident light intensity. Figure 6.5 shows the operation mechanism of direct readout photodiode [53]. Due to the low photo current, a reset transistor is always operating in the weak inversion (subthreshold) region and the photo current-to-voltage conversion is logarithmic. The relationship between the gate-source voltage V_{gs} and the drain current I_d of the load transistor is given by

$$V_{gs} = \frac{\kappa K T}{q} \ln\left(\frac{I_d}{I_0}\right) + V_T \quad (6.3)$$

where κ is the ideality factor of the MOSFET, I_d is the photocurrent, I_0 is the I_d at onset of weak inversion, and V_T is the threshold voltage. For this design, due to

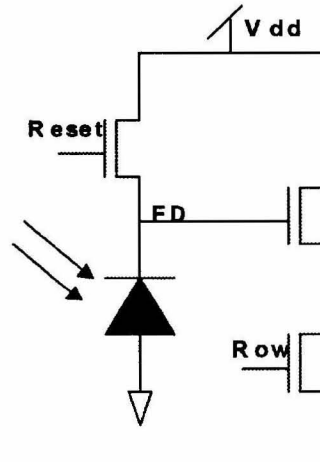


Figure 6.6: Active photodiode pixel circuits.

the lack of integration period, the signal-to-noise ratio is smaller than integration type pixel design. However, this design offers better noise performance than passive photodiode with the same pixel size. This is quite attractive in some applications, such as high speed imaging, low illumination environment detection, etc.

Active Photodiode

It was quickly recognized, almost as soon as the passive pixel was invented, that insertion of a buffer/amplifier into the pixel could potentially improve the performance. A sensor with an active amplifier within each pixel is referred to as an active pixel sensor or APS. Figure 6.6 shows the operation mechanism of active photodiode [54]. The newly added transistors are a source follower, a reset transistor, and a row selection transistor. The source follower buffers the charge onto the bus, which results in faster charging and discharging that allows longer bus lines. This increased bus length, in turn, increases the array size. The reset transistor controls the integration time and, therefore, provides for an electronic shutter. The row select transistor gives half the coordinate-readout capability to the array. This active photodiode pixel also has some drawbacks. More transistors within each pixel limits the pixel size as well

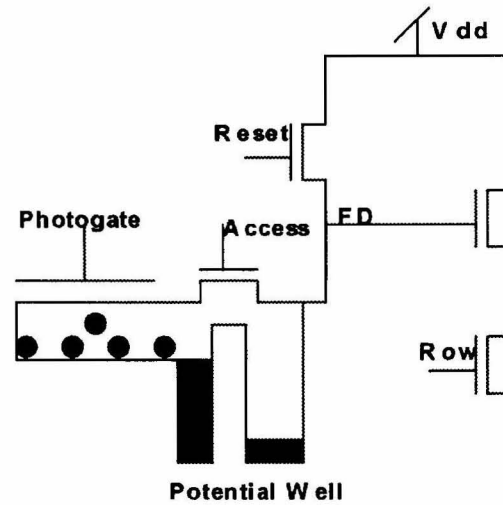


Figure 6.7: Active photogate pixel circuits.

as the filling factor and the typical pixel pitch is around 15x the minimum feature size.

Active photogate pixel

The active photogate pixel borrows the CCD charge-transfer technique to enhance the CMOS imager quality. Figure 6.7 shows the operation mechanism of active photogate [55]. For this pixel, signal charge is integrated under a photogate and performs double sampling readout. First, the array controller resets the output diffusion, and the source follower buffer then reads this reset level charge voltage. Then, after an integration time, a pulse on the photogate and access transistor transfers the charge to the output diffusion. The buffer then senses the new charge voltage. The difference between the reset level and the signal level is the output of the sensor. This correlated double sampling technique suppresses reset noise, $1/f$ noise, and Fixed Pattern Noise (FPN) due to threshold variation. The active photogate pixel offers the lowest readout noise and is optimal for high-performance scientific imaging and low light applications. On the other hand, its 5 transistor-pixel makes its size on the order of 20x the minimum feature size. Furthermore, its quantum efficiency is reduced,

particularly in the blue, due to the overlying polysilicon. Overall, each pixel design has its own advantages as well as disadvantages. A careful design tradeoff is definitely needed.

6.2.3 Readout circuits

The designed CMOS detector's pixel circuit is shown in Figure 6.8. Each pixel consists of three transistors plus a reversed biased photodiode as the sensing element. The operation mechanism is the same as the previously described active photodiode. The pixel size is custom tailored to $17\mu\text{m} \times 17\mu\text{m}$ (that is the pixel size of our SLM in the system shown in Figure 6.1) with 23% filling factor and fabricated with a $1.2\mu\text{m}$ AMI 2-metal 2-poly n-well 5V process through MOSIS. For each column, a correlated double sampling (CDS) circuit is applied to reduce the fixed pattern noise [56]. The whole operation mechanism is as follows: First, the reset transistor is turned on with a short pulse period to reset the Floating Diffusion (FD) to be around 3V. The row select transistor is ON to readout this reset level through a source-follower. The value is stored at capacitor C_R when the sample-and-hold transistor SHR is ON. Then the FD node is discharged by illumination. After a certain integration time, this signal level is read out similarly by source follower and stored at capacitor C_S . In the column level processing, two readouts from reset level and signal level are differentially amplified and the difference is the charge corresponding to the illumination intensity. This is the correlated double sampling (CDS) operation.

The final designed CMOS imager chip layout is shown in Figure 6.9. The whole $2\text{mm} \times 2\text{mm}$ die consists of 64×64 array, where 32×64 are direct readout photodiode pixels and the other 32×64 are active photodiode pixels. The motivation behind this is to compare the performance, especially dynamic range and noise, of those two designs since the ultimate design goal of this CMOS detector is targeting $1\mu\text{m}$ pixel size where the larger dynamic range and lower noise, corresponding to higher sensitivity, are desired. Besides the on-chip CDS conditioning circuits, the chip also features a software controlled window of interest readout implemented by the programmable

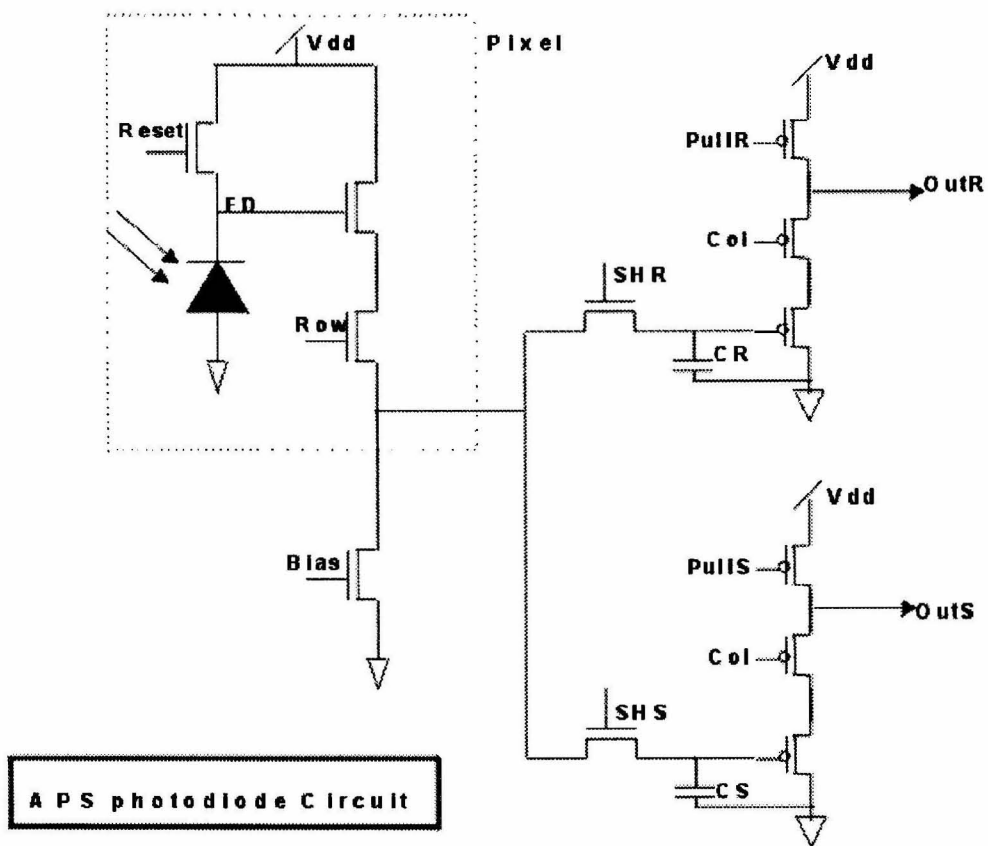


Figure 6.8: Active pixel Sensor (APS) pixel circuits.

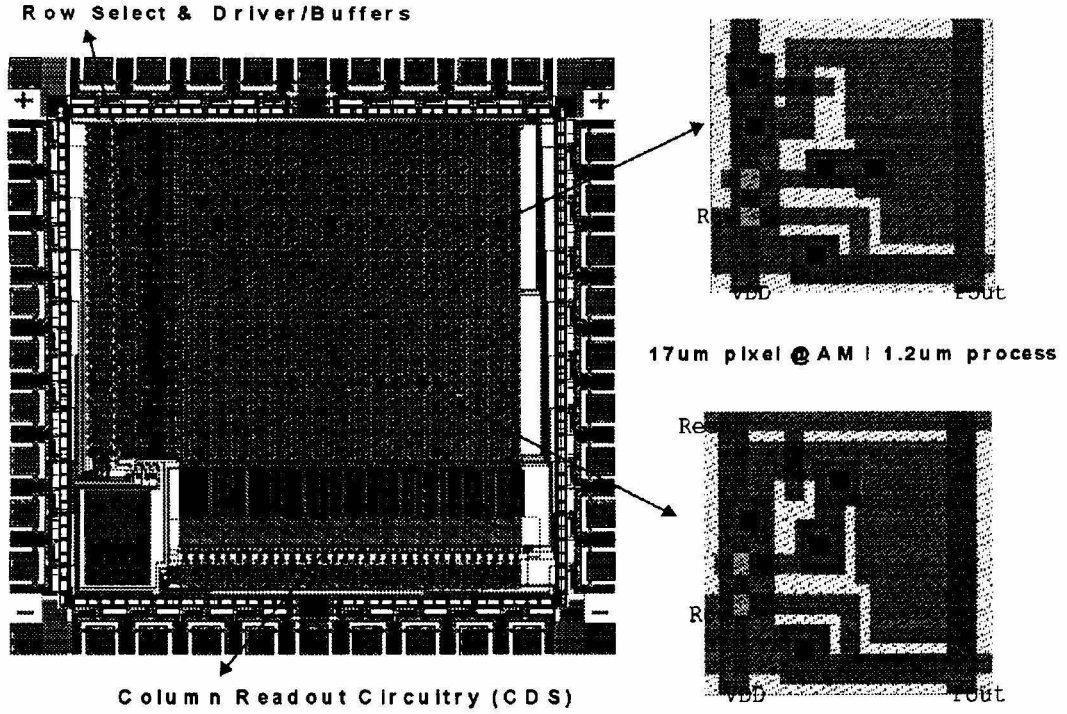


Figure 6.9: CMOS imager chip layout.

row/column decoder. This feature can speed up the image readout rate by scanning out only portions of the whole image.

6.3 Noise analysis

To explore the feasibility of designing an ultra small pixel (targeting 1um pixel size) CMOS imager, a noise/sensitivity is absolutely needed. For any CMOS component, by physics, there are basically three types of noise [57]. The first one is the shot noise which is due to the DC current flow across the P-N junction. Its mean-square noise current power spectral density (PSD) could be represented as

$$\overline{i^2} = qI_{DC} \quad (A^2/Hz) \quad (6.4)$$

where I_{DC} is the average DC current of the P-N junction. This noise is linearly proportional to the DC current. The second type is thermal noise which is due to the random thermal motion of electron and it is independent of the DC current flowing in the component. Its typical mean-square noise current PSD is

$$\overline{i^2} = 4kTg \quad (A^2/Hz) \quad (6.5)$$

where k is the Boltzmann constant, T is the temperature, and $kT=25.9\text{meV}$ at room temperature. g is the conductance in which the thermal noise is occurring. This noise is linearly proportional to conductance and temperature. The third type is Flicker noise ($1/f$ noise) which is due to the carrier trapped in the semiconductor to capture and release carriers in a random manner. The time constants associated with this process give rise to a noise signal with energy concentrated at low frequency. Its mean-square noise current PSD is

$$\overline{i^2} = K_f \frac{I^a}{f^b} \quad (A^2/Hz) \quad (6.6)$$

where K_f is the flicker noise constant, a is a constant (0.5 to 2) and b is also a constant (≈ 1). Obviously, a higher frequency gives smaller noise, which is where the name of $1/f$ noise comes from.

By domain, circuit noise comes from two big categories, spatial noise and temporal noise. In a CMOS imager, the spatial noise is mainly contributed by fixed pattern noise (FPN) which is generated from CMOS field effect transistor (FET)'s threshold variation within the whole CMOS chip. FPN noise is always present since the manufacturing technology is never perfect. But techniques such as correlated double sampling (CDS) can be used to get rid of the FPN noise from the pixel level, and Delta double sampling (DDS) [58] can reduce the FPN noise from the column level. The temporal noise of the CMOS imager is mainly coming from pixel signal conditioning and readout circuits. As its name suggests, if we do not care about the operation speed at all, we can always collect the whole image data several times and

then average to remove the temporal noise. But, in reality, fast operation is definitely needed; nobody wants to wait 10 minutes for just taking one picture. So we must find some other way to reduce the temporal noise. In this analysis, we concentrate on the temporal noise since the FPN noise is well understood and a lot of techniques have been proposed to successfully compress this noise to a very low level already. For our CMOS imager's temporal noise analysis, we discuss each noise generated from Reset, Integration, and Readout operation.

6.3.1 Reset noise

For reset, the dominant noise source is shot noise induced by the reset transistor's drain DC current i_d as shown in Figure 6.10. In steady state, this noise belongs to the well-known KTC noise, i.e., $\overline{Q^2} = KTC_{pd}$, where C_{pd} is the photodiode's capacitance. But, in order to reach steady state, IN voltage must be constant, which means $i_d = i_{ph} + i_{dc}$. This condition usually needs a few ms to settle down, while the reset time is normally a few μs . This means the real steady state is NEVER attained! Actually the reset here belongs to so-called soft-reset since the reset transistor is not turned off completely. During the whole reset period, at the beginning, for a very short amount of time, the reset transistor is in the saturation region. It then goes subthreshold for the rest of reset time.

To find the reset noise under non-steady state condition, we consider the small signal circuit equation with time varying parameters:

$$I_n(t) = C_{pd} \frac{dV_n(t)}{dt} + g_s(t)V_n(t) \quad (6.7)$$

where $I_n(t)$ is the noise source current, $V_n(t)$ is the reset voltage, and $g_s(t)$ is the total transistor transconductance. Solving this equation, we find at the end of reset, i.e., at t_r , the mean square noise charge is

$$\overline{Q_n^2(t_r)} = \int_0^{t_r} W(\alpha) e^{-\frac{\alpha^2}{C_{pd}^2} \int_\beta^{t_r} g_s(\beta) d\beta} d\alpha \quad (6.8)$$

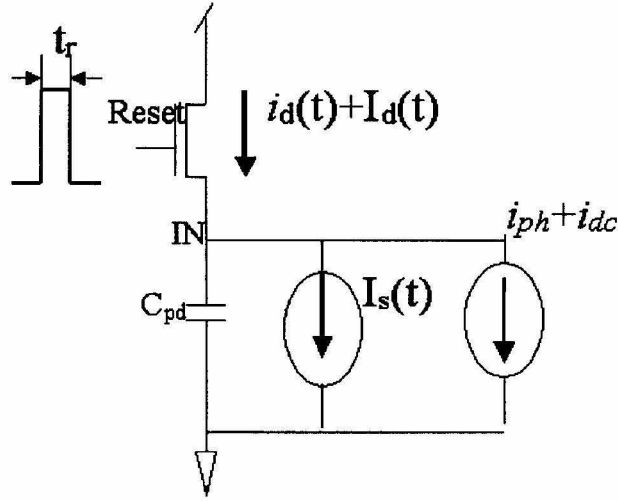


Figure 6.10: Reset circuit small signal model.

where $W(\alpha) = qi_d(\alpha)$ is the PSD of shot noise source. $i_d(\alpha)$ could be solved from the following equation with both above and below threshold operation:

$$\frac{dV_{pd}}{dt} = \frac{i_d(t) - i_{ph} + i_{dc}}{C_{pd}} \quad (6.9)$$

Finally $i_d(\alpha) = \frac{u_T C_{pd}}{\alpha - t_0 + \gamma}$, where t_0 is the transition time from above to below threshold, which is normally less than 1ns. γ is the thermal time which is normally a few ns. Plug the notation of $i_d(\alpha)$ into Equation 6.8, and we have the final formula for noise charge:

$$\overline{Q_n^2(t_r)} = \frac{KTC_{pd}}{2} \left(1 - \frac{\gamma^2}{(t_r - t_0 + \gamma)^2} \right) \quad (6.10)$$

Under normal condition, the second term in the above equation is negligible so that the actual reset noise for our CMOS imager is only half of the commonly quoted KTC. This conclusion explains, to some degree, the common disagreement of the reset noise between experimental measurement and calculation result using KTC formula with the former roughly half of the latter.

6.3.2 Integration noise

The dominant noise source is shot noise $I_s(t)$ due to the dark current i_{dc} and the photocurrent i_{ph} , which is well modeled as white gaussian noise with two sided PSD (as in Equation 6.4). To simplify the notation, we will represent all noises to be charges, i.e., noise electrons. The integration noise is then represented as

$$\overline{Q^2(t_{int})} = q(i_{ph} + i_{dc})t_{int} \quad (6.11)$$

where t_{int} is the integration time.

6.3.3 Readout noise

The readout noise includes thermal noise and flicker noise from the source follower, as well as the thermal noise from the sample and hold circuits. S/H thermal noise is the well-known reset KTC noise at steady state. Notice that now the reset is hard reset since the reset time is normally a few ms which enables the S/H transistor to fully settle down. The notation of noise charge from S/H can be represented as:

$$\overline{Q_{n,S/H}^2} = KTC_{pd}^2\left(\frac{1}{C_S} + \frac{1}{C_R}\right) \quad (6.12)$$

Regarding the noise from source follower, [15] has a detailed discussion. Adopting from it, with 2 assumptions that Q_3 and Q_b have the same physical constants (W, L, B, K') and neglect the body effect ($\eta_3 \ll 1$ and $\eta_b \ll 1$), the derived final formula for noise from the source follower is given by

$$\overline{Q_{n,SF}^2} = \frac{64C_{pd}^2KT}{3t_{int}K'(V_{bias} - V_T)} + \frac{4C_{pd}^2B_3}{W_3L_3} \int_0^{2/t_{int}} \left| \frac{H_{CDS}(j2\pi f)}{f} \right|^2 df \quad (6.13)$$

where V_{bias} and V_T are the bias voltage and threshold voltage. $H_{CDS}(j2\pi f)$ is the transfer function of the CDS operation. W and L are the transistor's width and length. B is the transconductance parameter and K' is the lumped flicker noise constant.

Finally, we combine all previously discussed noise together to get the total tem-

poral noise from CMOS imager with the assumption that the two storage capacitors of S/H circuits are equal. The final result is

$$\begin{aligned}
\overline{Q_{n,total}^2} &= \overline{Q_{n,reset}^2} + \overline{Q_{n,integration}^2} + \overline{Q_{n,readout}^2} \\
&= \frac{KTC_{pd}}{2} + q(i_{ph} + i_{dc})t_{int} + 2KT \frac{C_{pd}^2}{C_S} \\
&\quad + \frac{64C_{pd}^2KT}{3t_{int}K'(V_{bias} - V_T)} + \frac{4C_{pd}^2B_3}{W_3L_3} \int_0^{2/t_{int}} \frac{|H_{CDS}(j2\pi f)|^2}{f} df \quad (6.14)
\end{aligned}$$

To illustrate more clearly how the noises are distributed, we quantitatively calculate the noise using 0.5um AMI 3-metal 2-poly non-silicided n-well process as the target process. The parameters we chose are: $W_3 = L_3 = 1.8\mu m$, $K' = 56\mu V/V^2$, $i_{dc} = 0.25fA$, $B_3 = 10^{-22}m^2V^2$, $V_T = 0.77V$, $V_{bias} = 1.5V$, $C_{pd} = 55fF$, $t_{int} = 1ms$, $\lambda = 0.5\mu m$, quantum efficiency=0.3. The results are listed as below:

- Reset noise: 66.8q
- Dark current shot noise: 1.25q
- Source follower thermal noise: 0.37q
- Source follower flicker noise: 7.3q
- Sample-and-Hold thermal noise: 22.2q($C_s = 1pF$); 12.8q($C_s = 3pF$)

As we can see, the dominant part of the temporal noise is coming from the reset noise. This is why the CDS is commonly used for any CMOS imager design. The second major contributor is the Sample-and-Hold thermal noise from readout operation. This noise could be reduced by using larger S/H capacitor. However, its resulting larger silicon area and slower operation (charging/discharging) speed put some limits there so that a careful design tradeoff is needed. Finally, the source follower flicker noise is surprisingly large. Fortunately, we can reduce it by designing a bigger source follower (enlarge the channel width and length), since this noise is inversely proportional to the follower transistor's channel width and length.

Chapter 7 Conclusion

7.1 Beam deflectors

Two types of liquid crystal beam deflectors have been successfully demonstrated. The essential working idea of those two deflectors is the same, which is utilizing a blazed grating (either permanently fabricated or virtually built up) to deflect the incident beam, where the liquid crystal is used as an electrically controllable birefringent medium. The reflective type deflector exploits the liquid crystal on silicon (LCOS) technology to build up a virtual blazed grating (dynamic grating) and vary this virtual grating's period to achieve multiple steering angles. Seven addressable angles with as high as 93% steering efficiency have been demonstrated. A numerical modeling tool is also developed to analyze the liquid crystal molecule director's distribution under nonuniform electrical field (fringe-field-effect). The transmission type deflector is based on a custom-fabricated PMMA blazed grating (fixed grating) and dynamically addresses multiple angles by stacking several layers of PMMA/LC composite gratings. 16 steering angles are obtained with the contrast ratio of 18. A fabrication-compensation trick is proposed to greatly improve the device's performance.

A couple of suggestions for future developing work: Since our target application for the beam deflector is a holographic memory system, large numbers of addressable angles is definitely the direction to pursue. The proposed programmable LCOS deflector approach should be a good starting point. The other concern is the device's milli-second response time. Some research might be worthwhile for exploring the feasibility of using ferroelectric liquid crystal (FLC) with the device. Finally, the large diffraction efficiency is also needed for device's wider application. Currently, device's energy loss is coming from the silicon substrate's poor reflection and the liquid crystal's scattering/absorption. To reduce these effects, we can first pattern the substrate

with high reflectivity metal, such as aluminum, before other masks involved, and apply the liquid crystal material that has lower scattering/absorption in the operation wavelength.

7.2 Diffraction of subwavelength structure

We have described a simple optical scatterometer for looking at isolated subwavelength features. The features were produced using a focused ion beam process that provided great flexibility in the range of sizes and shapes that could be produced. A numerical modeling program capable of handling arbitrary two-dimensional features in a planar surface was developed. The modeling results were shown to agree very closely with the experimental measurements for scattering from a range of subwavelength features etched into or deposited on a planar metallic surface. The model was then used to investigate what information could be extracted about subwavelength scatterers. We have shown that for two-dimensional features such as scratches, the effective aspect ratio of the feature can be determined by either the ratio of the scattering from s and p polarized illuminating beams, or by monitoring the depth of the dip in scattering at the edge of the specular beam. We have also shown that the s/p scattering ratio can be used to distinguish subwavelength trenches from ridges. Finally, we have shown that a commonly used technique for distinguishing subwavelength particles from pits on a surface can not be extended to features with aspect ratios of 1:4 or smaller. The model developed here can be used to study a wide range of scattering situations for subwavelength features.

However, the developed program package has one disadvantage. It requires that the surface contour must vary smoothly and it should not have sharp corners. This is due to the contour integration singularity issue [59] generated from the integral method. With that concern, finite difference method, either time domain [60] or frequency domain [35], is probably more suitable for future multi-pits optical memory work. It could possibly offer faster computation time and is naturally suitable for pit-encoded optical memory work where the pits usually have large wall angles.

7.3 CMOS detector

We have designed a CMOS detector to be used in a compact memory module. The chip features 64x64 array of $17\mu\text{m} \times 17\mu\text{m}$ pixel with 23% filling factor within a 2mmx2mm die, correlated double sampling (CDS) signal-conditioning circuit in each column, as well as a software-controlled window-of-interest readout. Two pixel designs (active photodiode and direct readout photodiode) are incorporated with the same chip for performance comparison.

It seems that the CMOS imager technology is very hot now and is gradually maturing. However, the most current concern is putting integration on the chip as well as functionality issues. The partial reason is that these two issues are CMOS imager technology's big advantages over CCD technology. But the more profound reason is that almost all the efforts of developing a CMOS imager are coming from industry, where profit is a major driver so that these outperformance of the CMOS imager over CCD are specifically emphasized. From a scientific point of view, it is worthwhile to put some effort into pursuing low noise and high speed operation.

Bibliography

- [1] K. M. Johnson, D. J. Mcknight, and I. Underwood, "Smart SLM using liquid crystals on Silicon," *IEEE Journal of Quantum electronics* **29**, 699–714 (1993).
- [2] S. Chandrasekhar, *Liquid Crystals*. Cambridge University Press, 2nd ed., 1992.
- [3] L. M. Blinov, "Electro-optical effects in Liquid crystals," *Sov. Phys. Usp.* **17**, 658–672 (1975).
- [4] W. Press, B. Flannery, S. Teukolsky, and W. Vetterling, *Numerical Recipes in C*. Cambridge University Press, 2nd ed., 1988.
- [5] "Private communication with Dr. Frank Allan from Merck Inc.," 10 1996.
- [6] Z. Z. Zhong, D. E. Schuele, W. L. Gordon, K. J. Adamic, and R. B. Akins, "Dielectric Properties of a PMMA/E7 Polymer-Dispersed Liquid Crystal," *Journal of polymer science:Part B:Polymer Physics* **30**, 1443–1449 (1992).
- [7] F. J. Kahn, G. N. Taylor, and H. Schonhorn, "Surface produced alignment of liquid crystals," *Proceedings of the IEEE* **61**, 823 (1973).
- [8] B. Bahadur, *Liquid crystals:applications and uses*, **1**. World Scientific, 1990.
- [9] M. Nakamura, "Surface topography and alignment of liquid crystal on rubbed oxide surfaces," *J. Appl. Phys.* **52**, 4561 (1981).
- [10] J.-J. P. Drolet, K. G. Haritos, A. S. Weihua Xu, and D. Psaltis, "Hybrid-aligned nematic liquid-crystal modulators fabricated on VLSI circuits," *OPTICS LETTERS* **20**, 2222–2224 (1995).
- [11] P. Vetter, Y. Ohmura, and T. Uchida, "Study of memory alignment of nematic liquid crystals on Polyvinyl Alcohol coating," *Jpn. Appl. phys.* **32**, **Part 2**, L1239–L1241 (1993).

- [12] K. Hirabayashi, T. Yamamoto, and M. Yamaguchi, "Free-space optical interconnections using liquid crystal micropism arrays," *Inst. Phys. Conf. Ser. No. 139* 195–198 (1994).
- [13] K. Hirabayashi and T. Kurokawa, "Liquid Crystal devices for optical communication and information processing systems," *Liquid Crystal* **14**, 307–317 (1993).
- [14] D. Faklis and G. M. Morris, "Diffractive optics technology for display applications," *SPIE* **2407**, 57–61 (1995).
- [15] J. J. Drolet, E. Chuang, G. Barbastathis, and D. Psaltis, "Compact, integrated dynamic holographic memory with refreshed holograms," *Optics Letters* **22**, 552–554 (1997).
- [16] Q. Chen, Y. Chiu, and D. D. Stancil, "Guide-wave electro-optic beam deflector using domain reversal in LiTaO₃," *IEEE J. Lightwave Technology* **12**, 1401–1404 (1994).
- [17] J. A. Thomas, M. Lasher, Y. Fainman, and P. Soltan, "A PLZT-based dynamic diffractive optical element for high speed, random-access beam steering," *SPIE* **3131**, 124–132 (1997).
- [18] D. P. Resler, D. S. Hobbs, R. C. Sharp, L. J. Friedman, and T. A. Dorschner, "High-efficiency liquid crystal optical phased array beam steering," *Optics Letter* **21**, 689–691 (1996).
- [19] J. Borel, J. C. Deutsch, G. Labrunie, and J. Robert, "Liquid crystal diffraction grating," US patent (10 1974).
- [20] A. F. Fray and D. Jones, "Large-angle beam deflector using liquid crystals," *Electron Letter* **15**, 358–359 (1975).
- [21] T. A. Dorschner and D. P. Resler, "Optical beam steering having subaperture addressing," US patent (3 1992).

- [22] MOSIS, "MOSIS Orbit 2.0 μ m CMOS Process Datasheet," tech. rep., MOSIS, 1995.
- [23] J. W. Goodman, *Introduction of Fourier Optics*. McGraw-Hill, 2nd ed., 1996.
- [24] D. Armitage, "Silicon-chip liquid crystal display," SPIE **2407**, 280–290 (1995).
- [25] T. Uchida, "Present and future trend of liquid crystal devices," SPIE **1815**, 10–17 (1992).
- [26] P. D. Maker, D. W. Wilson, and R. E. Muller, "Fabrication and performance of optical interconnect analog phase holograms made by E-beam lithography," Proceedings of SPIE **CR62**, 415–430 (1996).
- [27] W. Veldkamp, G. Swanson, S. Gaither, C. Chen, and T. Osborne, "Binary Optics: A diffraction analysis," MIT Lincoln Lab Technical Report (1989).
- [28] D. W. Wilson, P. D. Maker, and R. E. Muller, "Binary optics reflection grating for an imaging spectrometer," SPIE **2689**, 255–266 (1996).
- [29] D. Marx and D. Psaltis, "Polarization quadrature measurement of subwavelength diffracting structures," Applied Optics **36**, 6434–6440 (1997).
- [30] Y. A. Eremin, J. C. Stover, and N. V. Orlov, "Modeling scattering from silicon wafer features based on discrete sources method," Optical Engineering **38**, 1296–1304 (1999).
- [31] C. A. Scheer, J. C. Stove, and V. I. Ivahknenko, "COMparison of models and measurements of scatter from surface bound particles," Proceedings of SPIE **3275**, 102–111 (1998).
- [32] H. Haidner, D. Dias, L. L. Wang, and T. Tschudi, "Binary subwavelength structure/resonance gratings as polarization elements," Pure Appl. Opt **7**, 1347–1361 (1998).

- [33] J. J. Greffet and F. R. Ladan, "Comparison between theoretical and experimental scattering of an s-polarized electromagnetic wave by a 2-D obstacle on a surface," *J. Opt. Soc. Am. A* **8**, 1261–1269 (1991).
- [34] D. Marx and D. Psaltis, "Optical diffraction of focused spots and subwavelength structures," *J. Opt. Soc. Am. A* **14**, 1268–1278 (1997).
- [35] W.-C. Liu and M. Kowarz, "Vector diffraction from subwavelength optical disk structures: 2-D near-field profiles," *Optics Express* **2**, 191–197 (1998).
- [36] W.-H. Yeh, L. Li, and M. Mansuripur, "Vector diffraction and polarization effects in an optical disk system," *Applied Optics* **37**, 6983–6988 (1998).
- [37] A. T. D. Hoop, *Modern Topics in Electromagnetics and Antennas*, **13** of *PPL Conference Publication*. Stevenage, England: Peter Peregrinus Ltd, 1977.
- [38] D. Marx, , *Optical diffraction of focused spots and subwavelength structures*. PhD thesis, California Institute of Technology, 1996.
- [39] R. Howland and L. Benatar, *A practical guide to scanning probe microscopy*. Park Scientific Instruments, 1996.
- [40] F. J. Giessibl, "Theory of an electrostatic imaging mechanism allowing atomic resolution of ionic crystals by atomic force microscopy," *Physical Review B* **45**, 13815–13818 (1992).
- [41] J. L. Hutter and J. Bechhoefer, "Calibration of atomic force microscope tips," *Reviews of Scientific Instruments* **64**, 1868–1873 (1993).
- [42] J. C. Stover and M. Bernt, "A multiple particle technique for determination of differential scattering cross-section of very small surface bound particles," *Proceedings of SPIE* **2541**, 108–112 (1995).
- [43] B. M. Nebeker, G. W. Starr, and E. D. Hirleman, "Light Scattering from Patterned Surfaces and Particles on Surfaces," *Proc. SPIE* **2638**, 274–284 **2638**, 274–284 (1995).

- [44] S. I. A. (SIA), "The national Technology Roadmap for Semiconductors," SIA 1994 Report (1994).
- [45] S. K. Mendis, S. E. Kemeny, R. C. Gee, B. Pain, Q. Kim, and E. R. Fossum, "CMOS active pixel image sensor for highly integrated imaging systems," *IEEE J. Solide State Circuits* **32**, 187–197 (1997).
- [46] C. T. Incorporation, "CN1024 datasheet," Website (1999).
- [47] V. V. Incorporation, "VV6801 datasheet," Website (1999).
- [48] D. Scheffer, B. Dierickx, and G. Meynants, "Random addressable 2048x2048 active pixel image sensor," *IEEE Trans. Electron Devices* **44**, 1716–1720 (1997).
- [49] Y. Iida, E. Oba, K. Mabuchi, N. Nakamura, and H. Miura, "A 1/4-inch 330K square pixel progressive scan CMOS active piel image sensor," *IEEE J. Solid State Circuits* **32**, 2042–2047 (1997).
- [50] E.Funatsu, Y.Nitta, Y.Miyake, T.Toyoda, J.Ohta, and K.Kyuma, "An artifical retina chip with current-mode focal plane image processing functions," *IEEE Trans. Electron Devices* **44**, 1777–1782 (1997).
- [51] J.Nakamura, B.Pain, T.Nomoto, T.Nakamura, and E.Fossum, "On-Focal-Plane signal processing for current mode active pixel sensor," *IEEE Trans. Electron Devices* **44**, 1747–1757 (1997).
- [52] G. P. Weckler, "Operation of p-n junction photodetectors in a photon flux integration mode," *IEEE J. of Solid State Circuits* **SC-2**, 65–73 (1967).
- [53] N. Ricquier and B. Dierickx, "Pixel structure with logarithmic response for intelligent and flexible imager architectures," *Microelectron Engineering* **19**, 631–634 (1992).
- [54] P. Noble, "Self-scanned silicon image detector arrays," *IEEE Trans. Electron Devices* **ED-15**, 202–209 (1968).

- [55] S. Mendis, S. Kemeny, and E. R. Fossum, "A 128x128 CMOS active pixel image sensor for highly integrated imaging systems," IEEE IEDM Tech Digest 583–586 (1993).
- [56] R. H. Nixon, S. E. Kemeny, C. O. Staller, and E. R. Fossum, "128x128 CMOS photodiode-type active pixel sensor with on-chip timing, control and signal chain electronics," Proceeding of SPIE **2415**, 117–123 (1995).
- [57] P. E. Allen and D. R. Holberg, *CMOS analog circuit design*. Saunders College Publishing, 1987.
- [58] R. H. Nixon, S. E. Kemeny, B. Pain, C. O. Staller, and E. R. Fossum, "256x256 CMOS active pixel sensor camera-on-a-chip," IEEE J.Solid State Circuits **31**, 2046–2050 (1996).
- [59] M. Abramowitz and I. Stegun, *Handbook of mathematical functions*. New York: Dove Publication Inc., 1965.
- [60] M. S. Mirotznik, J. N. Mait, D. W. Prather, and W. A. Beck, "3-D vector-based analysis of subwavelength diffractive optical elements using the finite-difference-time-domain(FDTD) method," *Diffractive optics and micro-optics* **10**, 91–93 (1998).